COHERENT NONLINEAR OPTICAL SPECTROSCOPY OF InGaN DISKS IN GaN NANOWIRES

by

Cameron R. Nelson

A dissertation submitted in partial fulfillment
of the requirements for the degree of
Doctor of Philosophy
(Electrical Engineering)
in the University of Michigan
2017

Doctoral Committee:

Professor Duncan G. Steel, Chair
Professor Hui Deng
Professor Pei-Cheng Ku
Professor Theodore B. Norris

ACKNOWLEDGEMENTS

First and foremost I would like to acknowledge my family: my wife Shirley and my parents for giving me the love and support needed to complete this dissertation. The thesis presented here is dedicated to them.

Next I would like to thank my adviser Duncan for giving me the opportunity to complete this work. I continue to be amazed and impressed at Duncan's rigorous approach to science and training students that transforms first year graduate students into competent, independent and confident scientists. Duncan has shown a nearly infinite amount of patience with me as I learned the ropes of the lab and about communicating my work. I can't overemphasize how much his training has developed me positively as a person.

I also give thanks to my thesis committee: Professor Ted Norris, Professor Hui Deng and Professor P.-C. Ku for taking the time to read my thesis and attend my defense.

Many thanks to the collaborators who grew the samples featured in this work: Saniya Deshpande and Shafat Jahangir, who worked in Professor Pallab Bhattacharya's group and Yong-Ho Ra in Professor Zetian Mi's group for their incredible patience and skill. This work would not be possible without their efforts and constant feedback.

Finishing a Ph.D requires a lot of support from your colleagues. I am truly lucky to have had the opportunity to work with people I now consider my great friends: Uttam (the Pal), Aaron, Midhat, Alex, Palbert, Colin, Bo, Greg, John, Adam, Christine, Madelyn and Victoria. Special thanks to Aaron for helping me to proofread this work. Their support and friendship allowed me to persevere even through the most

difficult times.

Uttam and I worked in the same side of the lab, and you learn more about a person this way than I can describe in this paragraph. Buddy, I want to thank you and Marta for the countless lunches and enduring my complaints about my experiment. After all these years, Uttam is like a brother to me.

Thanks to the north campus crew: Heather, Brandon and Kyu-Tae (even though central campus is more cool). Also thanks to all of my friends in Ann Arbor. Finally I would like to thank Chrissy, Paul and Joe.

TABLE OF CONTENTS

LIST OF TABLES

Table

LIST OF FIGURES

Figure

LIST OF APPENDICES

Appendix

CHAPTER 1

Optical applications using III-nitride quantum confined structures

InGaN and the associated III-nitrides such as GaN and AlGaN have emerged as some of the most important solid state materials in the world for optical applications. Much of this has to do with the fact that III-nitrides are direct band gap materials that emit in the full visible spectrum and the deep UV, thus providing a useful source of light for the human eye. Another significant aspect of III-nitrides is the fact that the exciton (Coulomb bound electron-hole pair) binding energy is typically almost an order of magnitude larger than other more conventional semiconductor light emitters [11], therefore the possibility of relatively high temperature quantum optical applications is open. The work in this thesis is focused specifically on InGaN disks grown inside GaN nanowires that have been shown to have similar properties to quantum dots [12]. The experimental goal in this work to measure the third order coherent nonlinear optical spectrum ($\chi^{(3)}$) to lay the groundwork for more sophisticated experiments, possibly involving coherent control of the disk-in-nanowire exciton.

This chapter will first serve as a review for the existing optical applications using III-nitride nanostructures and heterostructures. This includes some historical overview of the development of applications in solid state lighting and laser technology. Within this discussion, some recent developments related to InGaN single photon emitters is included. A discussion of the future potential uses of InGaN in coherent control applications follows, using existing results from III-As systems as a model.

1.1 III-nitride light emission technology

It is worthwhile to mention the impact that III-nitride materials have had on the development of semiconductor technology, specifically in light emission applications. The development of III-nitride light emitters began with quantum well technologies in the 1990s. III-nitride quantum wells are inherently limited in spectral range for light emission applications due to strain related effects, however recent developments have shown that quantum dots can overcome some of these deficiencies. In this section some of the important results in III-nitride light emission applications will be highlighted. I will first discuss the use of III-nitride structures in solid state lighting and laser technology. Later on, the use of III-nitride quantum dots as single photon emitters for room temperature quantum information applications such as quantum cryptography will be mentioned.

Much of the development of III-nitrides as light emitters stemmed from the controlled creation of InGaN light-emitting diodes (LEDs). The historical development of the InGaN LED will be discussed shortly. An LED is created when an active semiconductor layer that provides light emission is sandwiched between two semiconductor layers where one layer is n-doped and one is p-doped. The p-n junction creates a depletion region that is centered in the active region. Applying a positive bias to the system results in the injection of charges into the depletion region that results in radiative recombination for direct bandgap materials. To make a laser, partially reflecting facets can be added to the perpendicular ends of the semiconductor sandwich to create a laser cavity, where the active region provides the gain medium. In some structures, a single semiconductor quantum dot is used as the active region. If a sufficiently small current pulse can be applied to the single quantum dot structure, the active region can emit single photons on demand for applications such as quantum cryptography. The basic structure of the LED is shown in Fig. 1.1 from Ref. [1].

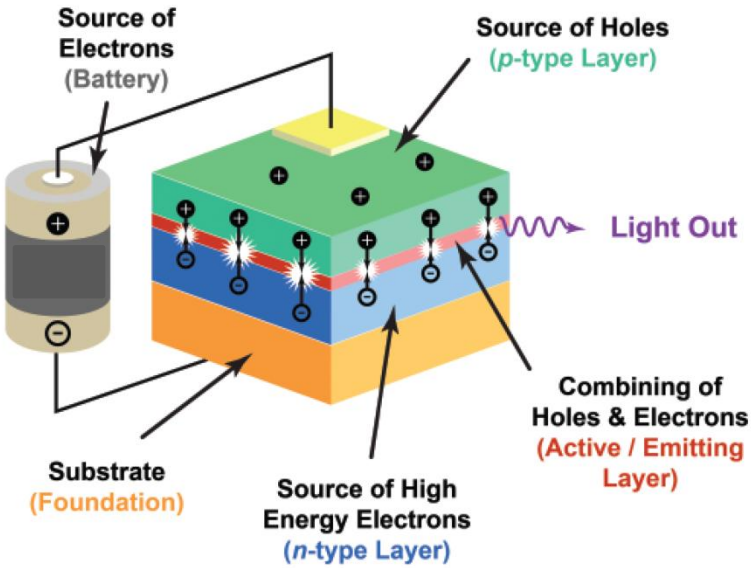

Figure 1.1: Schematic of an LED from [1]

1.1.1 Solid state lighting using InGaN

Fluorescent bulbs are commonly used in business and industrial settings because they are typically much more economical and energy efficient compared to incandescent bulbs. That being said, a major issue with fluorescent bulbs is the use of mercury in their construction and the associated costs with proper disposal. One alternative to fluorescent lights uses blue-violet emitting semiconductor LEDs and phosphor screens. The blue-violet light is absorbed in the phosphor and is re-emitting at a higher wavelength, thus the combination of the unabsorbed blue-violet and phosphor emission can span the full visible spectrum. Due to their enviornmental advantages, developments in the fabrication of white light emitting LEDs based on InGaN light emission technology has made LED-based lights the highest efficiency source of lighting in the world, even surpassing compact fluorescents [13]. If trends continue, it is estimated that by 2030 the total savings in input energy by using LEDs compared to other light sources will avoid generating 185 million tons of CO_2 [1, 13].

Prior to the mid-1990s, there were no semiconductor materials available that could be made into LEDs that emit in the blue-violet part of the visible spectrum, although several candidate materials including InGaN/GaN and ZnSe were theoretically available. One of the largest issues with using InGaN/GaN materials prior to the mid-1990s was that the controlled p-doping of GaN had not been successful. A determined engineering effort by Shuji Nakamura using a home-built set-up in the late 1980s-early 1990s eventually led to the first reliable growth of p-doped GaN using Mg as an acceptor. Using InGaN quantum wells as an active layer between layers of doped GaN, Nakamura and colleagues reported the first fabrication of an InGaN LED emitting in the blue spectral region [14]. The development of the first InGaN-based light sources by Shuji Nakamura, Hiroshi Amano and Isamu Akasaki resulted in their award of the Nobel Prize in physics in 2014.

The success of InGaN-based LEDs is largely based on material disorder. Compared to other light emitting materials such as GaAs, ZnSe or GaAsP, InGaN planar quantum well light emitters are very insensitive to structural defects that are associated with nonradiative recombination. The material disorder creates localized regions in the material where a large density of electron-hole pairs can recombine and emit light. Thus, even though the density of defects in InGaN layers can exceed other materials with no disorder effects such as ZnSe, the output efficiency of InGaN layers can be larger due to a larger density of disorder states. This is an extremely important feature of InGaN that allows for the construction of efficient InGaN LEDs on cost effective substrates such as silicon.

Although the commercial fabrication of blue emitting InGaN LEDs has become fairly well-developed at this point, InGaN technology has yet to achieve its full potential since the green-red region of the visible spectrum has not been available. Typically InGaN/GaN quantum wells are grown using polar wurtzite material, a crystal configuration that leads to large, strain-induced electric fields in the material active region due to the lattice mismatch between the InGaN and GaN layers [11]. The internal electric field strength in the $In_xGa_{1-x}N$ layer increases with InN mole fraction x, therefore red emitting structures have a higher internal electric field compared

to blue emitting structures. Due to the higher lattice mismatch, green-red emitting InGaN/GaN planar quantum wells also have a much larger density of growth defects compared to blue emitting structures. As a result of these two effects, red-green emitting planar InGaN quantum wells have a much lower emission efficiency compared to blue-emitting InGaN planar quantum wells. Prior to recent work with InGaN quantum dot materials that will be mentioned shortly, there was in fact a lack of any reasonably efficient light-emitting semiconductor material in the green spectral region, an aspect known as the green gap [15,16]. Full color tunability in InGaN light emitters could have a large impact on the emission efficiency of the LEDs since the conversion process from blue light to white light using a phosphor, a process that has inherent energy loss, would not be required.

In solid state lighting applications, initial results with InGaN quantum dots have shown that they can be used to bridge the green gap. InGaN quantum dots are usually formed as a result of a strain relief mechanism, therefore effects related to the strain-induced internal electric fields are largely alleviated [17]. Furthermore, certain designs of InGaN quantum dots such as InGaN-disks-in-GaN nanowires can be grown with virtually defect-free active regions. As a result, the emission efficiency of InGaN quantum dots is significantly higher than in quantum wells and the fabrication of full visible spectrum solid state lighting has become much closer to a reality [18]. Aside from the possibility of more economic solid state lighting, the invention of LEDs that emit in the full visible spectrum creates opportunities in other applications using incoherent light such as water-splitting [19] or phototherapy [20].

1.1.2 Lasers

The advent of LEDs constructed from blue-emitting planar InGaN layers in the mid-1990s naturally led to the use of blue emitting planar InGaN layers in solid-state laser devices [21]. One of the most well-known applications for blue emitting lasers is in data storage applications. The invention of InGaN blue emitting lasers spurred on the invention of higher storage ROM disks, eventually resulting in new widely used

technology such as DVD-ROM [22].

The large internal electric fields and defect densities in planar InGaN quantum well layers haved created issues in laser technology as well as in solid state lighting. The large electron-hole separation leads to extremely large threshold current densities for green-red emitting planar quantum well InGaN laser structures compared to other red emitting materials [21, 23]. Furthermore, screening of the internal electric fields leads to a blue shift in the output wavelength of the lasers as a function of carrier injection [24]. The use of strain-relieved quantum dots as the laser active region in InGaN structures has led to the construction of solid state lasers throughout the visible spectrum with low current threshold densities and small wavelength shift due to the significantly lower internal electric fields [25, 26]. Low threshold current lasers that use InGaN disks-in-nanowires as the active region have also been successfully fabricated on Si substrates, an important innovation for Si photonics applications [27].

1.1.3 InGaN quantum dot light emission technology with single photons

Although III-nitrides are primarily known for solid state lighting and laser applications that utilize many photons at a time, quantum confined III-nitride nanostructures are also being used to generate on-demand single photons for applications in quantum information science.

Due to Coulomb effects, quantum dot systems admit the occupation of only a single electron-hole pair at a given energy level [28]. This means that only one photon can be emitted at a given energy from the quantum dot at a given time. A set-up shown below, known as a Hanbury-Brown and Twiss (HBT) interferometer [29], can be used to confirm this behavior.

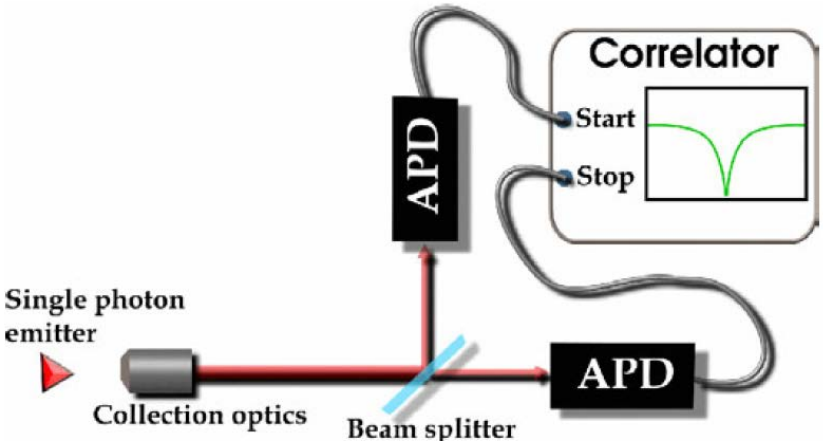

Figure 1.2: Schematic of Hanbury-Brown and Twiss interferometer from [2]

In an HBT interferometer, emission from the quantum dot is first sent to a 50/50 beam splitter and coincidence counts are measured between two detectors placed at the ports of the beam splitter to give the second-order correlation function $g^{(2)}(\tau)$, where τ is the time delay between the two arms. Ideally, the second-order correlation function at zero relative time delay between the two arms indicates that the system can only emit a single photon at a given time [30, 31], hence an ideal quantum dot system shows zero coincidence counts at zero time delay for a given emission energy.

Nanostructures made from III-nitride materials have emerged as a candidate material for room temperature quantum applications. This stems from the relatively large exciton binding energy in III-nitrides compared to more conventional semiconductor materials such as III-As [32] that has led to demonstrations such as single photon emission in single III-nitride quantum dots up to room temperature [10, 33]. This result is generally not observed in more conventional III-As quantum dot systems due to exciton dissociation at room temperature [34, 35].

One application that utilizes engineered single photon emitters is quantum key distribution, a topic that falls under the umbrella of a larger research area known as quantum cryptography [36]. The polarization state of single photons can be used to generate a secure key that allows two users to communicate securely without the

threat of eavesdropping [37]. It has been recently shown that InGaN single photon emitters with well-defined polarization states can be fabricated by etching planar InGaN quantum wells into elliptical nanostructures, where the direction of photon polarization is along the long axis of the ellipse [38,39]. The degree of linear polarization in the etched InGaN nanoellipses is typically much higher than other direct-gap materials due to strong valence-band mixing effects in III-nitrides. Strain-induced valence band mixing effects will be discussed further in future chapters. These demonstrations along with the demonstration of room temperature single photon emission make InGaN quantum dot systems strong potential candidates for room temperature quantum cryptography using photons.

1.2 Coherent optical control of solid state qubits

Although semiconductor quantum dots are typically composed of $\sim 10^5$ atoms, the interaction between a single quantum dot and a light field can mimic the properties of the interaction between a light field and single atom. This has thrust semiconductor quantum dots into research towards applications in quantum information technology where the quantum state of a single atom-like structure is carefully controlled using an optical field and subsequently the quantum state of the system can be entangled together with other quantum states using emitted photons. In an energy picture, the time-dependent state of the quantum dot exciton can be mapped to a two-level energy system, or qubit, where the excited state represents the creation of an exciton (or biexciton, trion) and the ground state is the crystal ground state. Interactions with resonant laser fields drive the population of the qubit from the ground state to excited state and back to the ground state, a process known as Rabi rotation or oscillation [30]. In principle, a pulsed laser field can be used to reliably coherently control the state of the two-level system so that an arbitrary superposition state with a well-defined phase can be achieved. In coherent optical control applications, quantum dots have several advantages over real atoms or ions such as the ability to precisely control the quantum dot position [40] and an enhanced dipole moment

compared to atoms [41].

The primary application of interest for coherent control of qubits is quantum information processing or quantum computation. Quantum information processing utilizes the quantum entanglement of many optically prepared qubits to perform computations [42,43]. For some calculations, such as prime factorization of large numbers, quantum computers can largely outperform classical computers [44]. Expedited prime factorization calculations can have serious impact in the area of internet security, for example. Typically internet messages are encrypted using RSA protocols [45] that utilizes the fact that prime factorization is inefficient using classical computers. Quantum computation also allows us to simulate the behavior of quantum systems. This was in fact one of the key drivers for implementing quantum computing when the field began in the 1980s [46]. If a functional quantum computer were to be realized, it would likely revolutionize the way in which scientific modeling is performed.

1.2.1 Developments in quantum information processing using coherent control in III-As quantum dots

In this section I will digress a bit from the main topic of this chapter and discuss some of the experimental progress in coherent control of III-As systems and the associated applications. A more extensive review of the topic is provided in ref. [47]. In terms of coherent control applications, III-As quantum dots have shown the most progress of any other semiconductor material. The experimental progress in III-As can essentially serve as a model for future studies in III-nitrides.

A necessary prerequisite to coherent control demonstrations in III-As quantum dots was an understanding of the coherent nonlinear optical spectrum of a single quantum dot using resonant laser fields. It has been shown experimentally that the coherent nonlinear optical response of the exciton state in single III-As quantum dots is atom-like, and that the coherent nonlinear response can be modeled using the density matrix equations of motion. Furthermore, the dipole dephasing rates in III-As quantum dots were shown to be much less than the spontaneous emission rate.

A low dipole dephasing rate is an important requirement for a qubit in a functional quantum computer [42, 43]. Shortly after the coherent nonlinear optical spectrum of single GaAs interface fluctuations quantum dots was mapped out, coherent control experiments were performed [48, 49] that showed that the internal state of a single quantum dot could be reliably manipulated using laser fields.

Experiments that have demonstrated coherent control in III-As quantum dots have led to significant progress toward the creation of the basic elements solid state quantum information processing. Due to the relatively fast radiative decay of the exciton state, typically the ground state spin of a single quantum dot is used as the system qubit. Experiments have demonstrated coherent control and read out of the ground state spin [50, 51]. In addition, our group has demonstrated the entanglement between the spin state of the electron in a charged quantum dot and the polarization state of a photon, an important stepping stone toward connecting together two functional spin qubits [52].

1.2.2 Towards coherent optical control in InGaN quantum dots

In general, the solid state environment quantum dots causes unwanted interactions, especially at room temperature where strong phonon interactions are typical for many materials including III-As systems. As a result, III-As quantum dots require cryogenic cooling in carefully controlled environments in order to maintain functionality for quantum information applications. Research continues to try to find a quantum dot material that can be coherently controlled at room temperature and also to show that the nanostructure can be used in real quantum information applications. As stated, the goal of this work is to measure the coherent nonlinear optical spectrum of InGaN nanostructures for future coherent control applications due to the potentially high temperature stability of the exciton in the system.

Compared to III-As quantum dots, progress towards coherent optical control applications such as quantum information processing using InGaN or other III-nitride quantum dots has not yet had time to develop. At the same time there has been some

progress: evidence of of Rabi oscillations in a single small GaN quantum dots [53] and a non-polar InGaN quantum dot system [54] has recently been observed at low temperature. One major roadblock for the implementation of III-nitride materials in future applications using coherent control is the presence of relatively large optical linewidths in the system that indicates the presence of dipole dephasing, even at low temperature. In single III-nitride quantum dots, the linewidth measured in frequency-resolved linear optical measurements such as photoluminescence can up to $\sim$1000 times greater than the lifetime limited value [55]. It is likely that the linewidth is III-nitride quantum dots is broadened by effects that cause dipole decoherence such as transient interactions of quantum dot excitons with nearby charges. The presence of a large dephasing rate severely limits the possibility of implementing coherent control applications in InGaN quantum dots at present. Optically controlled quantum information processing using coherent control of InGaN quantum dots is still far away into the future.

The work in this thesis is centered on measuring the coherent nonlinear optical spectrum in ensembles of red-emitting InGaN disks-in-nanowires in order to understand the intrinsic interactions and decay mechanisms in the material to pave the way for more sophisticated coherent control measurements. We find that the nonlinear optical dynamics of excitons in our InGaN DINW samples is dominated by effects related to a large density of background disorder states and/or metastable trap states. At the same time, the nonlinear optical response of the system is largely unaffected by temperature and a strong nonlinear signal is measured up to room temperature, which is a promising result for future coherent control demonstrations. Future coherent control applications will require a high degree of increased control over the growth properties of future samples to eliminate the negative effects of disorder. The specific aspects of each chapter in this work is given in the next section.

1.2.3 Summary of the work in this thesis

In ***Chapter* 2** an overview of the optoelectronic properties of semiconductor

nanostructures with a focus on wurzite materials is given. Methods for calculating the bandstructure in quantum confined heterostructures such as the $\boldsymbol{k} \cdot \boldsymbol{p}$ method are mentioned and results from the literature for III-Nitride materials are featured. The effects of internal electric fields in InGaN/GaN heterostructures are considered, such as the quantum confined Stark effect. The basic Hamiltonian for optical interactions in semiconductor nanostructures is also discussed. Finally, some specific optoelectronic aspects of the DINW samples in this thesis are presented including a calculation of the internal electric fields and the electron and hole wave functions using a $\boldsymbol{k} \cdot \boldsymbol{p}$ solver.

In ***Chapter* 3** an overview of the line shapes in the frequency domain of the third order ($\chi^{(3)}$) coherent nonlinear optical response of two-level systems such as quantum dot excitons and the methods for theoretical calculation of the line shapes using the density matrix is presented. The Maxwell-Bloch equations are introduced in order to relate the quantum mechanical polarization of the two-level systems to classical nonlinear fields emitted by the sample. A variety of different line broadening mechanisms are included in the calculations such as inhomogeneous broadening, pure dephasing and slow spectral diffusion.

In ***Chapter*4** phase-sensitive detection methods of nonlinear signals are described. This chapter is also meant to highlight some of the modifications to the standard nonlinear detection techniques have been used for measuring the coherent nonlinear optical spectrum of III-As materials in our group.

In ***Chapter* 5** the linear and nonlinear optical data of InGaN disks-in-nanowires that are self-assembled on a silicon substrate are presented. Due to substrate roughness, many of the nanowires grow at different angles and coalesce together during growth. The coalescence leads to the formation of defects that trap charges at the boundaries between the coalesced nanowires. We find that the nonlinear dynamics is mainly driven by interactions between metastable traps, likely formed due to coalescence, excitons and background disorder states. Despite complicated optical physics in the system, we observe that resonances that are assigned to excitons persist up to room temperature, validating the fact that the system shows strong excitonic absorp-

tion at room temperature.

In ***Chapter* 6** a study of selective area InGaN disk-in-nanowires is presented. The selective area nanowires can be grown without significant nanowire coalescence, therefore effects related to metastable charge traps are not observed in this system. This chapter focuses on effects related to background disorder states and their effects on excitons in the system. In particular, it is found using intensity-dependent photoluminescence and nonlinear spectroscopy that electron-hole pairs excited into the background disorder states transfer energy into lower energy exciton states. The focus of this chapter is on the dynamics of emission in selective area DINWs.

In ***Chapter* 7** the third order ($\chi^{(3)}$) coherent nonlinear optical spectrum of selective area InGaN disks-in-nanowires is presented. Although an analysis of the spectrum is complicated by the presence of background disorder states in the system, some aspects can be understood in terms of a quasi-two-level system model. We find evidence of a hole burning response that shows dipole dephasing rates $\sim$ 30-40 meV. This observation is confirmed by observing population pulsation resonances in the system that show decoherence-induced extra resonances due to the large decoherence rate in the system. This is the first observation of decoherence-induced extra resonances in a solid state system.

Finally, in ***Chapter* 8** the work in this thesis is summarized and future research directions are suggested.

CHAPTER 2

A review of the optoelectronic properties of wurtzite InGaN/GaN heterostructures and InGaN disks in GaN nanowires

For optical applications, III-Nitride material, most commonly found in the wurtzite crystal configuration, is relatively unexplored compared to more mature III-As materials such as GaAs and InAs, which are most often found in the zinc blende crystal configuration. In previous Ph.D theses in our group, the optoelectronic properties of zinc blende materials has been extensively reviewed (see for example refs. [56, 57]). A discussion of the optoelectronic properties of the material system is an important foundation toward the main focus of this thesis that is nonlinear optical interactions between solid state quantum confined systems and light fields. The main goals in this discussion are to understand the nature of the electronic eigenstates (and their corresponding energy separations) that appear in important physical quantities such as optical transition matrix elements. The nature of the eigenstates can be used to understand the optical polarization selection rules and to justify the use of 2-level system models that will be described in future chapters.

This chapter will review results in the literature describing the basic electronic band structure near the k = 0 point for bulk wurtzite materials including the effects of strain. The effective mass approximation will be introduced and methods of calculating quantum confined wave functions, such as the envelope function approximation, will be discussed. In addition, the internal electric fields generated due to the polar growth configuration in InGaN/GaN heterostructures and their effects on the electron and hole envelope functions will be presented. A review of the effects

of material disorder on the emission and absorption properties of InGaN/GaN heterostructures will be included. In the final two sections of this chapter, the specific optoelectronic properties of the samples under study in this work will be introduced.

2.1 Electronic bandstructure in bulk wurtzite materials

We first begin by outlining the nature of electronic states in wurtzite materials and reviewing results in the literature that describe the wurtzite bandstructure, neglecting strain and spin-orbit coupling. Schrödinger's equation in a wurtzite material is given by

$$[\frac{p^2}{2m_e} + V(\boldsymbol{r})]\psi(\boldsymbol{r}) = E\psi(\boldsymbol{r}), \tag{2.1}$$

where V($\boldsymbol{r}$) is the background potential experienced by the electron due to the wurtzite crystal. Assuming a perfect bulk crystal, the material is periodic in the unit cell, so that the wave function ψ must have the form:

$$|\psi(\boldsymbol{r})|^2 = |\psi(\boldsymbol{r} + \boldsymbol{R}))|^2, \tag{2.2}$$

where $\boldsymbol{R}$ is a unit vector. One of the most important results of solid state physics is the realization that the periodicity of the wavefunction in equation 2.2 implies that the eigenstates of the bulk crystal can be written in the Bloch form [11, 58, 59]:

$$\psi_{n,\boldsymbol{k}}(\boldsymbol{r}) = e^{i\boldsymbol{k}\cdot\boldsymbol{r}} u_{n,\boldsymbol{k}}(\boldsymbol{r}). \tag{2.3}$$

The function $u_{n,\boldsymbol{k}}(\boldsymbol{r})$ is an extended state that has the same periodicity as the unit cell and is modulated by the envelope function $e^{i\boldsymbol{k}\cdot\boldsymbol{r}}$. The Bloch state $\psi_{n,\boldsymbol{k}}(\boldsymbol{r})$ is an extended state that spans the entire crystal volume. The vector $\boldsymbol{k}$ is known as the crystal momentum, which is not the actual momentum of an electron in the crystal, but plays the role of the electron momentum when an external force is applied to the electron inside the crystal. That is, the electron residing inside the crystal responds to an external force as if it had a momentum magnitude given by $\hbar|\boldsymbol{k}|$. The index n in the wave function $\psi_{n,\boldsymbol{k}}(\boldsymbol{r})$ arises due to the periodic boundary condition

$$u_{\boldsymbol{k}}(\boldsymbol{r}) = u_{\boldsymbol{k}}(\boldsymbol{r} + \boldsymbol{R}), \tag{2.4}$$

required by the cell-periodic part of the wave function. The periodic boundary condition gives rise to an infinite number of eigenvalues of equation 2.1 for a given $\boldsymbol{k}$ that are each labeled by an index n. Typically, periodic boundary conditions at the bulk crystal interfaces (also known as the Born-von Karman boundary conditions) are also assumed [59]. With the Born-von Karman boundary conditions, the allowed values of $\boldsymbol{k}$ are discrete, where the volume in k-space per allowed value of $\boldsymbol{k}$ ($\Delta\boldsymbol{k}$ is given by

$$\Delta\boldsymbol{k} = \frac{(2\pi)^3}{V}, \tag{2.5}$$

where V is the crystal volume. Typically the crystal volume is taken to be large enough so that the dispersion relation $E(\boldsymbol{k})$ can be approximated as a continuous band. Therefore, the dispersion of bulk crystals can contain an infinite number of continuous energy bands, each designated by the index n.

Although equation 2.2 represents a lot of progress in understanding the form of the wave function in a bulk crystal, calculating the exact form of the infinite set of cell-periodic wave functions $u_{n,\boldsymbol{k}}(\boldsymbol{r})$ and the associated energy eigenvalues as a function of $\boldsymbol{k}$ remains a daunting task. Nevertheless, there exist several methods that are used extensively for calculating the approximate band structure of materials such as the tight binding method [60], augmented plane wave method [61, 62] and $\boldsymbol{k}\cdot\boldsymbol{p}$ method [63, 64]. Most of the time, calculations performed using these techniques are semi-empirical and/or approximate for a given band. A band structure calculation from ref. [3] of wurtzite GaN using a variation of the augmented plane wave method is shown in Fig. 2.1, plotted as a function of $\boldsymbol{k}$ along high symmetry directions of the crystal lattice. Although the full band structure calculation in principle involves solving for an infinite number of bands, a good approximation to the crystal band structure can be found by solving for a finite number of bands (usually $\sim$10).

The population of electrons $n_e(T)$ in each energy band at a given temperature T and energy E follows the Fermi-Dirac distribution:

$$n_e(T) = \frac{1}{e^{(E-E_F)/k_BT}+1}. \tag{2.6}$$

In intrinsic semiconductor materials the Fermi energy E_F occurs in the middle of two energy bands known as the valence band and the conduction band. In direct band

gap semiconductor materials such as wurtzite, the highest energy point in the valence band and the lowest energy point in the conduction band both exist at $\boldsymbol{k} = 0$, also known as the Γ point, as shown in Fig. 2.1. The energy difference between the lowest part of the conduction band and highest part of the valence band is known as the band gap.

For most optical absorption/emission applications in direct-gap semiconductors, we are only interested in characterizing the electronic band structure only near the Γ point. As we will see later on, the band structure of direct gap quantum confined systems that are mainly of interest in this work can be described accurately with a knowledge of the cell perioidic wave functions $u_{\boldsymbol{k},n}$ and band curvatures at the Γ point. Also, in direct gap materials, electrons excited to higher energy states within the conduction band (holes excited to lower energy states within the valence band) quickly decay, for example by emitting phonons, to the lowest energy point in the conduction band (highest energy point in the valence band). The electrons and holes usually only have time to radiatively recombine once they reach the lowest energy point. Hence, most of the action in optical applications occurs at or near the Γ point in bulk and quantum confined semiconductors.

Close inspection of Fig. 2.1 reveals that the valence band of wurtzite materials is actually composed of 3 separate bands. Each of the bands is doubly degenerate in spin. The first two bands are degenerate at the Γ points and normally labeled as the A and B valence bands, and the third is split from the A and B bands and labeled as the C band. Note that in zinc blende material, there exist 3 degenerate valence bands in the absence of spin orbit coupling. The fact that the C band is split from the A and B bands in the absence of spin-orbit coupling reflects the lower symmetry in the wurtzite unit cell compared to zinc blende. For optical applications, the C band is typically ignored.

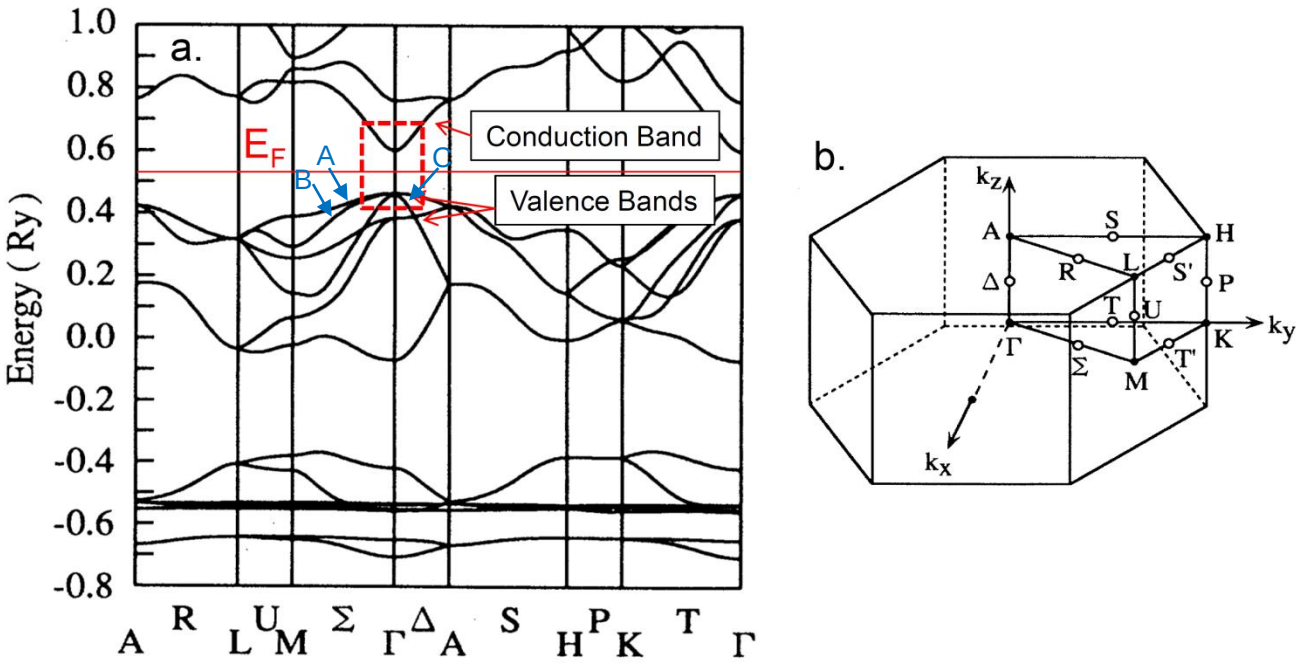

Figure 2.1: a. Bandstructure calculation of GaN using a variation of the augmented plane wave method (full-potential linearized augmented plane wave method). The figure is modified from Ref. [3]. b. First Brillouin zone of GaN wurtzite crystals. Figure is reproduced from Ref. [3]

One very important point to note is that the valence electrons in the constituent atoms that compose III-Nitride wurtzite semiconductors (In, Al, Ga, N) are in the atomic s and p orbitals. Electrons that reside in the valence and conduction bands of bulk semiconductors retain similar properties to the valence electrons in the constituent atoms. It turns out that at the Γ point, the conduction band in direct-gap semiconductors can be mapped to an atomic $|S\rangle$ function, while the valence bands can be mapped to a linear combination of atomic $|P\rangle$ functions [11]. To be clear: it should be kept in mind that angular momentum is generally not a good quantum number in the wurtzite system. The electron (say in the conduction band) can be described near k = 0 using an atomic $|S\rangle$-like state, but the assumption from the tight-binding technique is that the electron is an extended state and the full wave function is essentially the atomic $|S\rangle$-like function repeated over every lattice site in

the crystal [11]. The symmetries of the electronic states can be better understood using group theory techniques [65].

2.1.1 Introduction to the effective mass and the $\boldsymbol{k}\cdot\boldsymbol{p}$ method

If one is only interested in optical interactions near the Γ point, an accurate and convenient method for calculating the approximate bandstructure (that is, the dispersion relation E($\boldsymbol{k}$) and the electronic eigenstates) is the $\boldsymbol{k}\cdot\boldsymbol{p}$ method. The $\boldsymbol{k}\cdot\boldsymbol{p}$ method is very popular because terms in the electron Hamiltonian resulting from quantum confinement, strain and Coulomb interactions can be more easily incorporated into the bandstructure calculation compared to other methods. In this section, some results of $\boldsymbol{k}\cdot\boldsymbol{p}$ calculations from the literature for wurtzite III-Nitride materials are featured, incorporating spin-orbit coupling and strain. Prior to a presentation of some calculation results, the basic elements of the $\boldsymbol{k}\cdot\boldsymbol{p}$ method are mentioned. In the next section, quantum confinement effects will be added. At the heart of the $\boldsymbol{k}\cdot\boldsymbol{p}$ method in confined structures is the concept of the effective mass, which is related to the curvature of the conduction band (for electrons) and valence bands (for holes).

The $\boldsymbol{k}\cdot\boldsymbol{p}$ method when applied near the Γ point begins by rewriting Schrödinger's equation in terms of only the cell-periodic part of the Bloch wave function:

$$(\frac{p^2}{2m_e}+V(r)+\frac{\hbar}{m_e}\boldsymbol{k}\cdot\boldsymbol{p}+\frac{\hbar^2k^2}{2m_e})u_{n,\boldsymbol{k}}(\boldsymbol{r})=E_{n,\boldsymbol{k}}(\boldsymbol{r})u_{n,\boldsymbol{k}}(\boldsymbol{r}). \tag{2.7}$$

The essential idea is to treat the terms $\frac{\hbar}{m_e}\boldsymbol{k}\cdot\boldsymbol{p}+\frac{\hbar^2k^2}{2m_e}$ as a perturbation and to obtain an approximate solution to equation 2.7 using second-order perturbation theory. If we consider a single band labeled v that is relatively isolated in energy compared to other bands, such as the conduction band in wurtzite (ignorning spin), then the dispersion relation (band structure) is approximately given by:

$$E_{v,\boldsymbol{k}}\approx E_{v,k=0}+\frac{\hbar^2k^2}{2m_e}+\frac{\hbar^2}{m_e^2}\sum_{n\neq n'}\frac{|\boldsymbol{k}\cdot\langle n',k=0|\,\boldsymbol{p}\,|v,k=0\rangle\,|^2}{E_{v,k=0}-E_{n',k=0}}, \tag{2.8}$$

where $|v,\boldsymbol{k}\rangle$ is the cell-periodic wave function and the sum over $n^{'}$ gives the energy correction due to all other bands. One of the most important parameters that emerges

from equation 2.8 is the effective mass, given by

$$\frac{m_e}{m^*_{i,j}} = \delta_{i,j} + \frac{2}{m_e} \sum_{n \neq n'} \frac{\langle v, \boldsymbol{k}=0 | \, p_i \, | n', \boldsymbol{k}=0 \rangle \langle n', \boldsymbol{k}=0 | \, p_j \, | v, \boldsymbol{k}=0 \rangle}{E_{v,k=0} - E_{n',k=0}}. \tag{2.9}$$

Note that results that are obtained using the $\boldsymbol{k} \cdot \boldsymbol{p}$ method are only useful if the wave functions $u_{v,\boldsymbol{k}=0}$ and energies $E_{v,\boldsymbol{k}=0}$ are known, which usually requires assistance from experimental results. Most of the time, the effective mass tensor $m_{i,j}$ is averaged over the 6 different possible combinations of i and j corresponding to the different x,y and z spatial directions. The resulting averaged effective mass is then used to describe a single band.

It is important to understand that the elements of the $\boldsymbol{k} \cdot \boldsymbol{p}$ method discussed above apply only to a single, non-degenerate band. For degenerate bands, the perturbation technique must be modified since the resonant denominator in equation 2.8 contains a singularity. The theoretical description of the effective mass is also modified. The degenerate perturbation technique for direct-gap materials, outlined in a seminal paper by Luttinger and Kohn [63], involves expanding the wave function using the Bloch functions at the Γ point as the basis states, then diagonalizing the submatrix spanned by those states, including strain and spin-orbit terms in the Hamiltonian. Usually only the conduction band and three valence bands are kept in the expansion, so typically the method is referred to as the 8x8 $\boldsymbol{k} \cdot \boldsymbol{p}$ method (for the four doubly degenerate conduction and valence bands).

2.1.2 Results of the $\boldsymbol{k} \cdot \boldsymbol{p}$ method including spin-orbit and strain

The spin-orbit effect adds an additional component to the electron Hamiltonian in the bulk crystal, given by [66]

$$H_{SO} = \frac{\hbar}{4c^2 m^2} \boldsymbol{\nabla V} \times \boldsymbol{p} \cdot \boldsymbol{\sigma}, \tag{2.10}$$

where $\boldsymbol{V}$ is the crystal potential and $\boldsymbol{\sigma}$ is the Pauli spin operator. The results of a calculation of the energy eigenvalues at k = 0 incorporating spin-orbit effects is reproduced from Ref. [4] in Fig. 2.2. The energies of the valence band states in Fig.

2.2 are E_1^0, the energy of the A band, E_2^0, the energy of the B band, and E_3^0, the energy of the C band. The energy splitting parameters in Fig. 2.2 are $\Delta_1 = \Delta_{CR}$, where Δ_{CR} is the crystal field energy splitting and $\Delta_2 = \Delta_3 = \frac{1}{3}\Delta_{SO}$, where Δ_{SO} is the spin-orbit energy correction. As mentioned earlier, the crystal field energy splitting is a consequence of the symmetry properties in the wurtzite crystal structure. One consequence of the spin-orbit interaction is that the degeneracy between the A and B bands is lifted.

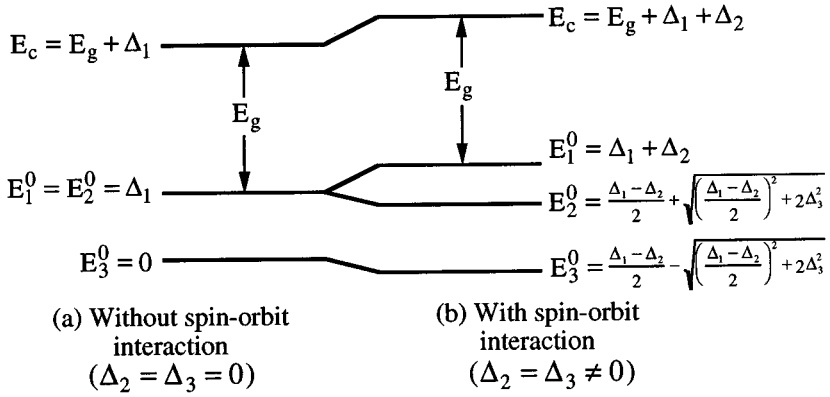

Figure 2.2: Energy level diagram at the Γ point with and without spin-orbit terms included. The energies of the valence band states are E_1^0, the energy of the A band, E_2^0, the energy of the B band, and E_2^0, the energy of the C band. The energy splitting parameters are $\Delta_1 = \Delta_{CR}$, where Δ_{CR} is the crystal field energy splitting and $\Delta_2 = \Delta_3 = \frac{1}{3}\Delta_{SO}$, where Δ_{SO} is the spin-orbit energy correction. The figure was reproduced from ref. [4].

When a layer of InGaN is coherently grown on top of a layer of GaN, the lattice constant of the InGaN layer must shrink in order to match the GaN layer without the formation of a defect, a result of the lower lattice constant in InN crystals compared to GaN crystals. This introduces compressive strain in the InGaN layer with the level of strain dependent on the InN concentration within the InGaN layer. The strain introduces new terms in the Hamiltonian that can be described using deformation potential theory [11]. Qualitatively, two of the major effects of compressive strain in wurtzite are the increase of the band gap and the separation and mixing of valence band states. Here we will focus on the separation and mixing of valence band states for different strain fields, but it should be remembered that the band gap also increases

when a strain is added.

We now examine the results of the $\boldsymbol{k} \cdot \boldsymbol{p}$ calculation including points in $\boldsymbol{k}$ space away from the Γ point and including strain effects. As mentioned earlier, although the conduction and valence band wave functions at $\boldsymbol{k} = 0$ are extended states in bulk, they can be mapped to atomic $|S\rangle$ and $|P\rangle$ wave functions, respectively. In the case of wurtzite material, the conduction band wave function ($\sim |S\rangle$) is unchanged with the addition of strain and spin-orbit coupling but the valence band states are mixed and are given by different linear combinations of the $|P\rangle$ wave functions depending on the strain directions. This is exemplified in a calculation of the valence band states and band structure using the 8x8 $\boldsymbol{k} \cdot \boldsymbol{p}$ method, as shown in Fig. 2.3, a figure from the Ph.D thesis of Momme Winkelnkemper [5, 67]. The top panel of Fig. 2.3 shows the resulting band structure when only spin-orbit coupling is included. The constants a and b are given by

$$a = \frac{1}{\sqrt{x^2 + 1}} \tag{2.11}$$

and

$$b = \frac{x}{\sqrt{x^2 + 1}}, \tag{2.12}$$

where

$$x = \frac{\sqrt{2}}{\sqrt{3}} \frac{-(\Delta_1 - \Delta_2) + \sqrt{(\Delta_1 - \Delta_2)^2 + 8\Delta_2^2}}{\Delta_2}. \tag{2.13}$$

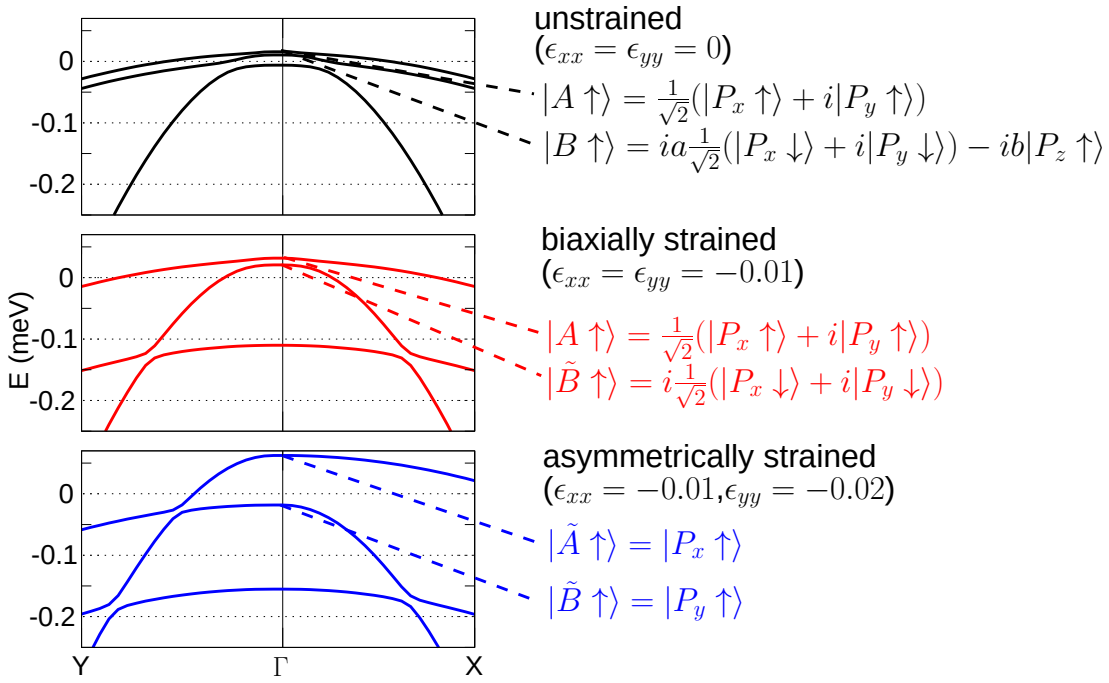

Figure 2.3: Results of the $\boldsymbol{k}\cdot\boldsymbol{p}$ calculation from Ref. [5] for different values of strain.

With the addition of biaxial compressive strain to the Hamiltonian, such as the strain perpendicular to the growth axis in a layer of InGaN grown on GaN, the nature of the A and B states changes dramatically compared to the unstrained case due to band mixing effects. It is very interesting to note the dramatic changes in the wave functions if the biaxial strain is even along the x and y directions (where in our case the z direction is given by the growth or $\boldsymbol{c}$ axis direction) shown in the middle panel of Fig. 2.3 compared to an uneven biaxial strain, shown in the bottom panel of Fig. 2.3. It is also interesting to note the energy splittings of the A, B and C bands for even biaxial and uneven biaxial strain. For even biaxial strain, the separation between the A and B valence bands does not significantly change, unlike in other crystal configurations such as zinc-blende, while the band gap and separation between the B and C bands increases. For an asymmetrically strained system, such as a typical

quantum dot, the separation between the A and B bands is strongly sensitive to the amount of strain in the system. Later on we will examine the effects of strain on the optical selection rules in wurtzite materials.

2.2 Modeling quantum confined exciton wave functions using the effective mass approximation

The concept of the effective mass allows us to simplify bandstructure calculations of quantum confined systems in direct band gap semiconductors assuming the cell periodic wave functions are known at the Γ point.

For a quantum confined semiconductor system, we write the energy equation as

$$(H_0 + U)\psi = E\psi \tag{2.14}$$

where H_0 is the Hamiltonian experienced by a single electron within the bulk crystal including effects such as spin-orbit coupling or strain, and U represents a confinement potential.

As long as the potential U does not vary significantly over the dimension of the unit cell, Luttinger and Kohn [63] showed, using $\boldsymbol{k}\cdot\boldsymbol{p}$ perturbation theory techniques, that near $\boldsymbol{k} = 0$ the wave function for the confined electron in equation 2.14 can be written to good approximation as

$$\psi(\boldsymbol{r}) = \sum_n F_n(\boldsymbol{r}) u_{n,\boldsymbol{k}=0}(\boldsymbol{r}). \tag{2.15}$$

where $F_n(\boldsymbol{r})$ is an envelope function. In this study, we are interested in the quantum confined exciton wave function, where exciton is in this instance a general term for a correlated electron-hole pair. The above wave function is therefore generally given for Wannier excitons as [68]

$$\psi(\boldsymbol{r}) = \sum_n F_n(\boldsymbol{r_e}, \boldsymbol{r_h}) u_{n,\boldsymbol{k}=0}(\boldsymbol{r_e}) u_{n,\boldsymbol{k}=0}(\boldsymbol{r_h}), \tag{2.16}$$

where $\boldsymbol{r_h}$ and $\boldsymbol{r_e}$ describe the coordinates of the hole and electron state. For illustration, we assume that the correlated, confined electron-hole pair exists in a non-degenerate band that is well-separated in energy from other bands. In this case, the

envelope function Fn($\boldsymbol{r_e}$,$\boldsymbol{r_h}$) follows a Schrödinger-like equation

$$(-\frac{\hbar^2\nabla_e^2}{2m_e^*} - \frac{\hbar^2\nabla_h^2}{2m_h^*} + U(\boldsymbol{r_e}, \boldsymbol{r_h}))F_n(\boldsymbol{r_e}, \boldsymbol{r_h}) = E_n F_n(\boldsymbol{r_e}, \boldsymbol{r_h}), \tag{2.17}$$

where $m^*_{e(h)}$ is the effective mass electron(hole) for the band. For a more accurate description of the dynamics in degenerate bands, equation 2.17 must be solved using techniques similar to the 8x8 $\boldsymbol{k}\cdot\boldsymbol{p}$ method.

2.2.1 Exciton wave functions in bulk

It is useful to first mention the exciton in bulk. Due to the Coulomb interaction between electrons and holes that can be excited in bulk semiconductors, some electron-hole pairs can become bound together into quasi-particles known as excitons. The energy states of the excitons appear below the bandedge [69] and are qualitatively identical to positronium [11].

We again assume that the electron and hole that compose the exciton exist in non-degenerate and well isolated energy bands for illustration. In this case, the confinement potential U in equation 2.17 is provided by the Coulomb potential and equation 2.17 can be rewritten as [11]

$$(-\frac{\hbar^2\nabla_e^2}{2m_e^*} - \frac{\hbar^2\nabla_h^2}{2m_h^*} + \frac{e^2}{4\pi\epsilon|\boldsymbol{r_e} - \boldsymbol{r_h}|})F_n(\boldsymbol{r_e}, \boldsymbol{r_h}) = E_n F_n(\boldsymbol{r_e}, \boldsymbol{r_h}). \tag{2.18}$$

It is useful to move to center-of mass coordinates so that the Hamiltonian in equation 2.18 can be rewritten as

$$H = \frac{\hbar^2 K^2}{2(m_e^* + m_h^*)} + \frac{\hbar^2 k^2}{2m_r^*} + \frac{e^2}{4\pi\epsilon|\boldsymbol{r}|}, \tag{2.19}$$

where

$$\boldsymbol{r} = \boldsymbol{r_e} - \boldsymbol{r_h}, \tag{2.20}$$

$$\boldsymbol{K} = \boldsymbol{k_e} - \boldsymbol{k_h}, \tag{2.21}$$

$$\boldsymbol{k} = \frac{m_e^*\boldsymbol{r_e} + m_h^*\boldsymbol{r_h}}{m_e^* + m_h^*} \tag{2.22}$$

and

$$m_r^* = \frac{m_e^* m_h^*}{m_e^* + m_h^*}. \tag{2.23}$$

Using existing techniques for solving for the hydrogen atom wave functions, the resulting exciton wave function can be written as

$$\psi_n = e^{i\boldsymbol{K}\cdot\boldsymbol{R}} F(\boldsymbol{r}) u_{c,\boldsymbol{k}=0}(\boldsymbol{r_e}) u_{v,\boldsymbol{k}=0}(\boldsymbol{r_h}), \tag{2.24}$$

where F($\boldsymbol{r}$) can be mapped to the atomic wave functions ψ_{nlm} with the usual constants such as m_e replaced by their excitonic counterparts m_r^*.

One component of the exciton energy is given by the hydrogen-like solution:

$$E_1 = -\frac{m_r^* e^4}{2(4\pi\epsilon)^2\hbar^2}\frac{1}{n^2} + \frac{\hbar^2}{2(m_e^* + m_h^*)}K^2. \tag{2.25}$$

At K = 0, the eigenenergies are qualitatively identical to positronium. The exciton binding energy is given by the separation between the band edge and the lowest energy exciton state at K = 0, which is the the magnitude of the first term on the right hand side of equation 2.25 for n = 1. The bulk exciton forms a band of states based on the continuum of allowed $\boldsymbol{K}$ values. It is important to note that the full exciton energy contains more terms in addition to energy given in equation 2.25 due to the Fermionic nature of the electron and hole. A more general solution must include effects such as electron-hole exchange [70] for example.

Although the bulk exciton is an extended state in the crystal, it is still useful to define a characteristic length which describes the proximity of the electron and hole wave functions. The exciton Bohr radius provides this length scale, in the same way that the Bohr radius describes the characteristic length between the nucleus and electron cloud in a hydrogen atom. The exciton Bohr radius is related to the Bohr radius a_B by $a_{ex} = (\epsilon m_e/\epsilon_0 m_r^*)a_B$, where ϵ is the permittivity of the material. Compared to many other conventional compound semiconductors, the exciton Bohr radius of bulk III-nitrides is typically smaller and the exciton binding energy is typically larger. For example, the exciton Bohr radius and binding energy in bulk GaAs is $\sim$300 $\mathring{A}$ and $\sim$4.2 meV, respectively, [71] and the exciton Bohr radius and binding energy in bulk GaN is $\sim$30 $\mathring{A}$ and $\sim$22 meV, respectively [72, 73]. As a result of the relatively large exciton binding energy, excitons in III-nitride materials are much more resilient to thermal ionization processes compared to other conventional materials.

2.2.2 Quantum dot and quantum well exciton wave functions

In semiconductor heterostructures and nanostructures such as quantum wells or quantum dots, the material can provide a source of physical confinement for the electron and hole. Generally, the degree of confinement for the electron and hole can be different. We will therefore modify the bulk exciton energy in equation (2.18 for a quantum dot or quantum well to include the confinement effects:

$$(-\frac{\hbar^2\nabla_e^2}{2m_e^*} - \frac{\hbar^2\nabla_h^2}{2m_h^*} + \frac{e^2}{4\pi\epsilon|\boldsymbol{r_e}-\boldsymbol{r_h}|} + V_{conf}(\boldsymbol{r_e}) + V_{conf}(\boldsymbol{r_h}))F_n(\boldsymbol{r_e},\boldsymbol{r_h}) = E_nF_n(\boldsymbol{r_e},\boldsymbol{r_h}). \tag{2.26}$$

If an exciton is confined to a small volume in space compared to the exciton Bohr radius, also known as the strong confinement regime, the continuous exciton energy bands become quantized. Quantum confinement can occur inside a small volume of one semiconductor material with a band gap E_{g1} that is contained within another semiconductor material with bandgap E_{g2} with $E_{g2} > E_{g1}$. The smaller band gap material is referred to as a quantum dot in this situation, generally assuming strong confinement.

We will ignore the Coulomb interaction between the electron and hole for the moment. If the Coulomb interaction is left out, the electron and hole wave functions can be solved for separately in equation 2.26. In the limit that E_{g2} becomes infinite, the envelope functions $F_n(\boldsymbol{r_e})$ and $F_n(\boldsymbol{r_h})$ can be solved using well-known 3-D particle in an infinite square well (or usually a spherical well) techniques to obtain analytical results except that the normal single particle mass is substituted with the effective mass. The eigenenergies of a conduction band electron in a 3-D cubic box with side lengths L are given by

$$E_{nx,ny,nz} = \frac{\hbar^2\pi^2}{2m_c^*L^2}(n_x^2 + n_y^2 + n_z^2). \tag{2.27}$$

If E_{g2} is finite, numerical calculations can be used to solve for the eigenfunctions and eigenenergies of the envelope function. In the strong confinement regime, the potential provided by the quantum confinement tends to provide a much more significant correction to the electron-hole Hamiltonian compared to the Coulomb correction in

equation 2.18 since the confinement energy scales like L^{-2} and the Coulomb energy scales as L^{-1}, where L is the characteristic length of the system [74]. In the case of very strong quantum confinement, the energy correction due to the Coulomb potential can be ignored.

In many real quantum dot systems, the quantum dot geometry differs strongly from the ideal rectangular or spherical potential well. Semiconductor quantum dots in this study form as a result of a strain relaxation process and the exact dimensions are usually unknown. Furthermore, in many cases the dots have a lateral dimension that exceed the exciton Bohr radius. In this case, the quantum dot is in an intermediate confinement regime and both the Coulomb and confinement terms must be included in the overall Hamiltonian. For these reasons, it is usually difficult to obtain an accurate theoretical description of quantum dot band structure parameters. At the same time, we will see in later sections that the envelope function techniques can be useful to observe qualitative effects of perturbations such as internal electric fields and strain.

2.3 Internal electric fields in InGaN/GaN heterostructures

Wurtzite GaN/InGaN/GaN quantum confined heterostructures grown along the c-axis are known for large internal electric fields. One contributor to the internal electric fields is the non-zero spontaneous (or pyroelectric) polarizations that can develop in the GaN and InGaN layers. Alternating layers of InGaN and GaN have generally different electric polarizations and the difference in the polarization magnitudes results in a sheet of charge along the InGaN/GaN interface causing the heterostructure to behave like a parallel plate capacitor. Furthermore, piezoelectric effects due to strain also leads to a sheet charge at the InGaN/GaN interface. As we will see, the magnitude of the internal electric field resulting from spontaneous polarization is generally much lower than the piezoelectric polarization in InGaN/GaN.

As can be seen from the wurtzite lattice in Fig. 2.4, some of the atoms comprising the unit cell are bonded in a tetragonal configuration. In GaN, the Ga and N atoms

are bonded together at the apex of two oppositely facing tetragons. There is a large difference in electronegativity between Ga and N (Ga = 1.81 and N = 3.04), therefore a nonzero polarization can be developed as electrons are pulled more toward the N side. This polarization is referred to as the pyroelectric or spontaneous polarization. In a random crystal model of InGaN, an In atom can replace a Ga atom in the unit cell with a likelihood of replacement given by the In doping concentration. The electronegativity of In is 1.78, which is very similar to Ga (1.81), therefore successive layers of InGaN and GaN do not usually have a large difference in polarization.

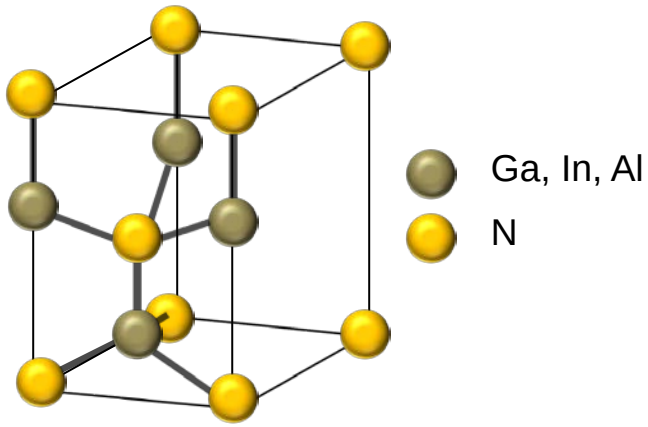

Figure 2.4: Unit cell of III-nitride wurtzite materials

As stated earlier, for InGaN layers grown along the ***c*** axis, strain occurs in the orthogonal directions to the ***c*** axis due to the lower lattice constant of InN compared to GaN. A compressive strain necessarily leads to a strain along the ***c*** axis direction as well, with the proportion of strain along the perpendicular axes given by Poisson's ratio:

$$\epsilon_{zz} = -2\frac{c_{13}}{c_{33}}\epsilon_{xx}, \tag{2.28}$$

where z is along the ***c*** axis direction, ϵ_{ij} is the strain tensor, and c_{ij} is a constant. The strain along the ***c*** axis pushes apart the N and Ga(In) atoms leading to a larger separation between the positive and negative charges in the lattice generated by the difference in electronegativity and an induced piezoelectric polarization. As we will see, this effect results in a significant internal electric field in the InGaN layer.

For illustration, we numerically calculate the electron and lowest energy hole envelope functions in a 1-D GaN/$In_{0.5}Ga_{0.5}N$/GaN quantum well grown along the $\boldsymbol{c}$ axis. The lattice constant of GaN is a = 3.18 $\mathring{A}$ along the $\boldsymbol{a}$ axis and the lattice constant of $In_{0.5}Ga_{0.5}N$ is a = 3.36 $\mathring{A}$ along the $\boldsymbol{a}$ axis, assuming the virtual crystal approximation [11]. The strain magnitude in the x in y direction is therefore given by $\epsilon_{xx} = \epsilon_{yy} = \frac{3.36}{3.175}$ - 1 = 0.058. From Poisson's ratio, the strain in the growth direction ($\boldsymbol{c}$ axis) is given by ϵ_{zz} = -0.035, where c_{13} and c_{33} are given by 10.9×10^{11} $\frac{N}{m^2}$ and 35.5×10^{11} $\frac{N}{m^2}$, respectively. The piezoelectric polarization generated at the heterostructure interface is given by $P_{PZ} = e_{33}\epsilon_{zz} + e_{31}(\epsilon_{xx} + \epsilon_{yy}) = 0.054\ C/m^2$, where the piezoelectric constants e_{33} and e_{31} are given by 0.73 C/m^2 and -0.49 C/m^2, respectively. The spontaneous polarization of GaN and $In_{0.5}Ga_{0.5}N$ at the interfaces are given by 0.029 C/m^2 and 0.0305 C/m^2, respectively. The resulting internal electric field magnitudes from the difference in spontaneous polarization values between the InGaN and GaN layers and is (0.14 $\times10^6$ V/m). The resulting internal electric field from the piezoelectric polarization is given by (-5.72 $\times10^6$ V/m). The spontaneous and piezoelectric fields are pointing in opposite directions along the growth axis, as shown in Fig. 2.5a. As stated earlier, the magnitude of the piezoelectric field is much larger than the magnitude of the electric field generated from spontaneous polarization effects due primarily to the small difference in electronegativity between In and Ga. In table 2.1, some parameters that may be useful for calculations involving strain in InGaN/GaN heterostructures are listed.

Assuming the above internal electric field values with directions shown in Fig. 2.5a, the electron and hole envelope functions are solved numerically using software written by Jasprit Singh and John Hinckley at the University of Michigan. The calculation uses the scalar approximation, meaning that the electron and hole wave functions are assumed to be in isolated, non-degenerate energy bands. The calculation also assumes ignores the Coulomb interaction between the electron and hole, so that the electron and hole wavefunctions are separately solved for each band. In the calculation, one InGaN/GaN interface is held at ground, while the other is biased to a suitable voltage to account for the internal electric fields. This explains the uneven

Parameter	***Name***	***Value***	***Reference***
E_G GaN	Wurtzite GaN Bandgap 0 K	3.47 eV	[75]
E_G InN	Wurtzite InN Bandgap 300 K	0.76 eV	[76]
a GaN	Lattice constant (a) GaN 300 K	3.189 angstroms	[77]
c GaN	Lattice constant (c) GaN 300 K	5.185 angstroms	[77]
a InN	Lattice constant (a) InN 300 K	3.5446 angstroms	[78]
c InN	Lattice constant (c) InN 300 K	5.7034 angstroms	[78]
e_{33} GaN	GaN piezoelectric constant	0.73 C/m^2	[79]
e_{31} GaN	GaN piezoelectric constant	-0.49 C/m^2	[79]
e_{33} InN	InN piezoelectric constant	0.97 C/m^2	[79]
e_{31} InN	InN piezoelectric constant	0.57 C/m^2	[79]
c_{33} GaN	elastic modulus GaN	10.9×10^{11} N/m^2	[80]
c_{31} GaN	elastic modulus GaN	35.5×10^{11} N/m^2	[80]
c_{33} InN	elastic modulus InN	12.1×10^{11} N/m^2	[81]
c_{31} InN	elastic modulus InN	18.2×10^{11} N/m^2	[81]

Table 2.1: Optoelectronic constants of InN and GaN

shape of the valence and conduction bands in Fig. 2.5b. The calculated electron and hole wave functions are shown in Fig. 2.5b. It should be noted that the band bending caused by the internal electric fields pushes the centroid of the lowest energy electron and hole wave functions to the top and bottom of the quantum well. This is a manifestation of the quantum confined Stark effect [82] that also leads to a red shift of the electron-hole transition energy compared to the quantum well with no internal fields. Next, we note that the internal electric fields make the system very sensitive to small changes in the thickness of the InGaN region. A fluctuation of the InGaN region by only 0.1 nm results in a change in the transition energy ΔE $\approx$ 29 meV. In 2-D InGaN/GaN structures such as quantum wells, the injection of carriers into the InGaN active region partially screens the internal electric field and the quantum confined Stark effect is partly canceled [83,84] resulting in a blue shift of the transition

energy and an increase in electron-hole overlap. It has been suggested that this effect can be used to create devices such as electro-absorption modulators in InGaN/GaN quantum well systems [85].

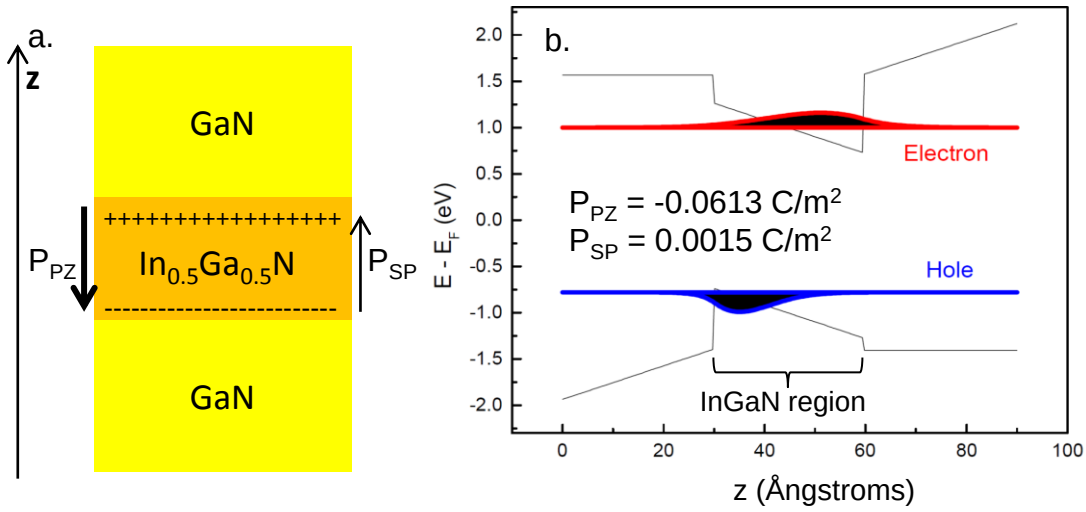

Figure 2.5: a. Schematic of the InGaN/GaN heterostructure used in the calculation. The sign of the charge accumulation and the directions of the piezoelectric and spontaneous polarizations is also shown. b. Plot of the calculated lowest energy electron and hole envelope functions.

2.4 Optical interactions in wurtzite InGaN quantum confined structures

Thus far the focus of this chapter has been on the electronic properties of wurtzite materials. In this section, we will entirely shift the discussion to introduce the interaction between optical fields and wurtzite semiconductor materials. This section will be mainly focused on an understanding of the initial steps for calculating transition matrix elements and the corresponding selection rules. In the next chapter, a more detailed approach will be given to the nonlinear interactions in the samples featured in this thesis.

2.4.1 Transition matrix elements

The Hamiltonian for an electron in a crystal interacting with a transverse electric field is given by

$$H = \frac{1}{2m_e}(\boldsymbol{p} - e\boldsymbol{A})^2 + V(\boldsymbol{r}), \tag{2.29}$$

where $V(\boldsymbol{r})$ is the crystal potential and $\boldsymbol{A}$ is the vector potential of the electric field. It is often convenient to rewrite equation 2.29 using the dipole approximation and working in the Coulomb gauge so that $\boldsymbol{\nabla} \cdot \boldsymbol{A} = 0$. In this case the field interaction term is simply

$$H_{int} = \frac{ie\hbar}{m_e}\boldsymbol{A} \cdot \boldsymbol{\nabla}, \tag{2.30}$$

Many quantities of physical interest, such as the spontaneous emission rate and linear absorption strength of excitons require knowledge of the square of transition matrix elements $|\langle j| H_{int} |i\rangle|^2$, where $|i\rangle$ is the wave function of the electron in the valence band and $|j\rangle$ represents the conduction band electron wave function. In a semiconductor quantum dot, the wave functions $|i\rangle$ and $|j\rangle$ are given by $F_n(\boldsymbol{r})u_{n,\boldsymbol{k}=0}(\boldsymbol{r})$, where n represents either the conduction or valence band and $F_n(\boldsymbol{r}$ is the envelope wave function. The optical transition matrix elements are therefore proportional to

$$\begin{aligned} |\langle j| H_{int} |i\rangle|^2 \propto \int F_v^*(\boldsymbol{r})u_{v,\boldsymbol{k}=0}(\boldsymbol{r})^* F_c(\boldsymbol{r})\boldsymbol{A} \cdot \boldsymbol{\nabla} u_{c,\boldsymbol{k}=0}(\boldsymbol{r})d^3\boldsymbol{r} + \\ \int u_{v,\boldsymbol{k}=0}(\boldsymbol{r})^* F_v^*(\boldsymbol{r})u_{c,\boldsymbol{k}=0}(\boldsymbol{r})\boldsymbol{A} \cdot \boldsymbol{\nabla} F_c(\boldsymbol{r})d^3\boldsymbol{r}. \end{aligned} \tag{2.31}$$

In each term in equation 2.31, the integrals over the rapidly varying cell periodic wave functions and the slowly varying envelope functions can be separated [86], leading to

$$\begin{aligned} |\langle j| H_{int} |i\rangle|^2 \propto \int F_v^*(\boldsymbol{r'})F_c(\boldsymbol{r'})d^3\boldsymbol{r'} \int u_{v,\boldsymbol{k}=0}(\boldsymbol{r})^* \boldsymbol{A} \cdot \boldsymbol{\nabla} u_{c,\boldsymbol{k}=0}(\boldsymbol{r})d^3\boldsymbol{r} + \\ \int u_{v,\boldsymbol{k}=0}(\boldsymbol{r'})^* u_{c,\boldsymbol{k}=0}(\boldsymbol{r'})d^3\boldsymbol{r'} \int F_v^*(\boldsymbol{r})\boldsymbol{A} \cdot \boldsymbol{\nabla} F_c(\boldsymbol{r})d^3\boldsymbol{r}. \end{aligned} \tag{2.32}$$

The second term on the right hand side of equation 2.32 is zero, since the conduction and valence band wave functions are orthogonal. This gives way to a compact expression for calculating the interband transition elements, proportional to

$$|\langle F_v|F_c\rangle|^2 \langle u_{v,\boldsymbol{k}=0}| \boldsymbol{A} \cdot \boldsymbol{p} |u_{c,\boldsymbol{k}=0}\rangle|^2. \tag{2.33}$$

Note now that there are two components that determine the optical selection rules in equation 2.33: the inner product of the envelope function states and the momentum matrix elements between the zone center states. A large negative side-effect of the internal electric fields in InGaN heterostructures is the decrease in the wave function overlap between the lowest energy electron and hole states due to the quantum confined Stark effect that leads to a lower emission and absorption efficiency.

2.4.2 Optical selection rules

For simplicity, we will assume here that there is sufficient overlap between the envelope wave functions so that the inner product $\langle F_v|F_c\rangle$ is nonzero and focus instead on the selection rules due to the zone center Bloch wave functions. Here we assume that the z direction is the growth direction ($\boldsymbol{c}$ axis). Since we are interested in quantum confined systems, we will only consider the zone center wave functions obtained including compressive strain and spin-orbit coupling. We will begin with the case of an even biaxial compressive strain, meaning that the magnitude of the strain along the $\boldsymbol{x}$ and $\boldsymbol{y}$ directions is equivalent. Including spin-orbit coupling, it was shown in a previous section that the A and B valence band states can be written as:

$$\begin{aligned}
|A\uparrow\rangle &= \frac{1}{\sqrt{2}}(|P_x\uparrow\rangle + i\,|P_y\uparrow\rangle)\\
|A\downarrow\rangle &= \frac{1}{\sqrt{2}}(|P_x\downarrow\rangle - i\,|P_y\downarrow\rangle)\\
|B\uparrow\rangle &= i\frac{1}{\sqrt{2}}(|P_x\downarrow\rangle + i\,|P_y\downarrow\rangle)\\
|B\downarrow\rangle &= i\frac{1}{\sqrt{2}}(|P_x\uparrow\rangle - i\,|P_y\uparrow\rangle),
\end{aligned} \tag{2.34}$$

The conduction band wave function can be written as $|iS\uparrow\rangle$ and $|iS\downarrow\rangle$. In optical interactions, the C band is usually ignored.

We are interested in finding the non-zero values of the matrix elements $\langle i|\,\boldsymbol{A}\cdot\boldsymbol{p}\,|j\rangle$ where i represents an electron in the conduction band j is the electron in a valence band state, for different electric field polarizations. In the x-y-z basis, this problem boils

down to determining the non-zero matrix elements $\langle S| p_{x,y,z} |A, B\rangle$ for x,y,z polarized light. Clearly x and y polarized light can be coupled to all of the transitions, but not z polarized light. In the case of a transition from an a A valence band state to the conduction band, the direction of the electron spin is preserved, while it is flipped for transitions from the B valence band to the conduction band.

In the case of an uneven biaxial strain, the A and B valence band states were found earlier to be

$$\begin{aligned} |A\uparrow\rangle &= |P_x\uparrow\rangle \\ |A\downarrow\rangle &= |P_x\downarrow\rangle \\ |B\uparrow\rangle &= |P_y\uparrow\rangle \\ |B\downarrow\rangle &= |P_y\downarrow\rangle . \end{aligned} \tag{2.35}$$

In this case, only x polarized light can couple to the A transitions and y polarized light can couple to the B transitions. In most quantum dots, the shape of the dot in the growth plane (perpendicular to the growth direction) is not even along the x and y directions that typically leads to a strain anisotropy. For small amounts of strain anisotropy, the A and B valence band states can be close enough together so that significant PL is observed from both conduction band to A and B transitions. It has been proposed that linearly polarized single photon emission from transitions in an uneven biaxially strained quantum dot can be used in key generation for quantum cryptography applications [67].

2.5 The effects of material disorder on the optical properties of InGaN/GaN heterostructures

In planar InGaN/GaN quantum wells, lattice-mismatch strain effects typically lead to a very large density of threading dislocations ($\sim 10^7 cm^{-2}$) in the InGaN active region, however strong light emission is still observed. In all other light-emitting materials, dislocation densities higher than $10^3 cm^{-2}$ will completely quench the light emission since the excitons will quickly recombine at the dislocation sites [87]. The origin for light emission in InGaN/GaN planar quantum wells has been shown to

be from radiative recombination of electron-hole pairs at localized states formed by material disorder in the InGaN layer [88–90] . For example, Schömig et al. [89] utilized nanoapertures to observe PL from individual localized sites and showed that the luminescence from individual sites had characteristics of quantum dot excitons such as saturation and the presence of biexciton lines.

The physical nature of the material disorder in InGaN layers is somewhat controversial. For years, it was widely accepted that the disorder originated from InN clustering due to the low miscibility of InN in GaN [91]. However, experimental results have shown that InN clusters can be formed as a result of electron beam damage during TEM measurements [87], so earlier experimental findings, primarily using TEM [21, 92], of InN clusters formed during MBE growth are questionable. It was found using low TEM electron beam currents that no gross InN clustering exists in the InGaN layer [87]. One of the most accepted explanations for localized radiative recombination in InGaN layers is the atomistic localization holes (and therefore excitons due to the large exciton binding energy of III-Nitrides) [93]. Theoretically it has been shown that InGaN layers can form In-N-In chains that tend to localize hole states in an otherwise random InGaN crystal [94, 95]. Experimental results by Chichibu et al. [96] have helped to confirm this theory using positron diffusion analysis. In InGaN/GaN heterostructures, it is also possible that interface flucations at the heterostructure interface contribute to the density of disorder states. A general effect of material disorder caused by the localized atomistic fluctuations is the formation of an exponential tail in the density of electronic states below the band edge, also known as an Urbach tail [11, 97]. In InGaN quantum wells (QWs), epilayers or bulk material, linear optical measurements such as photoluminescence excitation (PLE) or photocurrent spectroscopy (PC) are generally dominated by an exponential tail below the bandedge, which validates the presence of disorder in the system [98–100].

2.5.1 Luminescence properties of disorder states in InGaN

Broad PL emission from InGaN QWs has been attributed to radiative recom-

bination of localized energy states within the Urbach tail [89, 101–106]. The first observation to support this argument is that pulsed excitation into the continuum energy levels of the quantum well results in a red-shifting luminescent signal as a function of time [101]. The explanation for this behavior is fast decay of charge carriers from higher energy states in the tail to lower energy states through the emission of phonons [107, 108]. The peak of the PL spectrum further shows an S shape when plotted as a function of temperature. That is, as the temperature of the sample increases, starting at 0 K, the emission wavelength of the disorder states first exhibits a redshift as a function of increasing temperature, followed by a blueshift at higher temperature T_1, then another redshift at a temperature T_2 that is greater than T_1 [104–106]. This behavior can be linked to thermionic processes in which carriers move to more or less localized disorder states (existing at lower and higher energy) based on the amount of thermal energy in the system before recombining [106]. An additional observation to support the radiative recombination of localized states in PL is a continuous blue shift of the peak of the PL emission as a function of excitation intensity [89, 102, 103]. Although some studies have attributed this behavior to screening of internal piezoelectric fields that creates a reverse quantum confined Stark effect, and thus a blue shift of the PL emission, the nanoaperture study of Schomig et al. [89] found that the blue shift is due to a progressive filling of lower energy states as the excitation intensity increased. As the lower energy states become filled, the emission from higher energy states begins to dominate since there are more states at higher energy.

The time-dependent PL of disordered systems is known for a stretched exponential behavior in which the time-dependent luminescence can be fit to a functional form [109]

$$I_{PL}(t) \sim e^{t/\tau^{-\beta}}, \tag{2.36}$$

where β is known as the stretching parameter and typically varies between 0 and 1. The stretching parameter scales inversely with the level of disorder in the system. The stretched exponential decay comes from relaxation processes of excited charge carriers that involves random hopping of electrons and holes between different disorder sites.

The time-dependent probability that an electron and hole will hop to the same site is given by [109, 110]

$$P(t) \sim t^{-(1+\beta)}. \tag{2.37}$$

The recombination rate of carriers is proportional to the number of excited electron-hole pairs N and the probability that they occupy the same site P(t), so that

$$-\frac{dN}{dt} \sim P(t)N. \tag{2.38}$$

Integration of equation 2.38 gives

$$N = e^{const.t^{-\beta}}, \tag{2.39}$$

the same functional form as equation 2.36. This shows that the time-dependent decay of excited electron-hole pairs follows a stretched exponential, a result very different from the single exponential decay observed in 2-level systems interacting with the vacuum field.

2.6 3-D quantum confinement of excitons in InGaN disks in GaN nanowires

The samples studied in this thesis consist of ensembles of InGaN disks grown in GaN nanowires (DINWs) using plasma-assisted molecular beam eptiaxy (PA-MBE) techniques [111–115]. In this section, the general optoelectronic properties of individual DINWs will be introduced. In a later chapter, the optical and structural properties of the ensembles and the unique properties of DINWs grown in the ensembles featured in this thesis will be further examined and discussed.

The active region of the DINW is a thin layer of InGaN that is grown on top of a GaN nanowire base. The radius of the GaN nanowire (30-200 nm) is typically much larger than the exciton Bohr radius in bulk GaN (2.2 nm) [73]. To relieve strain during growth, the InGaN disk does not grow uniformly across the flat top of the GaN nanowire and instead forms a flat pyramid island in the center of the nanowire with the apex of the pyramid slightly extending along the growth direction [9,12,116]. The DINWs featured in this thesis are grown along the c-axis, which results in internal

electric fields within the InGaN layer. Due to strain relaxation at the side wall of the DINW, the magnitude of the internal electric fields is generally much lower than in planar quantum wells, however it is not negligible [12, 117, 118]. Furthermore, the DINWs can be grown virtually free of defects in the active region, therefore emission from excitonic states is possible, unlike in planar quantum wells [119]. More on the growth properties of the DINWs will be discussed in a later chapter.

One of the most interesting aspects of the DINW system is that single photon emission has been observed from the InGaN region using intensity correlation ($g^{(2)}$) measurements of individual DINWs [120]. Single photon emission is usually a characteristic associated with systems that have full 3-D quantum confinement such as quantum dots, where the energy levels are fully quantized and only a single electron-hole pair can exist at a given energy. Typically quantum well materials do not exhibit this property due to the fact that multiple emitting states can exist at approximately the same energy. The lateral dimensions of the InGaN pyramid in the middle of the DINW are typically much larger than the bulk exciton Bohr radius in GaN, therefore it is not immediately clear how full 3-D quantum confinement can be achieved in this system.

One explanation to support 3-D quantum confinement in DINWs involves the lattice pulling effect [121, 122]. In InGaN, regions of lower strain tend to accumulate higher concentrations of InN compared to regions of higher strain. In the InGaN pyramid formed at the center of the GaN nanowire, the strain relief is higher at the apex compared to the base [17, 123]. It has been shown in thick DINWs ($\sim$15 nm thickness) that the InN concentration increases from the base to the apex [9]. Since the apex of the pyramid has a lower effective band gap compared to the base, the pyramid can possibly provide exciton confinement near the apex. Nanocathodoluminescence measurements show that most of the radiative recombination does indeed occur near the apex [9].

Another explanation for 3-D confinement involves the internal electric fields. The radial strain distribution in the DINW makes the internal electric field higher at the center of the DINW compared to the sides. The associated Stark shift creates a lower

energy region in the center of the DINW compared to the side. As a result, the electron and hole wave functions become confined to the center of the DINW. This effect can be futher illustrated using the modeling software TiberCAD. In TiberCAD, the envelope functions of electrons and holes can be solved using finite element methods over a 3-D mesh environment incorporating the effects of strain and the associated internal electric fields. The Coulomb interactions between electrons and holes is ignored. The strain is first solved over the mesh assuming a linear elasticity model [124, 125]. The strain field creates a sheet of charge at the InGaN/GaN interface that is used as a source term for Poisson's equation, along with the sheet charge from the difference spontaneous polarization between the InGaN and GaN layers. Poisson's equation is then solved to find the electric potential that is plugged into Schrödinger's equation, which is used to solve for the electron and hole envelope wave functions incorporating the 8x8 $\boldsymbol{k}\cdot\boldsymbol{p}$ method. The resulting electron and hole density found from Schrödinger's equation is then fed back into Poisson's equation as a source term and the process repeats until the solver converges on a self-consistent solution within some specified tolerance. In the top center of Fig. 2.6, we present the results of the calculation of the internal electric fields resulting from strain. At the bottom center of Fig. 2.6 the lowest energy electron and hole envelope wave functions in a DINW are shown following the self-consistent Schrödinger-Poisson calculation, using a relative tolerance of 10^{-8}. The more red regions represent a higher wave function probability density. The lowest energy electron and hole both appear to be weakly confined to the center of the DINW. The wave functions are also separated along the growth direction of the DINW due to the internal electric fields. Several recent studies have also discussed this effect in blue emitting InGaN DINWs [117, 118, 126]. In general, the electron and hole will be more strongly confined due to the 3-D pyramid shape of the DINW and therefore the wave functions will likely be more concentrated near the center of the DINW. based on the calculation shown in Fig. 2.6, it is is unlikely that the internal electric fields strongly confine the excitons. More accurate modeling of the DINW optoelectronic properties will therefore require the addition of electron-hole Coulomb terms.

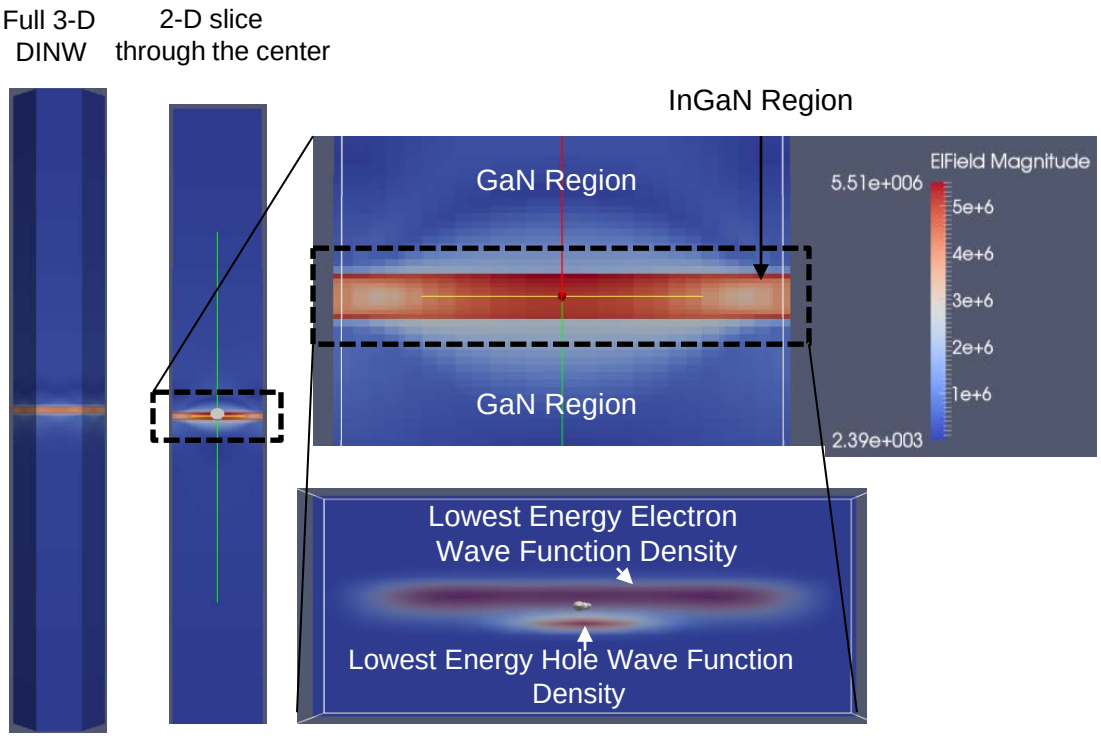

Figure 2.6: The left two figures show the overall DINW. The InGaN region is 3 nm thick and the overall nanowire is 80 nm long. The diameter of the nanowire is 30 nm. The left-most figure shows the 3-D nanowire while the second from the left shows a slice through the center of the DINW. The center figure shows a zoom-in of the slice and the magnitude of the internal electric fields. Note that the field is highest in the center of the DINW. The bottom-center figure shows the electron and hole wave functions, where the more red color represents a higher wave function density.

2.6.1 Luminescence properties of InGaN disks in GaN nanowires

The PL of individual DINWs shows several interesting properties. As mentioned in the previous section, some DINWs exhibit properties of single photon emission in intensity correlation measurements, a characteristic trait of a two-level quantum dot system. For a more conventional single quantum dot system such as a III-As quantum

dot, the time-resolved PL is normally an exponentially decreasing function of time with a decay constant that is proportional to the spontaneous emission lifetime [127]. Instead of a single exponential decay, the time-resolved PL of individual DINWs must usually be fit to a stretched exponential model [12, 120]. This shows that disorder plays a large role in the optical dynamics of the system, even though ultimately the emission appears to come from a single quantum dot exciton. Another interesting aspect of individual DINW luminescence is the discrepancy between the decay rate extracted from time resolved PL measurements and the line width measured from frequency resolved PL measurements, which is typically $\sim$ 1000 times larger than what is expected from the inverse of the spontaneous emission time. One possible explanation for this effect is fast spectral diffusion, possibly caused by background charge fluctuations. This effect will be explored further later on.

2.7 Chapter summary This chapter presented some of the basic elements of semiconductor band theory and mentioned some of the methods of obtaining an approximate solution to the semiconductor band structure of wurtzite materials. The concept of the effective mass allows us to calculate the envelope wave functions of electrons and hole in quantum confined structures. This was used to demonstrate the effects of internal electric fields in wurtzite InGaN/GaN heterostructures. The optoelectronic properties of the individual InGaN/GaN DINWs featured in this thesis were also laid out. It was found that the internal electric fields in DINWs can weakly confine electrons and holes to the center of the DINW, providing a source of quasi-3D confinement in addition to other effects such as the lattice pulling effect.

CHAPTER 3

Theoretical background of coherent nonlinear spectroscopy of quantum dots

As stated earlier, the work in this thesis is aimed towards future applications involving coherent control of solid state systems, such as quantum computation. Prior to the reliable execution of demonstrations involving coherent optical control, a new system must be characterized fully. Because coherent optical control is a nonlinear optical process, the coherent nonlinear optical spectrum is naturally required to characterize the system. This is perhaps best exemplified in earlier work in our group, where the coherent nonlinear absorption spectrum of GaAs interface-fluctuation quantum dots [128] laid the groundwork for coherent optical control experiments shortly afterward [48, 49]. The coherent nonlinear optical spectrum allows us to measure intrinsic decay rates in the system that may not be possible to measure in the linear absorption spectrum, such as the degree of inhomogeneous broadening and the dipole dephasing rates. Furthermore, the coherent nonlinear optical spectrum allows us to comment on the role of many-body physics in the system, which has been an important roadblock in the implementation of quantum wells and bulk excitons in coherent control applications [129]. In this chapter, some theoretical techniques based on the density matrix equations of motion will be considered in order to gain an initial understanding of the complex lineshapes that can be involved in the coherent nonlinear spectrum.

The nonlinear dynamics of solid state systems due to interactions with strong laser fields is generally difficult to model theoretically. In some cases, the frequency-domain

nonlinear absorption line shapes of strong laser fields that interact with solid state systems can reveal important physical phenomenon that can later be understood in terms of a more complicated physical model. A good example of this can be found in nonlinear optical studies of excitons in bulk GaAs that was dominated to third order by excitation-induced dephasing [130]. A theoretical understanding of this phenomenon required complex modeling based on the semiconductor Bloch equations [131] that incorporated the many-body effects of exciting multiple excitons in the system.

Unlike in bulk solid state material, the theoretical analysis of laser field interactions in semiconductor quantum dots simplifies considerably, essentially owing to the fact that only one electron-hole pair (or charged variants such as two electrons and one hole) can be excited to a given energy level due to Coulomb effects. Because of this, the nonlinear interactions between laser fields and quantum dots can be mapped to the interactions between laser fields and atomic systems [48, 128]. As mentioned earlier, this also allows for the use of quantum dots in optically addressed coherent control applications that are not feasible using bulk material because of the complex nonlinear optical response.

The work in this thesis centers around an understanding of the nonlinear optical properties of ensembles of InGaN disks in GaN nanowires (DINWs). As we have seen in a previous chapter, a weakly confined quantum dot can exist at the center of the DINW. Although it is possible that the nonlinear optical properties of the DINW have some influence from many-body physics, as a starting point to our analysis we will consider that the coherent nonlinear optical response of the DINW ensemble can be understood in terms of the nonlinear optical response of an ensemble of atomic systems. The justification for this starting point largely stems from previous results that demonstrated single photon emission in g^2 measurements of single DINWs. Typically single photon emission is associated with atom-like systems. Ultimately, a comparison of the theoretical analysis in this chapter to the nonlinear optical data will be required to rule out complex many-body behavior.

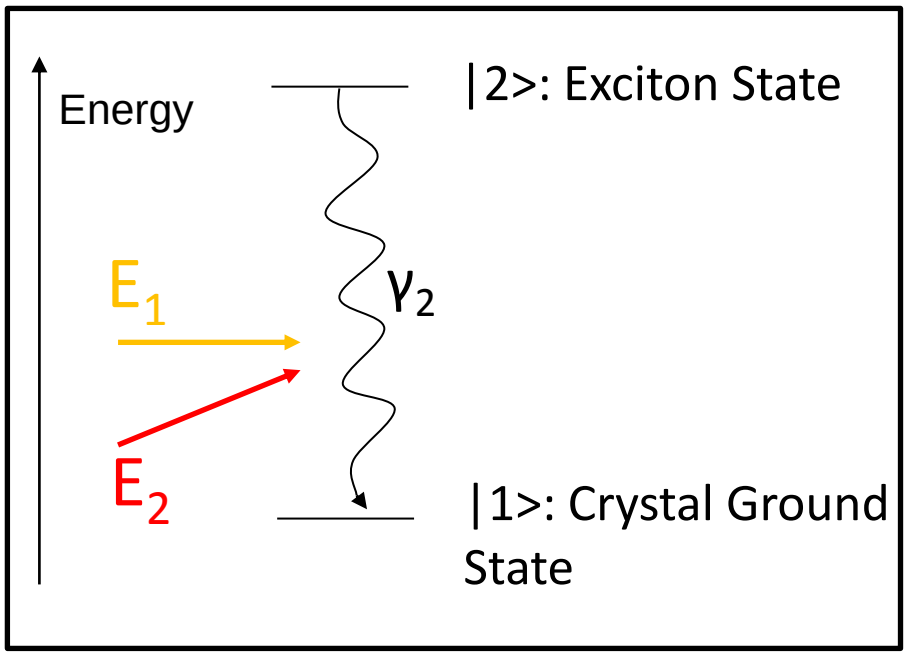

Figure 3.1: Energy diagram of quantum dot exciton system interacting with laser fields

In an energy level picture, the initial diagram of a single DINW is shown in Fig. 3.1. We consider the situation in which two laser fields E_1 and E_2 optically excite the system resulting in a nonlinear polarization. The discrete excited state represents the creation of an exciton (or charged variants such as trions or biexcitons) depending on the energy of the two laser fields and the ground state is the crystal ground state. In this chapter we mainly consider a closed two-level system although in later chapters we will find that this assumption must be modified by the addition of more energy levels for accurate modeling.

3.1 Optical interactions in two-level systems

The time-dependent state vector $|\psi\rangle$ of the two-level system is generally described as a superposition of the ground state $|1\rangle$ and the excited state $|2\rangle$:

$$|\psi\rangle(t) = a_1(t)|1\rangle + a_2(t)|2\rangle . \tag{3.1}$$

I will now take the frequency separation between $|1\rangle$ and $|2\rangle$ to be ω_0. In the dipole approximation we can write the interaction between a two-level system and a laser field as

$$\boldsymbol{V} = -\boldsymbol{\mu} \cdot \boldsymbol{E}, \tag{3.2}$$

where the $\boldsymbol{V}$ operator can be written as the 2x2 matrix

$$-E \begin{pmatrix} 0 & \mu_{12} \\ \mu_{21} & 0 \end{pmatrix}. \tag{3.3}$$

This form is often more convenient then the $\boldsymbol{A} \cdot \boldsymbol{p}$ form used in a previous chapter. Schrödinger's equation, describing the dynamics of the two-level system, is given by

$$i\hbar\dot{\vec{a}} = \mathbf{H}\vec{a}, \tag{3.4}$$

where $\boldsymbol{H} = \boldsymbol{H_0} + \boldsymbol{V}$ with $\boldsymbol{H_0}$ describing the energy of the quantum dot exciton state, given in matrix form by

$$\frac{\hbar}{2} \begin{pmatrix} -\omega_0 & 0 \\ 0 & \omega_0 \end{pmatrix}, \tag{3.5}$$

and $\vec{a}$ is the 1x2 vector formed by the two time-dependent probability amplitudes.

Instead of proceeding forward with solving the time-dependent Schrödinger's equation as written in the amplitude approach, it is often instead useful to introduce the density matrix equations of motion to solve for the system dynamics [132]. One of the most important reasons for utilizing the density matrix approach over the amplitude approach is that it is much simpler to account for interactions that affect the relative phases of the ground and excited states, but do not cause population decay. This type of interaction is known to cause pure dephasing, a decay term that affects only the off-diagonal density matrix elements and observables such as polarization. Minimizing pure dephasing in real quantum systems is a necessary goal before the systems can be used in applications such as quantum information processing that require the preservation of a well-defined time-dependent phase between different quantum

states. The density matrix is defined as:

$$\boldsymbol{\rho} = \sum_j w_j \left|\psi_j\right\rangle \left\langle\psi_j\right|, \tag{3.6}$$

where w_j is the probability of being in a pure state $|\psi_j\rangle$. The density matrix equation of motion, following from Schrödinger's equation is then given by

$$i\hbar\frac{d\boldsymbol{\rho}}{dt} = [\boldsymbol{H}, \boldsymbol{\rho}]. \tag{3.7}$$

For a closed, homogeneously broadened two-level system, the density matrix equations of motion with an external perturbation $\boldsymbol{V}$ from equation 3.2 are explicitly given by

$$\begin{aligned} i\hbar\dot{\rho}_{11} &= V_{12}\rho_{21} - c.c. + \gamma_2\rho_{22} \\ i\hbar\dot{\rho}_{22} &= V_{21}\rho_{12} - c.c. - \gamma_2\rho_{22} \\ i\hbar\dot{\rho}_{12} &= -\hbar\omega_0\rho_{12} + V_{12}(\rho_{22} - \rho_{11}) - \gamma\rho_{12} \\ \rho_{21} &= \rho_{12}^*, \end{aligned} \tag{3.8}$$

where γ_2 is the excited state decay rate due to spontaneous emission and $\gamma = \gamma_2/2 + \Gamma$, where Γ is the pure dephasing rate, which will be discussed further shortly.

We will now consider a specific case of a single monochromatic traveling wave laser field interacting with the two-level system. If we assume that the optical field is polarized in the $\hat{\boldsymbol{x}}$ direction and propagating in the $\hat{\boldsymbol{z}}$ direction, we can write the total field as

$$\boldsymbol{E}(Z,t) = \frac{1}{2}\hat{\boldsymbol{x}}[\tilde{E_0}(Z,t)e^{i(kZ-\omega t)} + \tilde{E_0^*}(Z,t)e^{-i(kZ-\omega t)}]. \tag{3.9}$$

Before solving equation 3.8, it is often useful to move to the field interaction representation, in which $\boldsymbol{\rho}$ is redefined so that

$$\tilde{\boldsymbol{\rho}} = e^{-i\frac{\omega t}{2}\boldsymbol{\sigma_z}}\boldsymbol{\rho}e^{i\frac{\omega t}{2}\boldsymbol{\sigma_z}}. \tag{3.10}$$

After plugging in the interaction term in equation 3.2, the steady-state solution of equation 3.8 in the field interaction representation is given by

$$\begin{aligned} \tilde{\rho_{12}} &= \frac{i\boldsymbol{\mu}_{12}\cdot\boldsymbol{\epsilon}E_0(Z,t)}{2\hbar(\gamma - i\delta)}\frac{\gamma^2+\delta^2}{\gamma^2+\delta^2+\frac{4\gamma}{\gamma_2}|\frac{\boldsymbol{\mu}_{21}\cdot\boldsymbol{\epsilon}E_0(Z,t)}{2\hbar}|^2} \\ \tilde{\rho_{21}} &= \tilde{\rho_{12}}^* \\ \rho_{22} &= \frac{|\frac{2\gamma}{\gamma_2}\frac{\boldsymbol{\mu}_{21}\cdot\boldsymbol{\epsilon}E_0(Z,t)}{2\hbar}|^2}{\gamma^2+\delta^2+\frac{4\gamma}{\gamma_2}|\frac{\boldsymbol{\mu}_{21}\cdot\boldsymbol{\epsilon}E_0(Z,t)}{2\hbar}|^2}\rho_{11} = 1 - \rho_{22}. \end{aligned} \tag{3.11}$$

where $\hat{\boldsymbol{\epsilon}}$ is the polarization direction of the applied field. In the next section, we will see how the electric field intensity dependence of the off-diagonal density matrix terms in equation 3.11 are what give rise to the nonlinear optical absorption in two-level systems.

3.1.1 Maxwell-Bloch equations

So far, our theoretical analysis has been focused on calculating quantum mechanical properties of two level systems excited by laser fields. In our experiments, we do not directly measure the state of the two level system. Instead the state of the two level system (or an ensemble of two level systems) is inferred based on nonlinear signals emitted by the two level system. The nonlinear signals are generated from an induced polarization in the two level system created by one or more excitation beams. Methods for nonlinear signal detection will be discussed in a later chapter.

Laser fields can generate a dipole moment in the individual quantum dot excitons (or two-level systems) that we study. The expectation value of the microscopic dipole moment is given by

$$< \boldsymbol{\mu}(t) >= \boldsymbol{\mu}_{21}\rho_{12}(t) + \boldsymbol{\mu}_{12}\rho_{21}(t). \tag{3.12}$$

This follows from the fact that the expectation value of an operator $\boldsymbol{O}$ is given by $\mathrm{Tr}[\boldsymbol{\rho O}]$. In an ensemble of two-level systems, the individual dipole moments add up to give a macroscopic polarization

$$< P(t) >= N[\boldsymbol{\mu}_{21}\rho_{12}(t) + \boldsymbol{\mu}_{12}\rho_{21}(t)]. \tag{3.13}$$

For many materials, the polarization can be written in terms of an applied classical electric field as the power series expansion

$$< P(t) >= \epsilon_0(\chi^{(1)}E(t) + \chi^{(2)}E(t)^2 + \chi^{(3)}E(t)^3 + ...). \tag{3.14}$$

From equations 3.13 and 3.14, one can see that the nonlinear susceptibility of ensembles of two level systems can be related to the internal state of the constituent two-level systems. I will give an example shortly of how this is done for the third order nonlinear term. Although in this work we are primarily interested in the $\chi^{(3)}$

response,in many materials the $\chi^{(2)}$ term is also interesting to study, since it leads to processes such as difference and sum frequency generation, converting a higher (lower) energy electric field into a lower (higher) energy electric field [133, 134]. Most of the time, higher order terms such as $\chi^{(4)}$ and $\chi^{(5)}$ are not considered individually since they are complicated to model, difficult to observe, and in many cases give no new information about the system.

The nonlinear polarization induced by the external electric fields can be fed in to Maxwell's equations as a source term, thus generating new fields. In this case we will use Maxwell's equations since the analysis in this thesis is semi-classical: treating the electric field classically and the dynamics of the atom quantum mechanically. The interference of the newly generated electric fields provided by the polarization induced in the sample and the excitation field can create an overall phase shift or decrease in intensity of the transmitted field compared to the excitation field. The following derivation of the Maxwell-Bloch equation heavily utilized ref. [30].

A well-known result of combining different components of Maxwell's equations is the wave equation for transverse electromagnetic fields. In this case, we assume that the transverse field is a plane wave propagating along the z direction, polarized in the x-y plane. This gives the wave equation:

$$\frac{\partial^2 \boldsymbol{E}(Z,t)}{\partial z^2} - \frac{1}{c^2}\frac{\partial^2 \boldsymbol{E}(Z,t)}{\partial t^2} = \frac{1}{c^2\epsilon_0}\frac{\partial^2 \boldsymbol{P}(Z,t)}{\partial t^2} \tag{3.15}$$

The idea is to now substitute the polarization given by equation 3.13 into the wave equation to see the effect of the polarization source term on the electric field. In order to simplify the resulting expression, we will utilize the slowly varying amplitude and phase approximation (SVAPA). Additionally, we only consider the positive frequency components of the laser field and polarization: $\boldsymbol{E}^{+}(\mathrm{Z,\ t}) = \frac{1}{2}\hat{\boldsymbol{\epsilon}}\tilde{E}(\mathrm{Z,t})e^{i(kZ-\omega t+\phi(Z,t))}$ and $\boldsymbol{P}^{+}(\mathrm{Z,\ t}) = \frac{1}{2}\hat{\boldsymbol{\epsilon}}\tilde{P}(\mathrm{Z,t})e^{i(kZ-\omega t+\phi(Z,t))}$, where $\hat{\boldsymbol{\epsilon}}$ is the polarization vector, with an understanding that the full solution requires the addition of the complex conjugate. To make the SVAPA we then assume that the complex amplitude $\tilde{E}(\mathrm{Z,t})$ is slowly varying in space compared to the laser wavelength and time compared with ω^{-1}. It is also convenient to rewrite the positive frequency polarization in terms of its real

and imaginary components $\tilde{P}$(Z,t)

$$\hat{\boldsymbol{\epsilon}}\tilde{P}(Z,t) = N\boldsymbol{\mu}_{12}\tilde{\rho}_{21}(Z,t) = N\boldsymbol{\mu}_{12}[u(Z,t) - iv(Z,t)]/2. \tag{3.16}$$

The SVAPA also requires that the polarization is slowly varying in space compared to the laser wavelength and time compared with ω^{-1}. The real parts of equation 3.16 lead to phase shifts in the transmitted electric field, while the imaginary parts give changes in field amplitude. Although it is sometimes interesting to measure the change in phase caused by a nonlinear medium, especially for applications such as electro-optic modulation [135], in this study we are interested in extracting information about the quantum dot exciton system through measurements of the frequency dependence of the intensity (amplitude) changes to the electric field caused by the imaginary components of the induced polarization. Because of the slow variations in the polarization and electric field, we neglect terms in equation 3.15 that have second derivatives in time or space. Finally, since we are interested in a steady-state (due to the continuous-wave fields) solution, we set any first derivatives in time equal to zero. This gives the resulting equation for the electric field amplitude in terms of the imaginary polarization component:

$$[k + \frac{\partial\phi(Z)}{\partial Z}]\frac{\boldsymbol{\epsilon}\partial\tilde{E}(Z,t)}{\partial Z} = \frac{Nk^2\boldsymbol{\mu_{12}}}{2\epsilon_0}v(Z,t). \tag{3.17}$$

The phase ϕ(Z) is used to account for situations in which the index of refraction of the material differs considerably from unity [30].

The essential idea now is to solve for v(Z,t), the imaginary component of the off-diagonal density matrix element ρ_{21}, assuming the other physical quantities such as the dipole moment matrix element μ_{12} and wave vector magnitude $|\boldsymbol{k}|$ are known. The imaginary component of ρ_{21} from equation 3.11 is given by

$$Im[\tilde{\rho_{21}}(Z,t)] = \frac{\boldsymbol{\mu}_{21}\cdot\boldsymbol{\epsilon}\gamma E_0(Z,t)}{2\hbar(\gamma^2+\delta^2)}\frac{\gamma^2+\delta^2}{\gamma^2+\delta^2+\frac{4\gamma}{\gamma_2}|\frac{\boldsymbol{\mu}_{21}\cdot\boldsymbol{\epsilon}E_0(Z,t)}{2\hbar}|^2}, \tag{3.18}$$

where E_0 is the applied electric field. Keeping the first two terms of the power series expansion of the expression in equation 3.18 in terms of the electric field gives

$$Im[\tilde{\rho_{21}}(t)] \approx \frac{\boldsymbol{\mu}_{21} \cdot \boldsymbol{\epsilon} \gamma E_0(Z,t)}{2\hbar(\gamma^2+\delta^2)}(1 - |\frac{\boldsymbol{\mu}_{21} \cdot \boldsymbol{\epsilon} E_0(Z,t)}{2\hbar}|^2 \frac{1}{\gamma^2+\delta^2}) \tag{3.19}$$

The electric field dependence of the second term on the right hand side of equation 3.19 shows how the third order component of the nonlinear susceptibility ($\chi^{(3)}$ in equation 3.14 can be related to the off-diagonal density matrix element after plugging in equation 3.19 to equation 3.16.

In the remaining sections, we will focus on semiclassical calculations of the imaginary components of the density matrix elements of interest for different physical situations. Specifically we are interested in calculating steady-state values of off-diagonal density matrix elements to third order in the applied fields. Although it will not be explicitly shown in the calculations, the observable of interest in our experiments is the polarization induced in the sample. We are mainly interested in understanding the qualitative frequency dependence of the third order response since the line shapes can be used to comment on fundamental decay parameters of the material.

3.2 Steady-state solution for a two-level system interacting with two laser fields in the pump-probe geometry

In this section, we will begin to explore the optical physics associated with the third order susceptibility. In general, we are interested in applying two lasers to the sample with different frequencies, resulting in the generation of a nonlinear polarization. This type of interaction is also known more generally as four-wave mixing [136]. When two lasers with different frequencies are applied to the same quantum dot exciton transition, the nonlinear interaction between the lasers produces very interesting spectral features that reveal system dynamics not otherwise observable with single laser experiments. In this section, a theoretical understanding of the nonlinear interaction between two laser fields and a two-level quantum system will be explored, assuming continuous-wave excitation fields. We will first consider a simple homogeneously broadened two-level system in the absence of dipole dephasing, then later on add dephasing and inhomogeneous broadening.

3.2.1 Homogeneously broadened two-level system

We are interested in solving the density matrix equations of motion for two applied laser fields with optical frequencies ω_1 and ω_2. The electric field component in the interaction term (equation 3.2) should therefore be replaced by a sum over the two fields with the corresponding frequencies. To simplify the analysis, it is useful to move the problem into an interaction representation. The interaction representation is defined so that

$$\boldsymbol{\rho}^{(I)} = e^{i\boldsymbol{H}_0 t/\hbar}\boldsymbol{\rho}e^{-i\boldsymbol{H}_0 t/\hbar}. \tag{3.20}$$

In this case, the density matrix equations of motion are transformed, resulting in the following set of equations:

$$\begin{aligned}
\dot{\rho}_{11} &= -\textstyle\sum_{\mu=1,2}[i\chi_\mu^*\rho_{21}^I + i\chi_\mu\rho_{12}^I] + \gamma_2\rho_{22} \\
\dot{\rho}_{22} &= \textstyle\sum_{\mu=1,2}[i\chi_\mu^*\rho_{21}^I - i\chi_\mu\rho_{12}^I] - \gamma_2\rho_{22} \\
\dot{\rho}_{12}^I &= \dot{\rho}_{21}^{I*} = -\textstyle\sum_{\mu=1,2} i\chi_\mu^*\,[2\rho_{22} - 1] - \gamma\rho_{12}^I,
\end{aligned} \tag{3.21}$$

where χ_μ = -$(\hat{\boldsymbol{\mu}})_{21} \cdot \hat{\boldsymbol{\epsilon}_{\boldsymbol{\mu}}} E_\mu(Z,t)/2\hbar$. We seek a steady-state solution to equation 3.21 by setting the time derivatives on the left hand side equal to zero. However even with this simplification, there is still no exact steady-state solution to equation 3.21. We therefore proceed by obtaining an approximate solution to equation 3.21 using time-dependent perturbation theory with the atom-field interaction as the perturbation. The analysis in this section can also be found in ref. [30].

We begin the problem under the assumption that the system starts in the ground state so that the zeroeth order solution (no applied field) is $\rho_{11}^{(0)} = 1$ with all other zeroeth order density matrix elements = 0. Plugging in the zeroeth order solution to equation 3.21 gives the first order off-diagonal density matrix term:

$$\rho_{21}^{I(1)}(\boldsymbol{R},t) = -\sum_{\mu=1,2} i\chi_\mu e^{i(\boldsymbol{k_\mu}\cdot\boldsymbol{R}+\delta_\mu t)}\frac{1}{(\gamma + i\delta_\mu)}. \tag{3.22}$$

where $\delta_\mu = \omega_0$ - ω_μ. Substituting the first order density matrix equation back into the equations of motion results in the second order population term:

$$\rho_{22}^{I(2)}(\boldsymbol{R},t) = \sum_{\mu,\nu=1,2} \chi_\mu \chi_\nu^* e^{-i(\omega_\mu - \omega_\nu)t} \frac{1}{(\gamma + i\delta_\mu)(\gamma - i\delta_\nu)} [1 + \frac{2\Gamma}{(\gamma_2 - i(\omega_\nu - \omega_\mu)}]. \quad (3.23)$$

Finally, the third order term is given by:

$$\begin{aligned} &\rho_{21}^{I(3)}(\boldsymbol{R},t) = 2i \textstyle\sum_{\mu,\nu,\sigma=1,2} \chi_\mu \chi_\nu^* \chi_\sigma e^{i(\boldsymbol{k_s}\cdot\boldsymbol{R} + \delta_s t} \\ &\times \tfrac{1}{(\gamma+i\delta_s)(\gamma+i\delta_\mu)(\gamma-i\delta_{nu})} [1 + \tfrac{2\Gamma}{\gamma_2 - i(\omega_\nu - \omega_\mu)}], \end{aligned} \quad (3.24)$$

where $\delta_s = \delta_\mu$ - δ_ν + δ_σ and $\boldsymbol{k_s} = \boldsymbol{k_\mu}$ - $\boldsymbol{k_\nu}$ + $\boldsymbol{k_\sigma}$.

For interactions involving two beams (labeled ω_1 and ω_2), equation 3.24 gives a total of 8 terms each of which produces a steady-state polarization in the sample that acts as a source term in the Maxwell-Bloch equations. In this thesis, we are interested in measuring nonlinear terms that are emitted along the ω_2 beam direction ($\boldsymbol{k_s} = \boldsymbol{k_2}$). To isolate these terms, the ω_1 and ω_2 beams are often crossed at the sample and both the nonlinear signal and ω_2 beam are homodyne detected, as shown in Fig. 3.2. This is often known as the pump-probe geometry, hence the title of this section. Methods for phase-sensitive detection of the nonlinear signal will be discussed further in a later chapter.

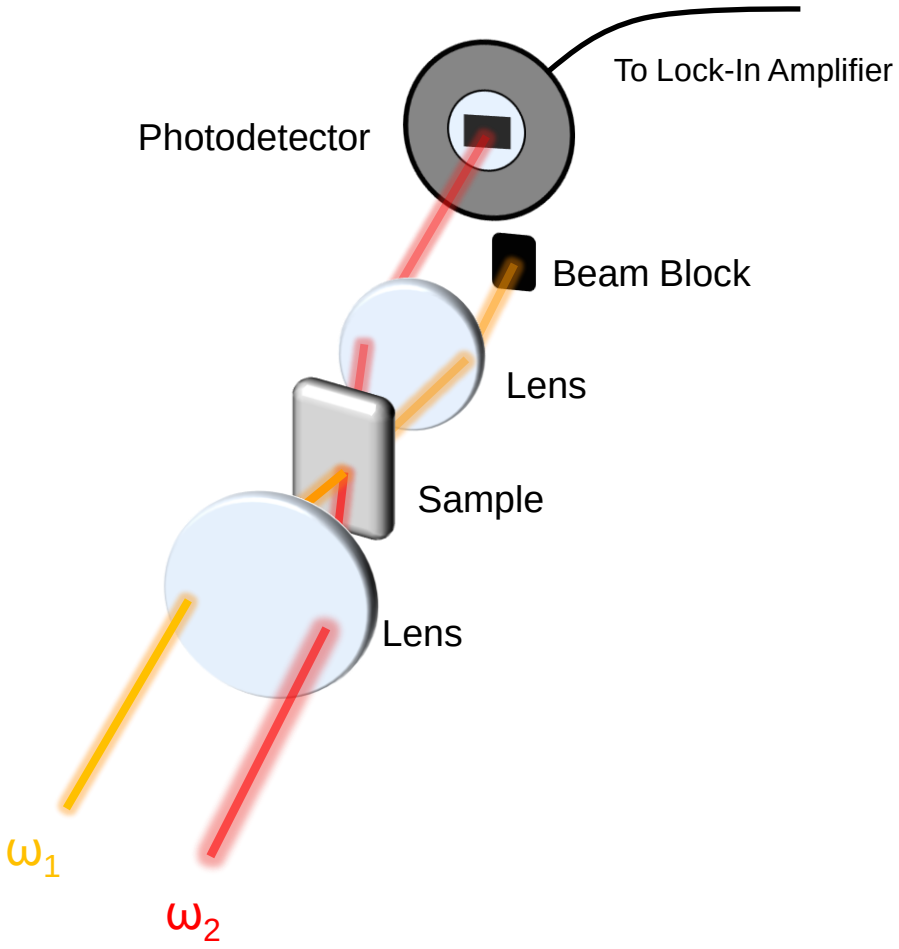

Figure 3.2: Pump-probe beam geometry and nonlinear signal detection technique.

By detecting only nonlinear signals emitted along the ω_2 direction, the number of terms in equation 3.24 that contribute to the nonlinear signal goes from 8 to 2. The resulting nonlinear off-diagonal density matrix element is given by

$$\begin{aligned}\rho_{21}^{I(3)}(\boldsymbol{R},t) &= 2i\chi_2|\chi_1|^2 e^{i(\boldsymbol{k_2}\cdot\boldsymbol{R}+\delta_2 t)} \\ &\times\left(\frac{1}{(\gamma+i\delta_2)^2(\gamma-i\delta_1)}\left[1+\frac{2\Gamma}{\gamma_2-i(\omega_2-\omega_1)}\right]+\frac{1}{(\gamma+i\delta_2)(\gamma^2+\delta_1^2)}\left[1+\frac{2\Gamma}{\gamma_2}\right]\right).\end{aligned} \tag{3.25}$$

The right hand side of equation 3.25 contains two resonances corresponding to the two terms that contribute to the nonlinear signal. The first term on the right hand side is known as the coherent population pulsation term (PPT) and the second term is known as the saturation term (ST). It should be appreciated that the theory of

pump-probe spectroscopy (or often referred to as saturation spectroscopy) extending beyond third order and including systems such as open two-level systems is the subject of many publications [137–140] that have been required to understand the complex topic of atom-field interactions.

The physics of the PPT is related to interference effects between the ω_1 and ω_2 beams in second order, when ω_2 acts in first order and ω_1 acts in second order. This interaction leads to a second order population that oscillates in time at frequency ω_1 - ω_2. Because of the time-dependent phase, the PPT depends on the coherent properties of the excitation fields. The population is also spatially modulated by the phase term $(\boldsymbol{k_2} - \boldsymbol{k_1}) \cdot \boldsymbol{R}$. In third order, the pump photon is scattered off of the spatial population grating in the direction of the probe beam. The spacing of the population grating is given by $\frac{\lambda}{2Cos(\frac{\theta}{2})}$ [141]. In the absence of spatial energy diffusion of the system, a population pulsation resonance will be observed in the third order lineshapes as long as the difference frequency between ω_1 and ω_2 is less than the decay rate of the population γ_2. If spatial diffusion of the system also exists, for example in atomic vapors, then the population pulsation resonance may be observed only if the decay rate γ_2 is greater than the spatial diffusion rate $(\boldsymbol{k_2} - \boldsymbol{k_1}) \cdot \boldsymbol{v}$, where $\boldsymbol{v}$ is the velocity of the system.

In the ST term, the ω_1 field acts in first and second order, generating a population in the excited state that does not depend on the coherent properties of the field. The creation of an excited state population saturates or bleaches the absorption of the ω_2 field. As we will see later on, this term always results in a bleaching or positive differential transmission signal. On the other hand, the PPT term can result in an induced absorption of the ω_2 beam caused by the presence of the ω_1 beam. The perturbation sequences leading to the PPT and ST terms is illustrated in Fig. 3.3.

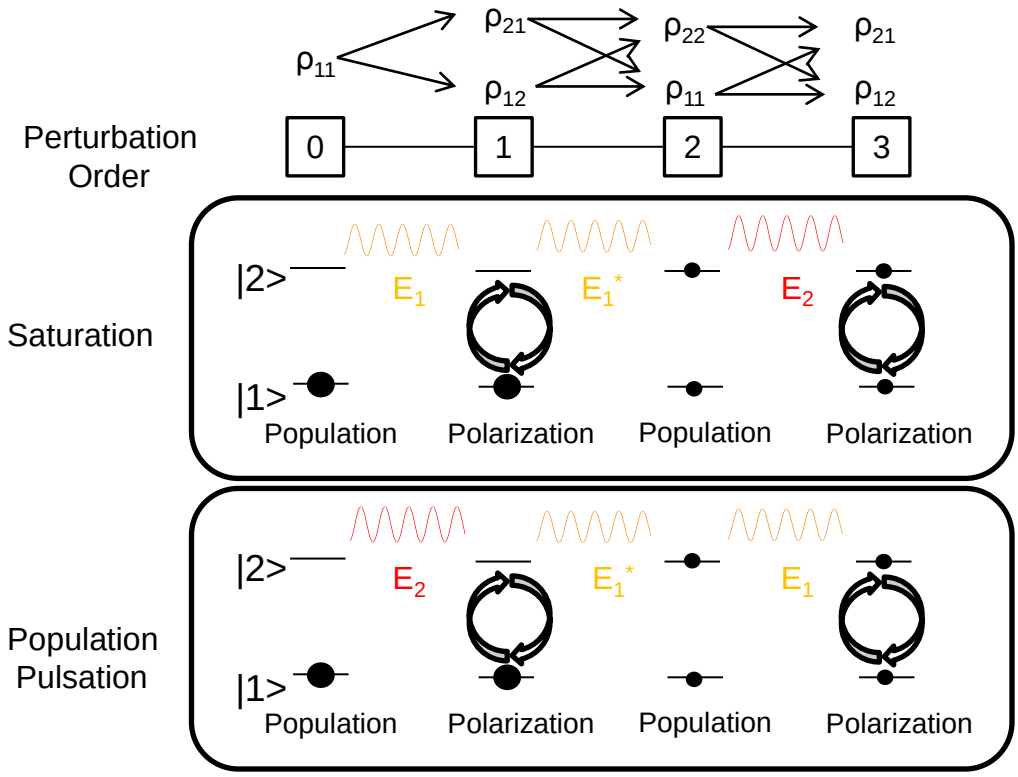

Figure 3.3: Schematic showing the contribution of the fields E_1 and E_2 at different perturbation orders. The nonzero contributions to the steady-state density matrix at each perturbation order is shown at the top of the figure.

In the situation where $\omega_1 = \omega_2$, the resulting third order matrix element is given by

$$\begin{aligned}\rho_{21}^{I(3)}(\boldsymbol{R}, t) &= 4i\chi_2|\chi_1|^2 e^{i(\boldsymbol{k_2}\cdot\boldsymbol{R}+\delta t)} \\ &\times \frac{1}{(\gamma+i\delta)}\frac{1}{(\gamma^2+\delta^2)}[1+\frac{2\Gamma}{\gamma_2}],\end{aligned} \tag{3.26}$$

where $\delta = \delta_1 = \delta_2$ in this case. Effectively the degenerate nonlinear optical response gives the same information as the linear optical response in this situation, except that the Lorentzian line shape in linear absorption is replaced by a Lorentzian squared.

Generally to see new physics beyond what is observed in linear absorption, we must measure the nonlinear spectrum with ω_1 fixed near resonance and ω_2 tuned with respect to the fixed ω_1. This will be especially clear when the nonlinear response of inhomogeneously broadened two-level systems is presented.

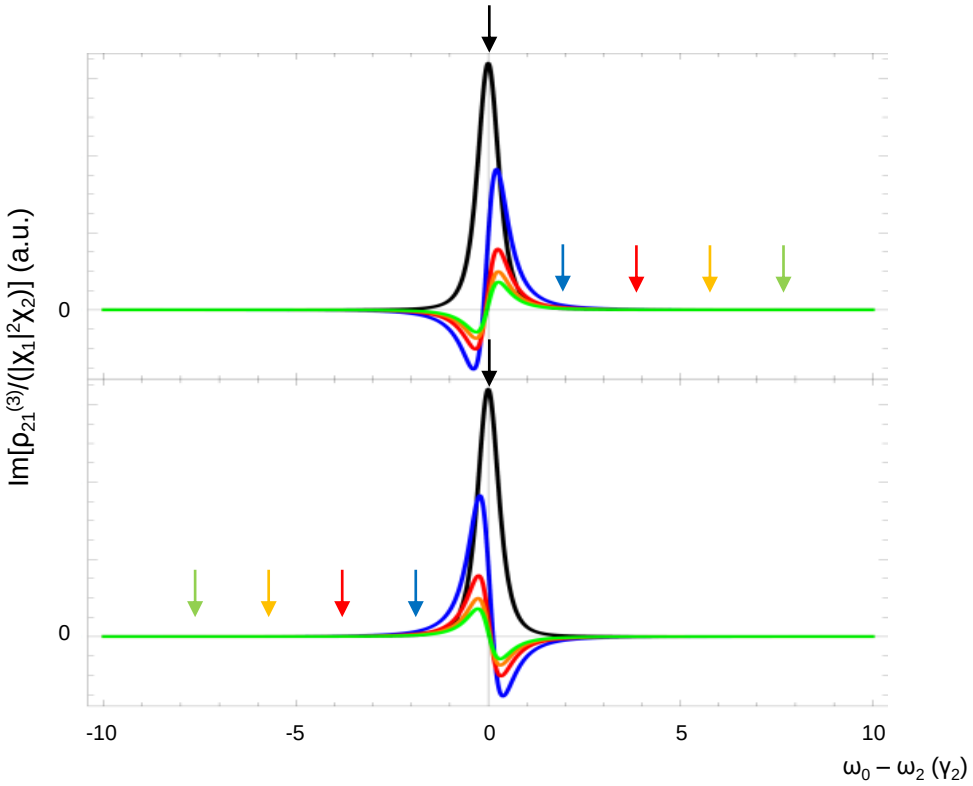

Figure 3.4: Imaginary component of the third order off-diagonal density matrix element for a homogeneously broadened system with no pure dephasing. The ω_1 frequency is given by the colored arrow, and the resulting third-order response as a function of ω_2 is given by the spectrum with the corresponding color..

3.2.1.1 Lineshapes with no pure dephasing for closed two-level system

In Fig. 3.4 the nonlinear optical response given by equation 3.25 is shown for several different values of ω_1 given by the colored arrows with $\Gamma = 0$. When ω_1 is tuned near line center, the nonlinear response shows a single peak, similar to the linear absorption spectrum. However, as ω_1 is tuned away from line center, the nonlinear response shows an interference-type line shape due to the PPT. The interference line

shapes observed in Fig. 3.4 have been reported in the coherent nonlinear optical spectrum of single GaAs quantum dots at low temperature [48, 128].

3.2.2 The effects of pure dephasing

Pure dephasing, or decay of the phase relationship between different energy levels without population decay, can come from random, time-dependent jumps in the transition frequency, assuming that the magnitude of the jumps is much lower than the transition frequency and that the time-duration of the jump is much faster than the fastest population decay in the system. In a solid state system, the time-dependent jumps can occur from interactions between the quantum dot exciton and the solid state environment. A typical example of a pure dephasing process would involve a transient interation between an exciton and a background charge state, where the time duration of the interaction is less than the exciton population decay rate. Note that this interaction returns the transition frequency back to its unperturbed value after the interaction time. We also assume that the frequency jumps are Markovian, so that a frequency jump at a time t_1 does not depend on a previous jump at a time t_2.

To see why random variations in the transition frequency $\Delta\omega(t)$ can cause pure dephasing (following Ref. [142]), we first write the equation of motion for the off-diagonal density matrix element with no applied electric field,

$$i\hbar\dot{\rho}_{12} = -\hbar(\omega_0 + \Delta\omega(t))\rho_{12} - \frac{\gamma_2}{2}\rho_{12}. \tag{3.27}$$

Integration of equation 3.27 gives

$$\rho_{12}(t) = \rho_{12}(0)e^{(i\omega_0 - \frac{\gamma_2}{2})t + i\int_0^t \Delta\omega(t')dt'}. \tag{3.28}$$

We now take a time average of both sides of equation 3.28. On the right hand side we get the term

$$< e^{i\int_0^t \Delta\omega(t')dt'} >=< 1+i\int_0^t dt_1\Delta\omega(t_1) - \frac{1}{2}\int_0^t\int_0^{t_1} dt_1dt_2\Delta\omega(t_1)\Delta\omega(t_2)+... > . \tag{3.29}$$

We take the time average inside each integral. The first term in equation 3.29 gives

$$i\int_0^t dt_1 < \Delta\omega(t_1) >= C, \tag{3.30}$$

where C is a constant, utilizing the fact that $< \Delta\omega(t_1) > = 0$. The second term in the expansion inside equation 3.29 gives

$$-\frac{1}{2}\int_0^t \int_0^{t_1} dt_1 dt_2 < \Delta\omega(t_1)\Delta\omega(t_2) >= -\frac{1}{2}\int_0^t \int_0^{t_1} dt_1 dt_2 2\Gamma\delta(t_1 - t_2) = -\Gamma t, \quad (3.31)$$

where Γ is the pure dephasing rate and the Markoff approximation has been used to equate $< \Delta\omega(t_1)\Delta\omega(t_2) >$ to $2\Gamma\delta(t_1 - t_2)$. Plugging equation 3.31 back into equation 3.28 gives to lowest order

$$\rho_{12}(t) = \rho_{12}(0)e^{(i\omega_0 - \frac{\gamma_2}{2} - \Gamma)t}. \quad (3.32)$$

From equation 3.21 we see that the diagonal density matrix elements have no explicit dependence on the transition frequency ω_0, therefore small, time-dependent jumps should only affect the off-diagonal density matrix elements. Hence, we see that observables such as polarization can decay without a decay in population.

3.2.2.1 Decoherence-induced resonances

The addition of interactions to atomic (or quantum dot) systems that causes decoherence (or dephasing) of the superposition of two states can create new resonances in the nonlinear spectrum that are not observed in the absence of decoherence. In general, decoherence-induced resonances in two-level systems arise from the fact that certain perturbation amplitudes completely cancel in the absence of decoherence, but no longer destructively interfere in the presence of decoherence leading to additional resonances in the nonlinear response [143, 144]. In atomic gases, pressure-induced extra resonances from collisional decoherence in four-wave mixing (PIER4) have been predicted theoretically [145, 146] and observed [147, 148].

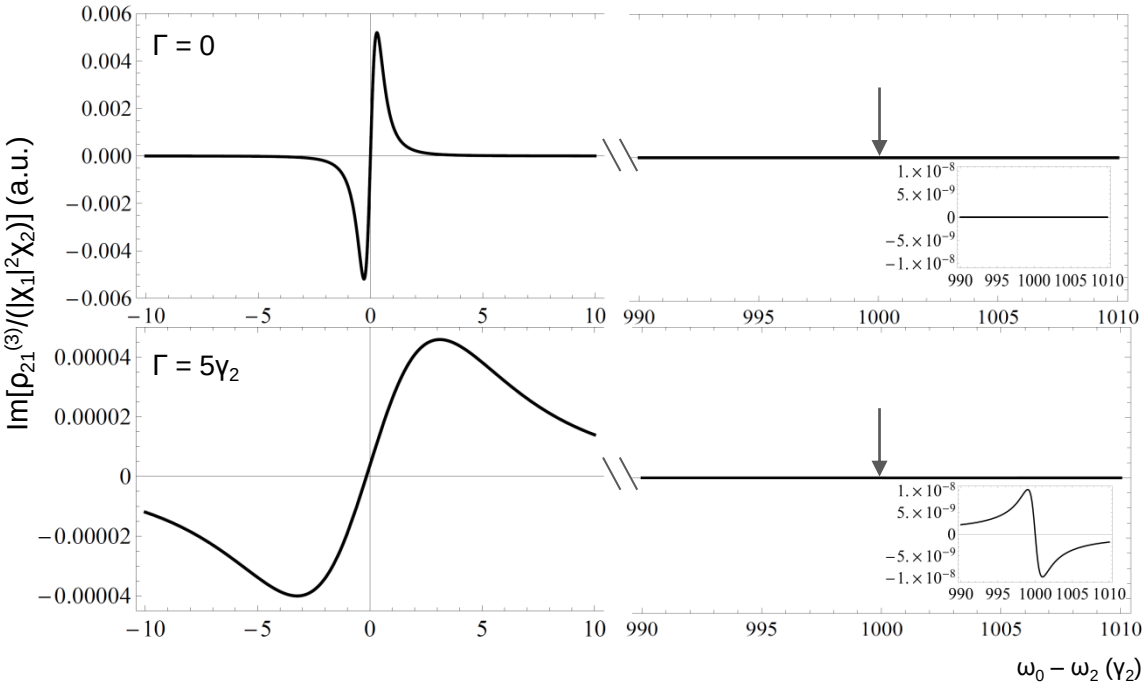

Figure 3.5: Imaginary component of the third order off-diagonal density matrix element as a function of ω_2 for a fixed ω_1, where ω_1 is given by the arrow on the right two panels. The top two panels show the response for zero pure dephasing. In the bottom two panels, the pure dephasing rate is taken to be $\Gamma = 5\gamma_2$. The insets in the right two panels show the same spectrum with the y-axis adjusted.

The effects of decoherence-induced extra resonances can be observed in the nonlinear optical interactions of closed two-level systems. In Fig. 3.5, we plot the nondegenerate third order response of a homogeneously broadened two-level system when the detuning $\delta_1 = \omega_0$ - ω_1 is much greater than the decay rate of the off-diagonal density matrix element γ with ω_1 fixed. In Fig. 3.5, we present the $\chi^{(3)}(\omega_2)$ spectrum for a fixed ω_1 detuning of $1000\gamma_2$ for both the zero dephasing case (top) and when $\Gamma = 5\gamma_2$ (bottom). In this case, the addition of pure dephasing causes a narrow interference-type resonance at zero ω_1 - ω_2 relative detuning that is not present with zero pure dephasing that is shown in the insets of Fig. 3.5.

3.2.2.2 Lineshapes with pure dephasing for closed two-level system

With the addition of pure dephasing, the third order nonlinear absorption line shapes become significantly different from the line shapes observed in Fig. 3.4. One of the most prominent effects is that the resonance in the PPT, $\propto \frac{2\Gamma}{\gamma_2 - i(\omega_2 - \omega_1)}$ becomes

non-zero, which generally gives rise to a narrow Lorentzian line that depends on the ω_2-ω_1 detuning. The narrow resonance that tracks with zero ω_2-ω_1 detuning is on top of a broad resonance that originates from the incoherent component of the third order signal. The broad resonance does not track with zero ω_2-ω_1 detuning and the width is $\propto \gamma$. In Fig. 3.6, we present the third order nonlinear absorption spectrum for two different values of pure dephasing. We see that the width of the narrow coherent population pulsation resonance shows no dependence on the pure dephasing rate while the width of the incoherent response scales with the level of pure dephasing, as stated.

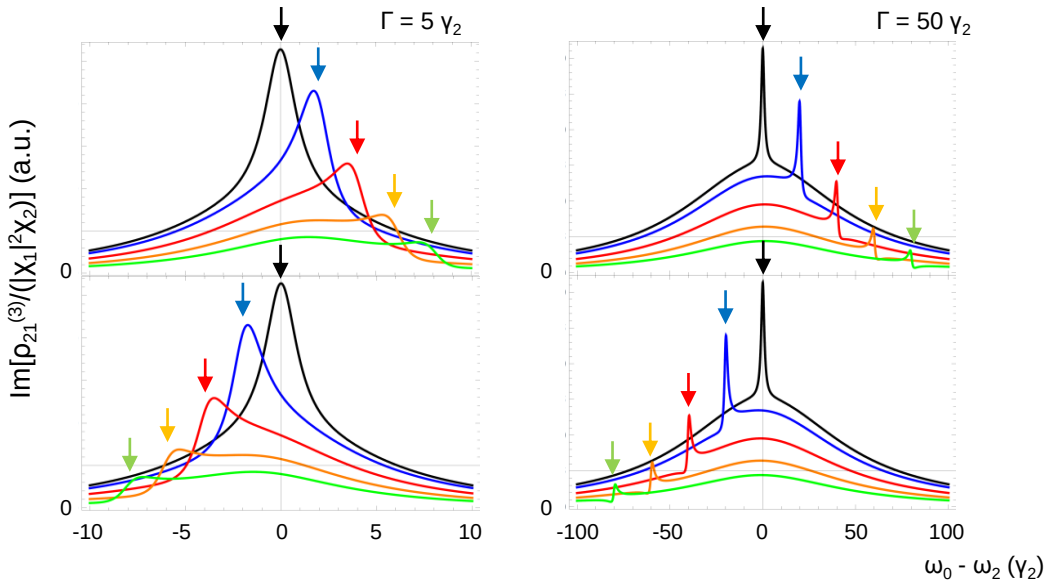

Figure 3.6: Imaginary component of the third order off-diagonal density matrix element with different values of pure dephasing (Γ) for a homogeneously broadened two-level system. The ω_1 frequency is given by the colored arrow, and the resulting third-order response as a function of ω_2 is given by the spectrum with the corresponding color.

It is important to note that the nonlinear signal strength of both the incoherent and coherent third order terms scales like $\frac{1}{\Gamma^3}$ for $\Gamma >> \delta_1, \delta_2, \gamma_2$. This means that

in systems with a large amount of pure dephasing, a significant nonlinear signal can usually only be detected (within our typical experimental sensitivity) using relatively high intensity electric fields compared to systems with low dephasing. It should be kept in mind that in order to extract meaningful lineshapes in the third order nonlinear optical spectrum, the intensities of the ω_1 and ω_2 beams must remain low enough so that the nonlinear optical signal is in the $\chi^{(3)}$ limit so that higher order terms do not come into play. At very high intensities, the power series expansion of the dielectric constant no longer applies [133]. We will see later on that homodyne detection of nonlinear signals requires that the nonlinear signal is linear in both the pump and probe intensities in the $\chi^{(3)}$ limit.

3.2.3 Coherent nonlinear absorption spectrum of two-level system with inhomogeneous broadening

This work features coherent nonlinear spectroscopy measurements on ensembles of DINWs. Many of the DINW excitons have different transition frequencies due to sample inhomogeneity. Sample specific sources of inhomogeneity will be discussed in later chapters. The inhomogeneity adds an additional source of broadening to laser absorption measurements since the absorption at each frequency must be averaged over the inhomogeneous distribution. In general, the dynamics of a group of excitons at a specific transition frequency may be entirely different from that of a different frequency group. Nevertheless, it is useful to consider, as an approximation, the linear and nonlinear absorption signal generated from an ensemble of identical two level systems with a distribution of frequencies. To simplify the discussion, we will consider that the transition frequencies of the two-level systems follow a Gaussian distribution.

In order to gain a foothold on the calculation of the complicated expressions involved in the third order density matrix elements including inhomogeneous broadening, we will first start with a simpler calculation of the linear absorption spectrum in an inhomogeneously broadened system. As stated, we begin with an ensemble of

two level systems, each with a linear absorption spectrum that is proportional to a Lorentzian function.

$$\alpha \propto \frac{\gamma}{\gamma^2 + (\omega_0 - \omega)^2}. \tag{3.33}$$

The transition frequencies of the ensemble are distributed according to the Gaussian distribution:

$$W(\Delta) = \frac{1}{\sigma_\omega \sqrt{\pi}} e^{-(\Delta/\sigma_\omega)^2}, \tag{3.34}$$

where $\Delta = \omega_0$ - $\bar{\omega}_0$ and $\bar{\omega}_0$ is the central frequency of the inhomogeneous distribution. The total absorption signal at a given laser frequency ω can be found by averaging the absorption profile of a single two level system over the distribution. Such an integration is proportional the convolution of a Lorentzian and a Gaussian:

$$\frac{\gamma}{\sigma_\omega \sqrt{\pi}} \int_{-\infty}^{\infty} d\Delta \frac{e^{-(\Delta/\sigma_\omega)^2}}{\gamma^2 + (\bar{\omega}_0 - \omega + \Delta)^2} = \frac{y}{\sqrt{\pi}\sigma_\omega} \int_{-\infty}^{\infty} d\xi \frac{e^{-\xi^2}}{y^2 + (\xi + x)^2}, \tag{3.35}$$

where $\xi = \Delta/\sigma_\omega$, y = γ/σ_ω, x = ($\bar{\omega}_0$ - ω)/σ_ω. The integral in equation 3.35 can be rewritten as

$$\begin{aligned} \frac{i}{2\sqrt{\pi}\sigma_\omega} \int_{-\infty}^{\infty} d\xi e^{-\xi^2} \left(\frac{1}{\xi + x + iy)} - \frac{1}{\xi + x - iy}\right) \\ = \frac{\sqrt{\pi}}{2\sigma_\omega} w(z) + c.c., \end{aligned} \tag{3.36}$$

where w(z) is the plasma dispersion function, given by

$$w(z) = \frac{i}{\pi} \int_{-\infty}^{\infty} d\xi \frac{e^{-\xi^2}}{z \pm \xi}, Im(z) > 0 = e^{-z^2}[1 - \Phi(-iz)], \tag{3.37}$$

where $\Phi(z)$ is the error function, which is defined as

$$\Phi(z) = \frac{2}{\sqrt{\pi}} \int_0^z d\xi e^{-\xi^2}. \tag{3.38}$$

The expression for the third order off-diagonal density matrix element including inhomogeneous broadening involves calculating the convolution of a Gaussian with the expression in equation 3.25. The detailed calculation is shown in Appendix A. The full third order expression for an inhomogeneously broadened two-level system is given by

$$\rho_{21}^{I(3)}(\boldsymbol{R},t) = -2i\chi_2|\chi_1|^2 e^{i(\boldsymbol{k_2}\cdot\boldsymbol{R}+\delta_2 t)}\frac{\sqrt{\pi}}{\sigma_\omega}([(1+\frac{2\Gamma}{\gamma_2})$$
$$\times\frac{1}{\omega_2-\omega_1+2i\gamma}(\frac{1}{\omega_2-\omega_1}(w(z(\omega_1))-w(z(\omega_2))+\frac{1}{2i\gamma}(w(z(\omega_1))+w(z_1(\omega_1)))]$$
$$+(1+\frac{2\Gamma}{\gamma_2-i(\omega_1-\omega_2)})[(-\frac{1}{\sigma_\omega}\frac{1}{\omega_1-\omega_2+2i\gamma}\frac{\partial w(z(\omega_1))}{\partial z}+(\frac{1}{\omega_1-\omega_2+2i\gamma})^2(w(z(\omega_1))+w(z_1(\omega_2))], \tag{3.39}$$

where

$$z(\omega) = \frac{\omega+i\gamma}{\sigma_\omega} \tag{3.40}$$

and

$$z_1(\omega) = \frac{-\omega+i\gamma}{\sigma_\omega}. \tag{3.41}$$

The third order off-diagonal density matrix element in equation 3.39 contains a coherent and an incoherent term. In an inhomogeneously broadened system both the incoherent term (also known as the hole burning term) and the coherent population pulsation term track with ω_1. In Fig. 3.7, the nonlinear response is plotted for both the case of no pure dephasing and including pure dephasing as a function of ω_2, where the colored arrows give the fixed value of ω_1. The inhomogeneous distribution is shown as the black dashed line in Fig. 3.7.

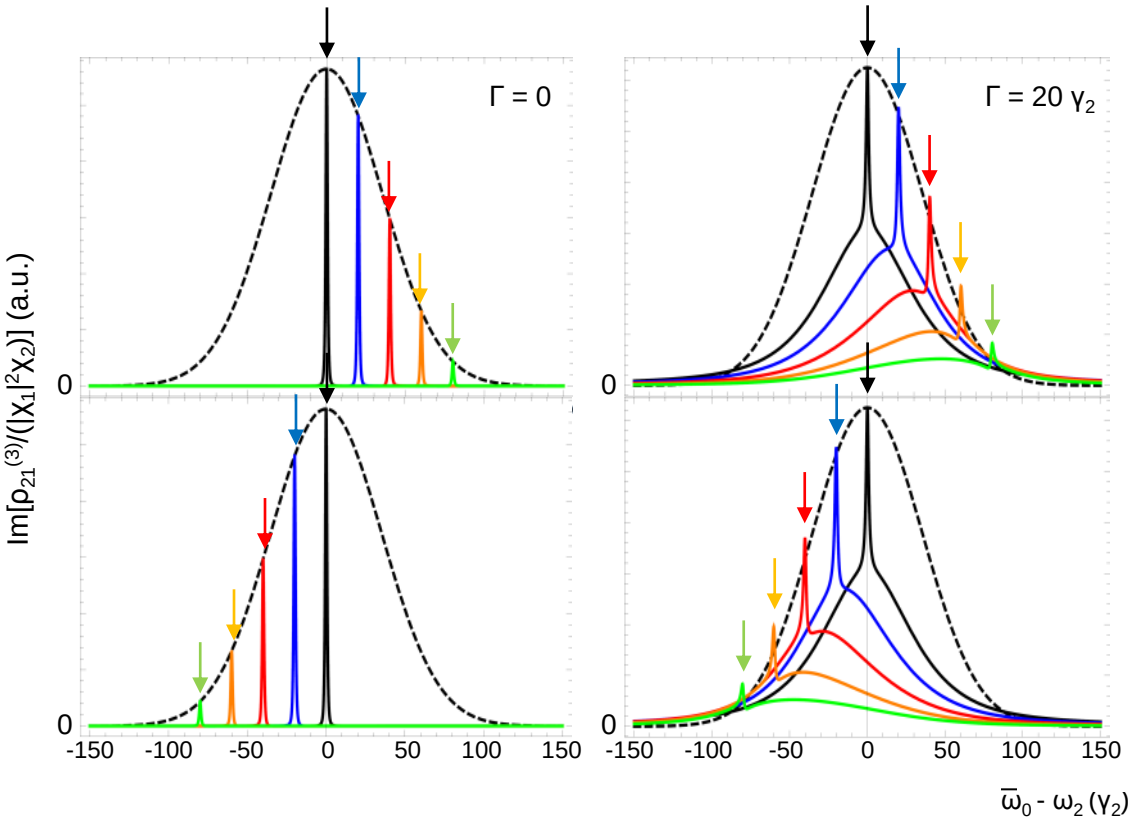

Figure 3.7: Imaginary component of the third order off-diagonal density matrix element with different values of pure dephasing (Γ) for an inhomogeneous distrubtion of two-level systems. The inhomogeneous distribution shown by the dotted-line Gaussian. The width of the Gaussian $\sigma_\omega = 50\gamma_2$. The ω_1 frequency is given by the colored arrow, and the resulting third-order response as a function of ω_2 is given by the spectrum with the corresponding color.

For a distribution of two-level systems with pure dephasing, the line width of the incoherent term is proportional to the dipole dephasing rate of the subgroup of two level systems pumped at ω_1 and the line width of the coherent term is proportional to the population decay rate of the subgroup, similar to a homogeneously broadened system. In the absence of pure dephasing, a single hole burning resonance is observed that tracks with ω_1. This is a very different effect from the interference-type line shapes observed in a homogeneously broadened system with no pure dephasing. With zero pure dephasing, a saturation-type line shape is always observed as long as ω_1 is tuned within the inhomogeneous distribution.

3.2.4 Spectral diffusion effects

As we saw earlier, random, time-dependent variations of the transition energy in a two-level system can provide a source of pure dipole dephasing as long as the time-dependent perturbations were fast enough. It is important to distinguish the effects of external perturbations that cause pure dephasing from those that cause spectral diffusion in two-level systems, a process that also causes dephasing. Spectral diffusion is essentially caused by perturbations that change the transition frequency of the two-level system where the time scale of the perturbation is greater than any population decay times in the system. Because of the slow dynamics of the transition frequency, spectral diffusion can essentially be thought of as a source of inhomogeneous broadening in the system with an inhomogeneous bandwidth given by σ_{SD}. The inhomogeneous distribution describes the possible energy states of the two-level system due to the external perturbation. Spectral diffusion has been observed in InGaN quantum dot systems when long-lived charges interact via Coulombic forces with excitons in close vicinity [149]. In InGaN systems, excitons are particularly sensitive to charge interactions due to the large built-in dipole moment.

In this section, we will write down the modifications to the density matrix equations of motion and the resulting steady-state density matrix elements from Refs. [130, 150]. Note that in the limit of fast spectral diffusion, where the rate of transition frequency variations $\Gamma_{SD} >> \sigma_{SD}$, the nonlinear absorption spectrum of the two-level system becomes qualitatively identical to the homogeneously broadened two-level system with a pure dephasing rate given by Γ_{SD}.

First, the modifications to the density matrix equations of motion are given by:

$$\begin{aligned}\dot{\rho}_{22}(\omega) &= \textstyle\sum_{\mu=1,2}[i\chi_\mu^*\rho_{21}^I(\omega) - i\chi_\mu\rho_{12}^I(\omega)] - [\gamma_2 + \Gamma_{22}(\omega)]\rho_{22}(\omega) + \int W_{22}(\omega',\omega)\rho_{22}(\omega)d\omega' \\ \dot{\rho}_{12}^I(\omega) &= \dot{\rho}_{21}^{I*}(\omega) = -\textstyle\sum_{\mu=1,2} i\chi_\mu^*\left[\rho_{22}(\omega) - \rho_{11}(\omega)\right] - [\gamma + \Gamma_{12}(\omega)]\rho_{12}^I(\omega)\end{aligned}, \tag{3.42}$$

where we now write the density matrix components explicitly in terms of the transition frequency ω, which is assumed to be a stochastic parameter. $W_{22}(\omega',\omega)$ is the redistribution kernel that takes a the two level system at frequency ω' to a state with frequency ω. The population decay term now has two components: γ_2 is the decay

rate of the excited state $|2\rangle$ back to the ground state $|1\rangle$ and $\Gamma_{22}(\omega)$ is the decay rate of the state at frequency ω to the excited states at all other frequencies.

To simplify the analysis in order to gain a qualitative picture of the steady state dynamics, we utilize the strong redistribution model [130,150]. The strong redistribution model assumes that the redistribution kernel is independent of the initial energy state of the two-level system so that $W_{22}(\omega^{'},\omega) = \Gamma_{SD}\mathrm{F}(\omega)$. The distribution $\mathrm{F}(\omega)$ is usually taken to be a Gaussian, $\frac{1}{\sigma_{SD}\sqrt{\pi}}e^{-(\Delta/\sigma_{SD})^2}$. The term $\Gamma_{22}(\omega)$ in equation 3.42 is then equal to the spectral diffusion rate Γ_{SD}. We also take $\Gamma_{12}(\omega) = \Gamma_{SD}/2$. We will consider that the system is closed, so that $\rho_{11}(\omega) + \rho_{22}(\omega) = \mathrm{F}(\omega)$. Note again that in a semiconductor quantum dot system, the excited state ρ_{22} represents the creation of an exciton with a transition frequency given by ω. The spectral diffusion process, such as a slow interaction with a charge or a physical hopping of the exciton to a new energy state, changes the transition energy of the exciton to $\omega^{'}$. The transition frequency ω is taken to be a stochastic parameter in the strong redistribution model [150], where the distribution of possible transition energies that the exciton can shift to is given by $\mathrm{F}(\omega)$. The resulting third order off-diagonal density matrix element is given by

$$
\begin{aligned}
&\rho_{21}^{I(3)}(\boldsymbol{R},t) = -2i\chi_2|\chi_1|^2 e^{i(\boldsymbol{k_2}\cdot\boldsymbol{R}+\delta_2 t)}\tfrac{\sqrt{\pi}}{\sigma_\omega}([(1+\tfrac{2\Gamma}{\gamma_2})\\
&\times\tfrac{1}{\omega_2-\omega_1+2i\gamma}(\tfrac{1}{\omega_2-\omega_1}(w(z(\omega_1))-w(z(\omega_2))+\tfrac{1}{2i\gamma}(w(z(\omega_1))+w(z_1(\omega_1)))]\\
&+(1+\tfrac{2\Gamma}{\gamma_2-i(\omega_1-\omega_2)})[(-\tfrac{1}{\sigma_\omega}\tfrac{1}{\omega_1-\omega_2+2i\gamma}\tfrac{\partial w(z(\omega_1))}{\partial z}+(\tfrac{1}{\omega_1-\omega_2+2i\gamma})^2(w(z(\omega_1))+w(z_1(\omega_2))]\\
&-2i\pi\frac{\Gamma_{SD}}{\sigma_\omega^2}\frac{1}{\gamma_2(\gamma_2+\Gamma_{SD})}w(z(\omega_2))[w(z_1(\omega_1))+w(z(\omega_1))]\\
&-2i\pi\frac{\Gamma_{SD}}{\sigma_\omega^2}\frac{1}{\omega_1-\omega_2+i\gamma_2}(\frac{1}{\omega_1-\omega_2+i(\gamma_2+\Gamma_{SD})})w(z(\omega_2))[w(z_1(\omega_1))+w(z(\omega_1))],
\end{aligned}
\tag{3.43}
$$

where $\gamma_t = \gamma_2/2 + \Gamma_{SD}/2 + \Gamma$ and

$$
z(\omega) = \frac{\omega + i\gamma_t}{\sigma_\omega}, \tag{3.44}
$$

$$
z_1(\omega) = \frac{-\omega + i\gamma_t}{\sigma_\omega}. \tag{3.45}
$$

The result is qualitatively very similar to the inhomogeneously broadened two-level

system with a Gaussian inhomogeneous distribution with 3 additional terms added due to the redistribution effects.

3.3 Probing energy transfer and excited state behavior

In this section, we begin to analyze the nonlinear signal beyond a single, closed two-level system. In solid state quantum dot structures, sometimes fixing the ω_1 beam at a certain energy and scanning ω_2 over a large range compared to the linewidth of any features near ω_1 can reveal different resonances, depending on the relationship between the energies of ω_1 and ω_2. This can be related to the fact that multiple neighboring quantum dots in a solid-state environment can be coupled together [151], resulting in coherent [152,153] or incoherent [48,154] energy transfer. It is also possible that the resonances are related to excited electronic states within a single quantum dot [155].

To give a simple example of how the nonlinear absorption signal can be used to identify optical physics related to energy transfer or excited state effects, we consider two quantum dot exciton transitions, A and B, generally from two different quantum dots. We assume that ω_A is greater than ω_B. We also assume that both quantum dots are at 0 K, so phonon absorption is frozen out. If the transitions are incoherently coupled, then the ω_2 beam will measure a resonance in the nonlinear absorption spectrum on both the A and B transitions when ω_1 is parked on resonance with the A transition, but will only measure a resonance on the B transition when ω_1 is parked on B (left side of Fig. 3.8). This is essentially because the state A can transfer energy to state B through emission of phonons, for example [108, 154]. If instead we consider transition B to represent the lower energy state of a quantum confined system and transition A to be the excited state, where the quantum dot system is again at 0 K, the ω_2 spectrum will contain both A and B resonances when ω_1 is parked on either A or B (right side of Fig. 3.8) [155]. This is because the excited state and lower energy state share the same ground state, so the excitation of either state results in a saturation of the ω_2 field. Generally, coherent energy transfer of two quantum

dot systems A and B can result in a similar absorption spectrum observed on the right hand side of Fig. 3.8, however this situation would be unusual if A and B have significant energy separation in solid state systems at 0 K.

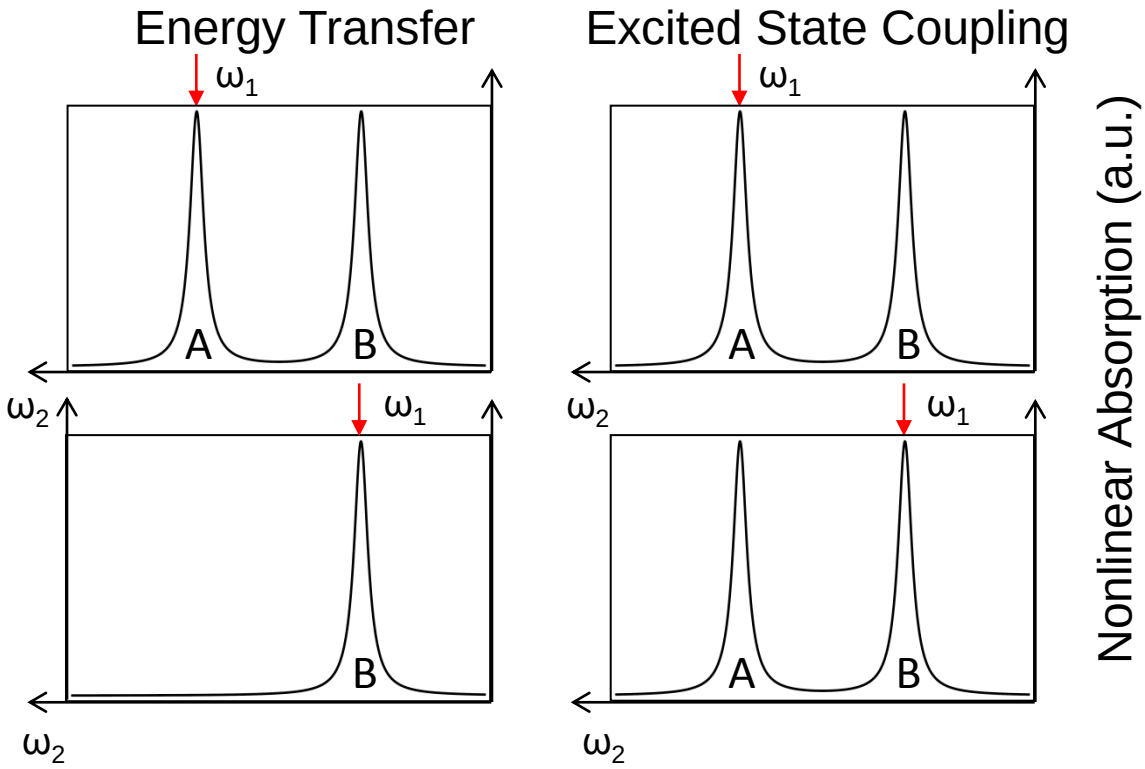

Figure 3.8: Qualitative schematic of the nonlinear absorption signal as a function of ω_2 for different fixed values of ω_1, assuming incoherent energy transfer (left) and absorption into an excited state (A) sharing a common ground state with the lower energy state of interest (B).

As mentioned in a previous chapter, incoherent energy transfer can have significant effects in the InGaN system due to relaxation of electron-hole pairs excited into the background disorder states. This effect will be explored further in later chapters.

3.3.1 Nonlinear response of a two-level system coupled to a metastable

state

In this section, we will consider the density matrix equations of motion describing a two-level system that is coupled to a third metastable trap state as a model for the DINW system. As mentioned, this analysis leads to essentially the same result that was first predicted by Lamb [156]. The laser fields ω_1 and ω_2 are sufficiently detuned from the trap state (on resonance with state $|2\rangle$ in Fig. 3.9 so that no trap state coherences are excited in the system.

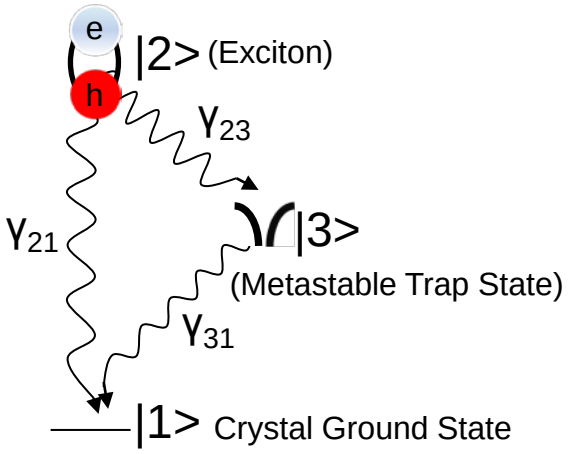

Figure 3.9: 3 Level system energy level diagram.

The density matrix equations of motion for a homogeneously broadened quantum dot exciton that is coupled to a metastable trap state as shown in Fig 3.9 are given by

$$\begin{aligned} i\hbar\dot{\rho}_{11} &= V_{12}\rho_{21} - c.c. + \gamma_{21}\rho_{22} + \gamma_{31}\rho_{33} \\ i\hbar\dot{\rho}_{22} &= V_{21}\rho_{12} - c.c. - \gamma_2\rho_{22} \\ i\hbar\dot{\rho}_{12} &= -\hbar\omega_0\rho_{12} + V_{12}(\rho_{22} - \rho_{11}) - \gamma\rho_{12} \\ \rho_{21} &= \rho_{12}^* \\ i\hbar\dot{\rho}_{33} &= i\hbar\rho_{22}\gamma_{23} - i\hbar\rho_{33}\gamma_{31}, \end{aligned} \tag{3.46}$$

where some of the population decay rates are shown in Fig. 3.9, $\gamma_2 = \gamma_{21} + \gamma_{23}$ and γ

$= \gamma_2/2 + \Gamma$. Solving equation 3.46 in steady state in a similar way to chapter 3 gives

$$\rho_{21}^{I(3)}(\boldsymbol{R},t) = i\chi_2|\chi_1|^2 e^{i(\boldsymbol{k_2}\cdot\boldsymbol{R}+\delta_2 t)}$$
$$\times\left(\frac{1}{(\gamma+i\delta_2)^2(\gamma-i\delta_1)}\left[1+\frac{2\Gamma}{\gamma_2-i(\omega_2-\omega_1)}\right]\left[1+\frac{\gamma_{23}}{\gamma_{31}-i(\omega_2-\omega_1)}\right]+\frac{1}{(\gamma+i\delta_2)(\gamma^2+\delta_1^2)}\left[1+\frac{2\Gamma}{\gamma_2}\right]\left[1+\frac{\gamma_{23}}{\gamma_{31}}\right]\right). \tag{3.47}$$

Equation 3.47 is identical to equation 3.25 except that there is an additional resonance in the nonlinear response that has a FWHM given by the decay rate from the metastable state into the ground state γ_{31}. When the condition $\gamma_{23} >> \gamma_{31}$ is met, the population pulsation resonance is dominated by the resonant denominator associated with the metastable state decay. This can be seen by comparing the nonlinear spectrum in Fig. 3.10a that shows the nonlinear response where $\gamma_{31} \sim \gamma_{23}$ to Fig. 3.10b where $\gamma_{23} >> \gamma_{31}$.

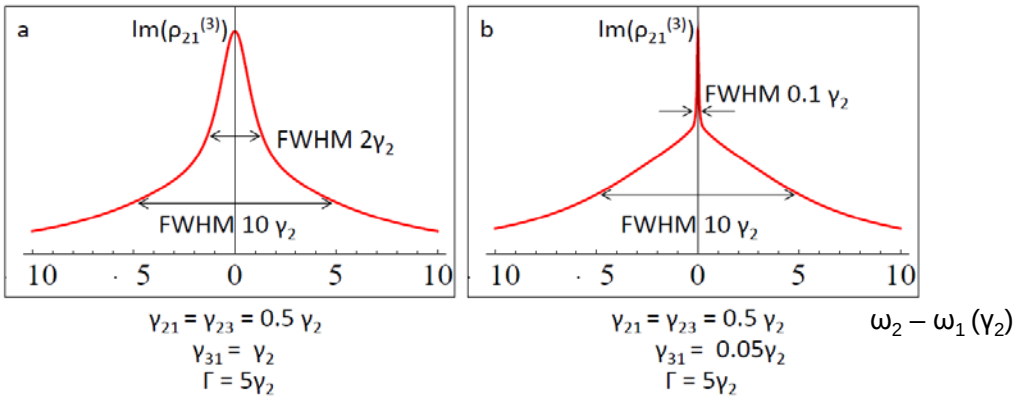

Figure 3.10: The imaginary part of the third order off-diagonal density matrix element for a two-level system coupled to a metastable trap state as a function of ω_1-ω_2 detuning for different trap decay rates.

3.4 Chapter summary

In this chapter we have thus far discussed the properties of closed two-level systems and incoherent coupling of multiple two-level systems. Another extension beyond the closed two-level system picture is when we consider an open two-level system. In this case, the decay associated with the ground state can lead to new (sometimes extremely

narrow) resonances in the nonlinear spectrum that are not otherwise observable in a closed two-level system [141]. We will see in a later chapter that multi-level systems are also often necessary to interpret experimental results, especially when the third level has a very slow decay rate, such as metastable trap state.

This chapter presented a theoretical overview of some of the third order nonlinear absorption line shapes for interactions with two laser fields in the pump-probe geometry. This chapter is meant to provide a starting point for theoretical analysis of line shapes in real solid-state quantum confined systems using the density matrix equations of motion. In well-behaved solid state systems such as GaAs quantum dots, the coherent nonlinear optical spectrum shows good agreement with the analysis presented in this chapter for zero dephasing. We will find later on that a theoretical analysis of coherent nonlinear optical line shapes in InGaN quantum dots is much less straightforward due to the presence of disorder that adds significant dephasing. Nevertheless, we will show that the two-level system picture can be a powerful toy model for understanding system dynamics in InGaN.

CHAPTER 4

Experimental techniques for taking coherent nonlinear spectroscopy data

Thus far, the coherent nonlinear optical properties of two-level systems has been discussed and the theoretical third order ($\chi^{(3)}$) absorption lineshapes were presented. It was also shown how the nonlinear signal is related to the polarization generated in the sample by the excitation beams. Measuring the nonlinear signal generated by the sample can be quite challenging as the signal level can be very small. As stated in the last chapter, the nonlinear signal of interest in our work is emitted along the ω_2 beam direction in Fig. 3.2. In a typical experimental set-up, the photocurrent generated by the nonlinear signal($\propto \chi^{(3)}(\omega_2)$) emitted along the ω_2 (scanning) beam direction, compared to the photocurrent signal generated by the the ω_2 field is 10^{-5}. Amplitude noise from the ω_2 beam generally makes it extremely difficult to measure the nonlinear signal accurately using direct photodetection. In order to detect a signal at this level, phase-sensitive detection techniques using lock-in amplifiers can be used. More specifically, we measure the homodyne signal between the ω_2 beam and the nonlinear polarization emitted along the ω_2 direction. This chapter will provide an introduction to phase-sensitive detection of coherent nonlinear optical signals and some experimental techniques used to take nonlinear spectroscopy data in the InGaN samples in this thesis.

4.1 Differential transmission technique for measuring nonlinear optical signals

To observe homodyned nonlinear optical signals, differential transmission techniques are utilized. In this technique, a first beam at frequency ω_1 is focused onto the sample along with a second beam at frequency ω_2 that is focused to the same spot as the ω_1 beam. The ω_1 beam is amplitude modulated, and the ω_2 beam is isolated from ω_1 in the far-field and detected by a photodiode as shown in Fig. 3.2. Using a lock-in amplifier that is synced to the modulation frequency of ω_1, the modulation of the sample absorption properties due to the presence of ω_1 can be detected by observing the differential transmission of ω_2. Specifically, this measurement is sensitive to

$$I_{\omega_2,\omega_1 on} - I_{\omega_2,\omega_1 off}, \tag{4.1}$$

where I is the photocurrent measured by the photodiode. Sometimes it may be necessary to modulate both ω_1 and ω_2 at different frequencies since for many samples the ω_1 beam is significantly scattered in the direction of ω_2 due to sample roughness. If both ω_1 and ω_2 are modulated, the nonlinear signal is detected at the difference of the modulation frequencies.

For simplicity, we assume for the moment that the scattering from the ω_1 beam in the direction of ω_2 is minimal, and only the ω_1 beam is amplitude modulated at frequency Ω_1. The differential transmission signal is proportional to:

$$dT \propto |E_2(\omega_2) + E^{(3)}_{sig}(\omega_2)(1 + Cos(\Omega_1 t))^2 + E^{(5)}_{sig}(\omega_2)(1 + Cos(\Omega_1 t))^4 + ...|^2 - |E_2(\omega_2)|^2 \tag{4.2}$$

where $E^{(3)}_{sig}(\omega_2)$ is the nonlinear amplitude of interest proportional to $|E_1|^2 E_2$ as discussed in a previous chapter and the $E_2(\omega_2)$ term is the amplitude of the transmitted ω_2 beam in the absence of ω_1. The lowest order surviving term in the dT signal is propotional to $2Re[E_2^* E^{(3)}_{sig}(1 + Cos(\Omega_1 t))^2] \propto |E_1|^2 |E_2|^2 v(Z,t)^{(3)}(1 + 2Cos(\Omega_1 t) + Cos(\Omega_1 t)^2)$, where $v(z,t)^{(3)}$ is the imaginary part of the third order polarization given in a previous chapter. The term $|E_1|^2 |E_2|^2 v(Z,t)^{(3)} 2Cos(\Omega_1 t)$ is measured by a lock-in amplifier using phase sensitive detection, a technique that will be described below.

If the beam intensity of either ω_1 or ω_2 is extremely high, higher order terms in the nonlinear response begin to dominate. In order to verify that the experiments

are performed in the $\chi^{(3)}$ limit, it is important to check that the differential transmission signal is linear in both the pump and probe intensities. Normally nonlinear measurements are taken with the intensity and wavelength of the ω_1 beam fixed while the ω_2 beam is scanned. The wavelength dependent transmission coefficient of the sample can lead to changes in the dT signal from the scanning ω_2 that are not caused by frequency dependent changes in the nonlinear polarization. In order to account for these changes, the dT signal is divided by the sample transmittance T that is measured using the ω_2 beam. The measurement of interest is therefore dT/T.

4.1.1 Phase-sensitive detection

In this section, some of the specific aspect of phase-sensitive detection using lock-in amplifiers will be discussed. For discussion simplicity, this subsection we will generally assume that only the ω_1 beam is modulated in phase sensitive measurements at frequency Ω_1, however it should be kept in mind that the measurements taken in this thesis were performed with double beam modulation where the ω_1 and ω_2 beams were modulated at frequencies Ω_1 and Ω_2. Techniques for proper phase sensitive detection with double modulation will be discussed in a separate subsection.

Measurements using a lock-in amplifier are very useful (as opposed to simply extracting a nonlinear signal from the magnitude of the photocurrent it generates) because the lock-in provides information about the phase of the nonlinear signal with respect to the lock-in reference phase. The output of the lock-in amplifier has two channels (X and Y) that correspond to the in-phase and in-quadrature components of the signal with respect to the reference. In our measurements, the lock-in phase is set so that a positive X channel signal corresponds to a signal that is in phase with the lock-in reference and a negative X channel signal corresponds to a π out-of-phase signal. In a single beam modulation set up, the lock-in reference frequency is synced to the modulation of the ω_1 beam at frequency Ω_1. Assuming that the photodetector in Fig. 3.2 measures no spurious signal due to scattering from the ω_1 beam, a positive X channel signal measured in the lock-in due to the nonlinear signal emitted along

the ω_2 direction implies a decrease in ω_2 absorption due to the ω_1 beam. Occasionally, the presence of the ω_1 laser field can lead to an induced absorption of the ω_2 field. In this case, more of the ω_2 field is measured at the detector due to the presence of the ω_1 field, resulting in a negative X channel signal.

In a previous chapter, the coherent nonlinear absorption spectrum was plotted using the imaginary part of the off-diagonal density matrix element as the dependent variable. It is important to note that the sign of the theoretical line shapes shown in chapter 3 follow the same sign convention as the X channel lock-in signal.

4.1.1.1 Phase modulation technique for observing nonlinear signals with a slow decay

Measuring a phase-sensitive nonlinear optical signal with a significant in-quadrature (Y channel) component can have interesting implications for the optical physics of the sample. Occasionally the system being measured using nonlinear spectroscopy techniques can have a very slow decay process due to a metastable energy state, for example. The presence of the metastable energy state can lead to a corresponding slow decay in the nonlinear optical signal. By comparing the X Channel and Y Channel components of the nonlinear signal measured using the lock-in amplifier, the decay rate of the metastable state can be measured. As an example, we consider some internal parameter of the system (such as an excited state population) x(t) that influences the nonlinear absorption signal. For an applied electric field given by $E_0(1+Cos(\Omega t))$ and a slow decay γ the resulting equation of motion for x(t) is given by:

$$\dot{x}(t) - \gamma x(t) = E_0(1 + Cos(\Omega t)). \tag{4.3}$$

Integration of equation 4.6 gives

$$x(t) = -E_0 \frac{-e^{\gamma t}\Omega + \Omega Cos(\Omega t) + \gamma Sin(\Omega t)}{\gamma^2 + \Omega^2}. \tag{4.4}$$

If the lock-in amplifier is set to be in-phase with the driving field modulation $Cos(\Omega t)$, we see that the ratio of in-phase X channel to in-quadrature Y channel of the nonlinear

signal due to x(t) is simply given by

$$\frac{X}{Y} = \frac{\Omega}{\gamma}. \tag{4.5}$$

By carefully measuring the ratio of the in-phase to out-of-phase lock-in signal, the decay rate of states in the system where $\gamma \approx \Omega$ can be accurately measured.

4.1.2 Double beam modulation dT/T signals

As stated previously, it is sometimes necessary to modulate both beams ω_1 and ω_2 at frequencies Ω_1 and Ω_2 and to detect the nonlinear signal at the difference frequency $|\Omega_1 - \Omega_2|$ due to scattering of the ω_1 beam in the ω_2 direction caused by sample roughness. To set the phase of the lock-in amplifier, we mix a sample of the pump and probe beams, arranged to be fully collinear in the photodetector, which is measured by the lock-in amplifier. We increase the power of both beams sufficiently until we detect a nonlinear photocurrent signal and we see a clear lock-in signal. The phase difference between the pump and probe beam is then adjusted until all the signal appears in the X-channel (recall the detector electronic bandwidth is large compared to the modulation frequencies). In this case a positive X channel dT/T signal still corresponds to an induced saturation of the ω_2 beam due to ω_1.

4.2 Set-up for nonlinear optical characterization

In this section, the optical set up for measuring nonlinear optical signals in InGaN DINW samples will be described. A large part of the optical set up is essentially standard for nonlinear optical measurements and has been extensively used in other nonlinear optical measurements in our lab (for example see refs. [48,56]). This section will focus on a few additions that were made to the usual set-ups in nonlinear optical measurements in our lab accommodate specific aspects of the InGaN DINW sample.

4.2.1 Double-pass acousto-optic modulator set-up for beam modulation

To modulate the ω_1 and ω_2 beams, the two beams are sent through separate

traveling wave acousto-optic modulators (AOMs) and the m = 1 diffraction order is amplitude modulated using two phase-locked function generators. The AOMs are used for beam modulation over traditional optical choppers for two main reasons: first, it is possible to electronically control the output intensity of the m = 1 order, which is useful for noise eating applications, and second, it is easier to achieve high frequency (∼MHz) modulation frequencies that are not available using traditional optical choppers.

Although using an AOM for beam modulation has some advantages over traditional mechanical choppers, a significant disadvantage of using an AOM is that the output angle of the m = 1 beam varies as a function of input wavelength. The traveling-wave AOMs in our experiment are usually driven by a 40 MHz RF signal, therefore the output angle of the m = 1 diffraction order is given by [157]

$$Sin(\Theta) = \frac{\lambda}{v_s/40MHz}, \tag{4.6}$$

where λ is the laser wavelength and v_s is the sound velocity in the AOM material, which in this case is 3630 $\frac{m}{s}$. Measuring the complete nonlinear optical spectrum of InGaN DINW ensembles requires tuning of ω_1 and ω_2 of (∼100 nm) due to large linewidth features. Typically the ω_1 and ω_2 beams are focused onto the same spot on the sample surface using a single objective lens, therefore the angular displacement of the beam caused by the AOM is translated to a change in position of the focal spots on the sample surface, which is highly problematic inhomogeneous InGaN DINW samples. One way to prevent this issue is to send both the ω_1 and ω_2 m = 1 beams through optical fibers before reaching the sample. The angular displacement provided by the AOMs is still problematic in this situation however, since the coupling into the optical fiber is affected by the m = 1 angular variation caused by the large wavelength tuning. Typically a tuning of ∼50 nm leads to a decrease in fiber output of around 80%. Although this decrease in output power can be often accounted for on the output end of the fiber, for lower noise automation it is generally more desirable to use the most optimized fiber coupling.

A method for circumventing the angular displacement issue for large beam tuning

was first discussed in ref. [158] and was utilized in the nonlinear optical setup in this work. A schematic of the experimental implementation of the technique is shown in Fig. 4.1. First, the input beam is sent through a polarizing beam splitter so that H polarized light emerges from the output of the beam splitter. This light is then sent through the traveling wave AOM where ∼60-70% of the light is coupled into the m = 1 diffraction order. Note that it may be necessary to optimize the beam size with a telescope before the beam enters the AOM for maximum coupling into the m = 1 diffraction order. Next the beam is sent through a plano-convex lens with a focal length f1 at a distance f1 away from the AOM so that the m = 1 beam propagates in a parallel direction to the m = 0 beam. After passing through the lens, the beams are sent through a quarter wave plate with fast and slow axes aligned at 45 degrees with respect to the H polarization direction. This creates circularly polarized light that propagates toward a mirror. Before the m = 0 and m = 1 beams can hit the mirror, the m = 0 beam is blocked. The mirror face should be completely perpendicular to the beam propagation direction so that the k vector of the m = 1 beam is reversed and the reflected polarization is circularly polarized light of the opposite orientation compared to the incident polarization. Because the reflected circularly polarized light is now of the opposite orientation compared to the incident beam, the polarization becomes vertical after the second pass through the QWP. The vertically polarized light passes through the AOM again and ∼60-70% is diffracted exactly along the incident m = 0 beam direction. The optical wavelength of the beam is shifted by 80 MHz due to the double diffraction through the AOM. The vertically polarized light is then reflected by the polarizing beam splitter and is fiber coupled away from the AOM. The fact that the $\boldsymbol{k}$ vector of double-pass diffracted beam is eventually the negative of the incident beam makes the fiber coupling efficiency insensitive to wavelength. It should be noted that almost 65% of the incident power is usually lost, not including the fiber coupling efficiency, therefore this technique should only be used if there is a significant incident beam power and losses do not affect the experiment.

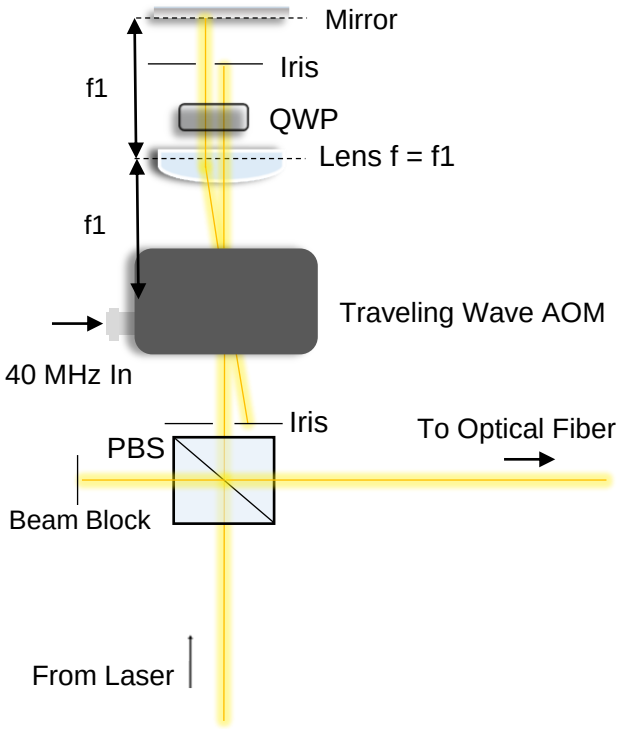

Figure 4.1: Diagram of double-pass AOM setup

4.2.2 Overview of optical setup

As we will in later chapters, the typical dephasing rate in the InGaN DINW system is very large compared to III-As nanostructures at low temperature. Large dephasing rates have also been reported in InGaN quantum wells at low temperature [100]. Recall that the third order nonlinear optical signal found scales like $\frac{1}{\Gamma^3}$ in the limit of large Γ in the $\chi^{(3)}$ term. The large dephasing rates in InGaN DINWs implies that a much larger beam intensity is required to observe a nonlinear signal for a given

experimental sensitivity compared to III-As systems, assuming that the intensity is low enough for the signal to be in the $\chi^{(3)}$ limit.

In order to achieve higher intensity sample excitation, we added an NA = 0.55 microscope objective to the system in place of the usual f ∼100-200 mm lenses used for nonlinear optical measurements in III-As systems. The microscope objective was also used in conjunction with a white light source to image the surface of the sample and selectively excite certain sample areas. The entire optical set up is shown in Fig. 4.2. The addition of the microscope objective was key in observing the first nonlinear optical signals. Imaging the sample surface also helped tremendously in aligning the ω_1 and ω_2 beams to achieve the maximum dT/T signal.

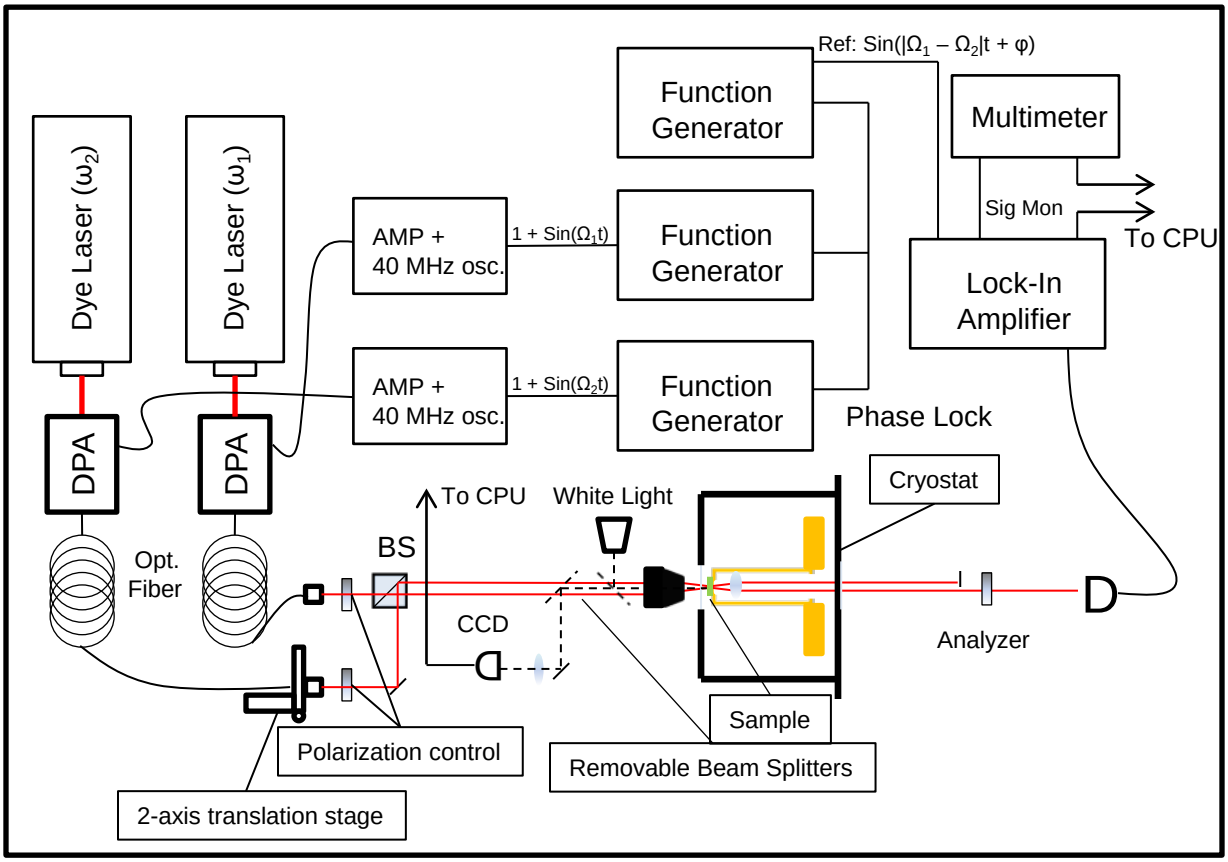

Figure 4.2: Optical set up for nonlinear optical measurements.

The two excitation beams ω_1 and ω_2 are provided by two frequency stabilized dye lasers (Spectra-Physics Matisse DX and Coherent 899-29, each with a coherence bandwidth of 1 MHz). The excitation beams are each immediately coupled into a double-pass AOM (DPA) set-up as shown in Fig. 4.2. After passing through an optical fiber, the beams are then aligned to focus onto the sample. It is imperative that the beams are completely parallel (but non-overlapping) entering the objective lens or else the beam overlap on the sample will be too small to observe an appreciable signal. To ensure that the beams are parallel but non-overlapping, both beams are made to be parallel and overlapping by coupling the two beams into a single optical fiber that is placed in front of the sample and maximizing the coupling efficiency. The optical fiber is then removed and the output port of 1 beam is spatially adjusted using an X-Y translation stage. This motion does not affect the angle of the beam, and as a result the two beams can be completely parallel but non-overlapping. Adjustment of the two beams into the microscope objective for maximum nonlinear signal can be done using external mirrors or a differential micrometer translation stage that holds the objective (not shown in fig. 4.2). This translation stage also allows us to excite different regions of the sample.

In order to maintain the sample at cryogenic temperatures, the sample is cooled using an ST-500 microscopy cryostat. This cryostat was necessary to acquire for this experiment due to the high NA of the focusing microscope objective. In the standard operating mode of the ST-500, the sample rests on a cold finger and data is taken in a reflection geometry. The reflection geometry is usually not desired in nonlinear optical measurements due to phase shifts in the reflected beam [159,160]. In order to allow for nonlinear optical measurements in a transmission geometry, a small threaded hole was machined into the bottom of cold finger to allow for an aspheric lens to be screwed in. The threaded hole stops near the top of the cold finger, where a smaller diameter hole is drilled through that allows the beam to pass though while maximizing the contact of the sample and cold finger. The distance between the top of the cold finger and lens is adjusted until the beam passing through the sample is roughly collimated going through the cold finger. The back end of the cryostat has

an additional window to allow for beam transmission.

Using a white light source and removable beam splitters, the sample surface can be imaged using a DCC1545M CCD camera. The camera is interfaced to the CPU using a USB port. The optical alignment of beams and the position of the sample in the experimental field of view is verified using the CCD image.

4.3 Chapter summary

In this chapter phase sensitive detection techniques were discussed for measuring coherent nonlinear optical signals. Although the techniques and optical set ups for phase sensitive differential transmission measurements have been discussed in previous work, our experimental set up required modification from the conventional system to perform nonlinear spectroscopy in the InGaN system. The modifications included the addition of an NA = 0.55 microscope objective for focusing both excitation beams, the use of a double-pass AOM set up and the addition of a microscope cryostat. These modifications allowed us to measure new optical physics in the system that will be the subject of the next chapters.

CHAPTER 5

Self-assembled InGaN dots-in-nanowires grown on Si substrates

The experimental goals in the study featured in this chapter are to understand the physics associated with the nonlinear optical response of self assembled InGaN disks-in-nanowires on silicon substrates. Growth of DINWs on silicon and the subsequent demonstration of DINW laser devices is also important for silicon-based photonics applications that may require an on-chip laser source [161]. As noted in the previous chapters, the characterization is motivated by the use of the DINWs in coherent control applications such as quantum information processing. The nonlinear optical data shows a spectrum comprised of a nonresonant component arising from the disordered states and several strong resonant components giving clear presence of excitons. We compare the nonlinear optical properties of different groups of excitons at room temperature and low temperature and find that the linewidths of some groups of excitons at room temperature is virtually unchanged compared to the groups at low temperature. The strong excitonic response shows no evidence of many body physics. This is consistent with the optical excitation being confined in a small region that is dot-like, exhibiting strong quantum confinement, a result anticipated by early TEM measurements [9,12,162] and the observation of single photon emission in similar samples [12]. We observe that the nonlinear signal has a long decay time $\sim \mu$s, which we attribute to interactions between the excitons and long-lived trap states. If growth conditions can be developed to minimize the role of traps and disorder states, the data indicates the InGaN samples could be viable for exciton based quantum logic devices at room temperature.

5.1 MBE growth of GaN nanowires with InGaN disks

Prior to a presentation of the optical data, some of the growth techniques of the DINW samples in this thesis will be presented. The InGaN disk-in-nanowire (DINW) samples featured in this chapter and the next two chapters were grown using plasma-assisted MBE (molecular beam epitaxy). MBE growth normally requires inserting the substrate into a growth chamber that is pumped to an ultra-high vacuum environment ($\sim 10^{-8} - 10^{-10}$ torr). To grow the GaN nanowires that provide the base of the DINW structure, N_2 is first introduced into the growth chamber and broken into atomic N using a radio-frequency plasma. The surface of the sample is then bombarded with Ga atoms that originate from a Ga effusion cell. Under proper growth conditions in the nitrogen-rich environment (temperature and gallium flux), GaN can begin to nucleate into small clusters [163]. The GaN nucleation process occurs when a balance is struck between temperature and Ga flux from the effusion cell. Typically at lower temperature and higher gallium fluxes, epitaxial layers of GaN form instead of the nuclei. Above a certain temperature, no growth of GaN occurs at all. The phase diagram for Ga nucleation is shown in Fig. 5.1 from Ref. [6]. The nuclei form the first building blocks of the GaN nanowire section that forms coherently on top of the Ga nuclei.

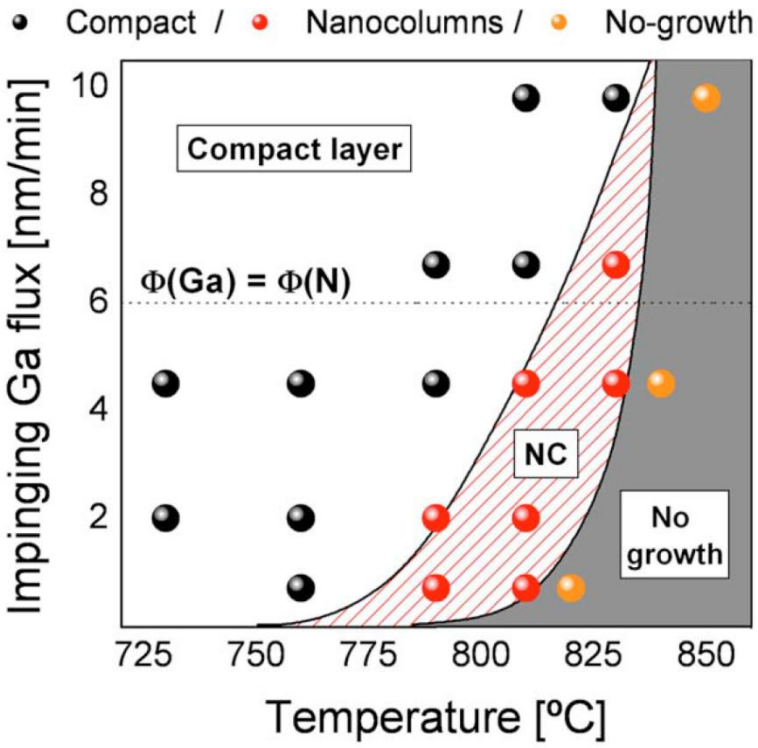

Figure 5.1: Phase diagram for nucleation of GaN from Ref. [6]

After the GaN nanowires are grown to ∼500 nm in length on top of the GaN clusters, growth of the InGaN layers is initiated. Growth of InGaN requires a lower temperature (∼520°) than the typical growth temperatures of GaN nanowires shown in Fig. 5.1 because of the low sticking coefficient of InGaN adatoms [55]. The emission energies of the InGaN sections can be colored-tuned depending on the temperature [18]. Generally lower temperature substrates (∼510° C) result in red emitting InGaN layers and higher temperature substrates (∼530° C) result in blue emission [55]. At lower growth temperatures, the InN diffusion is very weak, resulting in a large concentration of nonradiative defects in the InGaN layer [55].

5.1.1 Spontaneous MBE growth of GaN nanowires with InGaN disks

The spontaneously grown samples featured in this work were grown on Si by Saniya Deshpande and Shafat Jahangir in Professor Pallab Bhattacharyas research lab. The InN concentration in the sample is ∼0.54, which gives a red emitting sample. In this section some of the basic aspects of the spontaneous growth technique will be highlighted. More details of the growth procedures for InGaN DINWs can be found in Refs. [55]

Prior to growth of the GaN nanowires, the substrate must be prepared. Since the substrate in this case is Si, the effects of oxidation on the Si surface during the short time when the substrate is moved from the lab to the MBE chamber must be counteracted. To counteract this effect, the oxide layer on the surface of the substrate is removed by heating in the MBE chamber. Furthermore, the heating provides degassing to the substrate surface. After the oxide is removed, N_2 is introduced and broken into atomic N using a radio-frequency plasma. The growth of GaN begins when Ga atoms are introduced into the nitrogen-rich environment. When the Si substrate is exposed to a nitrogen-rich environment, the Si and N react to form layers (3-5 nm thick) of Si_xNi_y, where x and y depend on the concentration of N.

GaN clusters that grow into nanowires are formed on top of the Si_xNi_y layer. The thickness of the Si_xNi_y layer is generally not uniform across the substrate surface and as a result the growth angles of the spontaneously grown nanowires can vary significantly across the sample. Variations in the growth angles of the nanowires can lead to the coalescence of multiple nanowires with different growth angles. The coalescence can have several effects [164]. First, coalescence can result in the coherent overgrowth of a larger diameter nanowire from the bridging of two smaller diameter nanowires. This can give a large variation in the nanowire sizes throughout the sample and generally occurs for small growth mismatch between the DINWs. In addition to bridging overgrowth, the formation of defects can also occur between the two merged nanowires for small misorientation angles. These defects can act as traps for charge carriers [164]. More extreme growth angle misorientation can result in long chains of defects that can quench the sample emission [164].

The lattice mismatch between GaN and Si in self-assembled samples leads to a significant density of dislocation defects at the base of the GaN nanowire. In InGaN quantum wells, the dislocation defects provide a large source of nonradiative recombination of 2-D excitons as noted in chapter 2. In nanowires, the small diameter of the nanowires and the ease of propagation of the dislocation defect along directions perpendicular to the growth axis means that the dislocations rarely propagate into the active InGaN region [119].

5.1.2 Sample preparation for optical studies

Usually it is desirable to perform nonlinear optical measurements in a transmission geometry where the excitation beams pass through the sample and are detected on the other side. In a reflection geometry, phase shifts resulting from the surface reflection can make the interpretation of the nonlinear signals more complicated [159, 160]. To allow for transmission measurements, the DINWs are removed from the Si substrate using a sonication technique and dispersed onto a sapphire substrate at an areal density similar to the growth density.

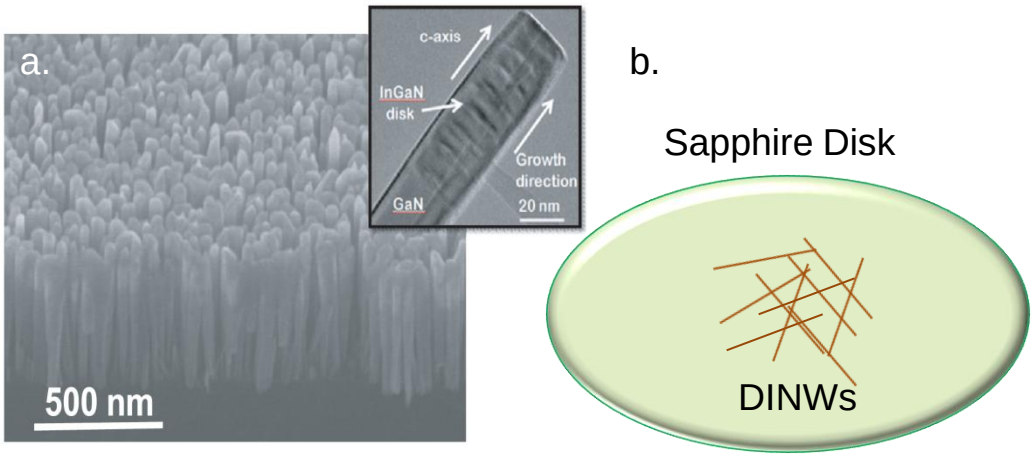

Figure 5.2: ***a.*** SEM image of a similarly grown self-assembled sample along with a TEM image of a single DINW in the inset, from Ref. [7] ***b.*** Schematic of the dispersed nanowires on a sapphire disk

In the sample featured in this chapter, we estimate that the areal density of nanowires is $\sim 10^{11} cm^{-2}$, the same order of magnitude as the growth density. The nanowires have a ~30 nm diameter with 2 nm thick InGaN regions. Each nanowire

contains 8 InGaN disks separated by 15 nm of GaN. The effects of defects due to nanowire coalescence have a serious impact on the optical properties of the DINWs. As noted earlier, defects formed due to coalescence can lead to quenching of the DINW exciton emission as the defects can act as nonradiative recombination centers [165]. As a result of coalescent defects, we estimate that only a small percentage (∼3-8%) of the nanowires are able to produce luminescence and/or absorb light [165]. This makes the effective areal density of nanowires probed in this study closer to ∼3-8 $\times 10^9 cm^{-2}$.

5.2 Preliminary sample data: PL, PLE and modulated absorption

Preliminary spectroscopy measurements are based on a combination of linear spectroscopy (PL and PLE) and nonlinear optical modulation spectroscopy. In both the PL and modulation spectroscopy measurements, a $\lambda = 405$ nm pump beam is focused to a spot size $\sim 1\ \mu\text{m}^2$, thus exciting ∼30-80 nanowires or ∼240-810 DINWs. We utilize a confocal microscopy system in our set-up to probe approximately the same region on a day-to-day basis and at different temperatures, however we found that the limited resolution of the system leads to some changes in the spectra for different measurements (taken on different days) and at and different temperatures.

We present PL and PLE data in Fig. 1. The PL is centered at ~ 1.98 eV with a width of ~ 480 meV. As a rough approximation, we fit the PL peak to a Gaussian (red line in Fig. 5.3). It is clear from the data in Fig. 5.3 that the PL data is not a smooth Gaussian resonance, but is rather composed of resonant structures. The origin of the resonant structures will be discussed later on. Inhomogeneous broadening from different sized nanowires, fluctuations in InN concentration or perhaps from background disorder state emission can lead to the broad PL emission observed in Fig. 5.3 [7, 164–168]. The PLE data shows an increasing spectrum as a function of energy. The PLE overall appears to follow exponential function (blue line in Fig. 1), however we again see that there is resonant structure within the PLE. We associate the exponential dependence in the PLE spectrum to a large density of disorder states

in the system formed perhaps by random InN alloy fluctuations [96] or heterostructure interface fluctuations [87].

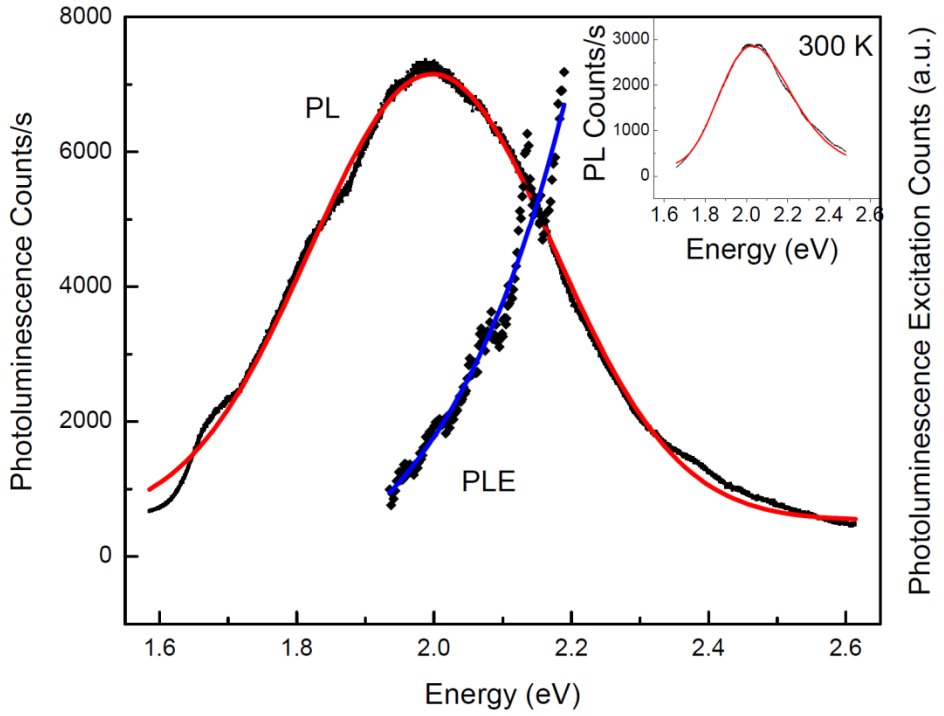

Figure 5.3: Photoluminescence (PL) and photoluminescence excitation (PLE) at 10K. The inset shows similar PL at room temperature from a similar sample ensemble, the shift reflecting the role of heterogeneity.

The modulated absorption data is presented in Fig. 5.4. Optical modulation spectroscopy in this work based on using a cw blue laser (at $\lambda = 405$ nm) to modulate the optical properties by exciting e-h pairs and then probing the resultant change in the absorption spectrum. A general review of modulation spectroscopy in semiconductors is provided in ref. [169]. Using phase sensitive detection, we set the phase so that a positive signal reflects an increase in transmission corresponding to a reduction in absorption. A simple saturation of the absorption reflected in the PLE would reproduce the basic exponential function seen in Fig. 5.4. The data in Fig. 5.4 (at both 10 K and 300 K) show a highly structured response comprised of multiple resonances. The data has a constant negative offset (indicating an optically induced increase in absorption) that has been subtracted in Fig. 5.4. Original data at 10 K without

background subtraction is shown in the inset of Fig. 5.4.

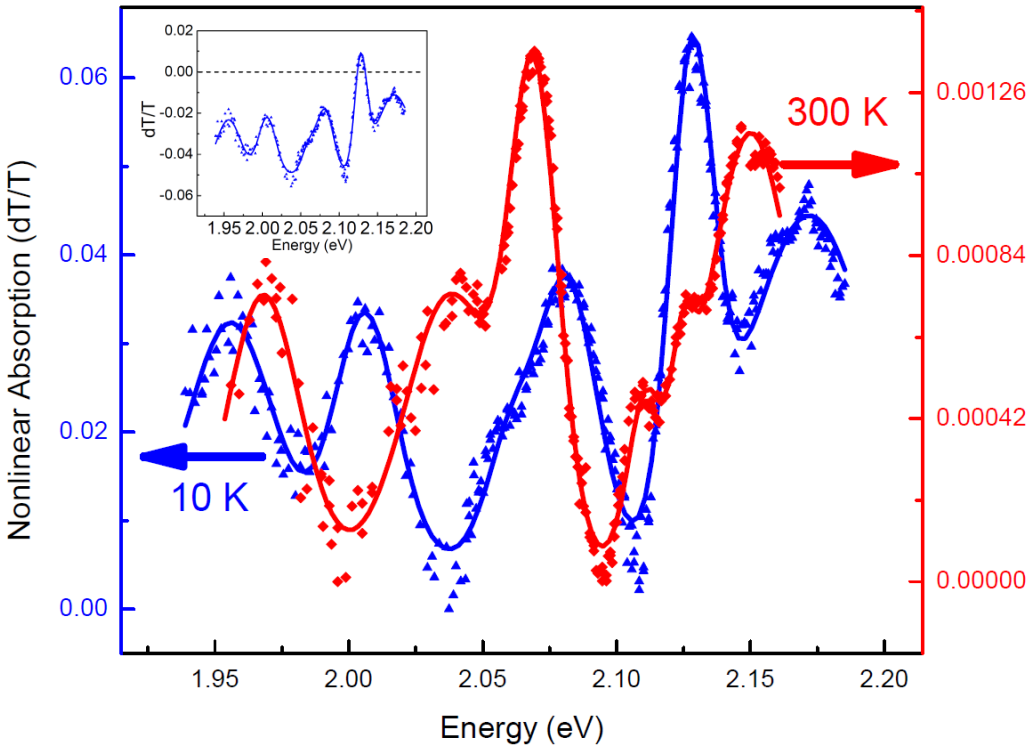

Figure 5.4: Modulated absorption where a more positive signal means reduced absorption (increase in transmission) showing strong excitonic features at 300 K and 10 K. There are variations in the relative positions and strengths of the resonances at 300 K and 10 K since: 1. the two spectra are taken at two different regions of the sample, and 2. an overall redshift of the spectra occurs as the temperature increases, as reported in ref. [7]. The constant negative offset is subtracted. Inset shows data with the constant negative offset included.

The increase in transmission associated with these resonances and the absence of first or second order derivative type structure that one would see in the presence

of many body effects arising from optically generated carrier induced energy shifts or broadening is consistent with a saturation of the response. We rule out that the resonances are related to optical effects such as Fabry-Perot resonances for several reasons. First, and most importantly, the frequency spacing between the resonances $\Delta\nu \approx 12$ THz would give a Fabry-Perot cavity length of $\sim$5 μm, assuming the index of refraction of GaN = 2.32 at 10 K [170]. The sample consists of a layer of DINWs with an average thickness $\sim$30 nm and random orientations on the uncoated substrate surface; therefore there is no structure in the system that could give rise to such resonances. Furthermore, as shown in Fig. 5.5, the transmission was monitored and compared to the modulated absorption to ensure no such structures were present.

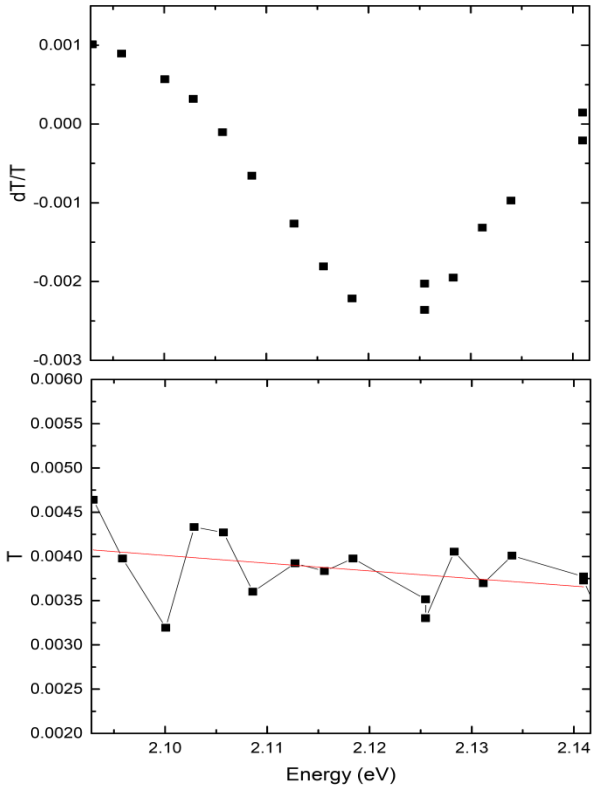

Figure 5.5: Transmission (bottom panel) and modulated absorption (top panel) of the sample at room temperature.

Unlike in III-V material, it is remarkable that the strong excitonic features persist at room temperature. Note that the data taken at 10 K and 300 K may be taken

at slightly different regions of the sample (spaced by ∼1-3 μm) due to the limited resolution of our confocal microscope set-up, therefore the resonances may not originate from the exactly the same groups of excitons. At the same time, it is important to notice that some features, in particular the large modulated absorption resonance near $\omega = 2.125$ eV at 10 K, seems to exist in both the low temperature and room temperature data. At room temperature the resonance should be red shifted due to the temperature dependence of the material band gap. We note that the relative energy spacing of this resonance at room temperature and low temperature is $\Delta E \approx 48.15$ meV. This is in good agreement with the temperature-dependent band gap energy shift expected from the Varshni equation [171], $\Delta E = 48.5$ meV, assuming the Varshni parameters $\alpha = 0.55$ and $\beta = 719$ [172]. This strongly suggests that a group of DINWs with very similar geometries that absorbs around $\omega = 2.125$ eV is probed in both the low temperature and room temperature measurement. It is remarkable that the line widths of some features appear to be so similar in both low temperature and room temperature, a feature that validates the temperature stability of excitons in the system.

In Fig. 5.6, we compare the modulation absorption spectrum at 10 K to the residuals of the Gaussian fit to the PL spectrum and exponential fit to the PLE spectrum. Although resonances in the three spectra do not overlap in some places due to slight differences in the probed sample region, we believe that there is enough similarity between the 3 spectra to suggest that the variations observed in the PL and PLE in Fig. 5.6 originate from the same excitons observed in the modulated absorption spectrum.

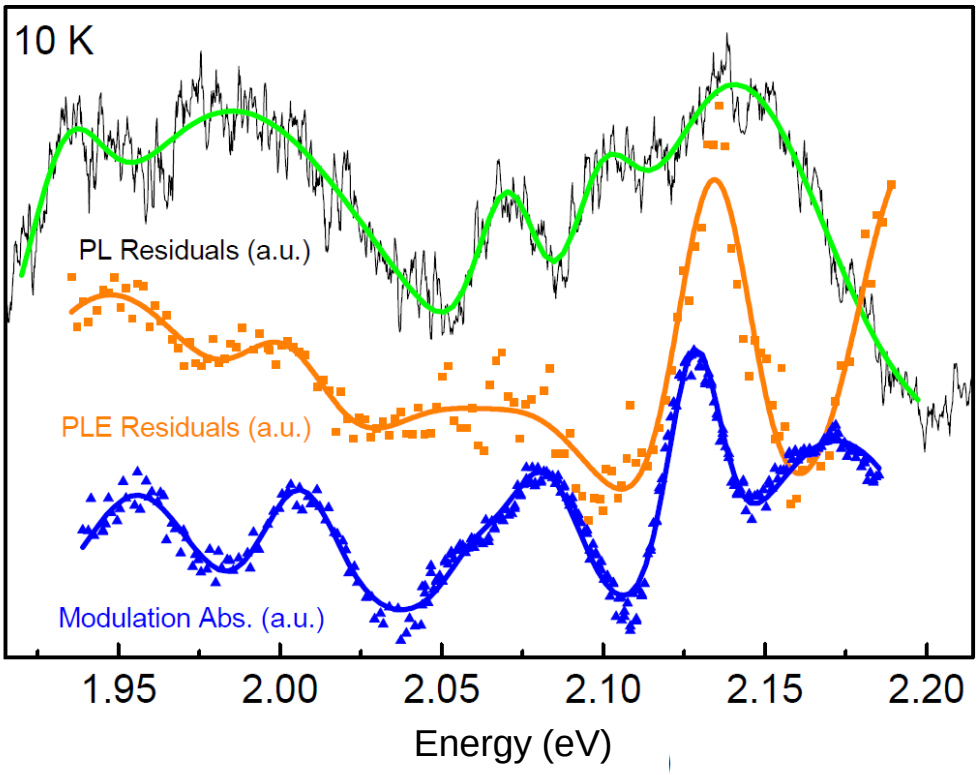

Figure 5.6: A comparison of the residuals of a Gaussian fit to the PL, exponential fit to the PLE and the modulated absorption data at 10 K

5.3 Coherent nonlinear optical spectrum

In this section, the coherent nonlinear optical response is presented. Unless otherwise indicated, the spectra are taken with ω_1 fixed and ω_2 scanned.

The absence of additional structure or more complex line shapes in the nondegenerate differential transmission spectrum, shown in Fig. 5.7, is again consistent with the absence of many body effects. Surprisingly, however, the nondegenerate response is virtually independent of the frequency of the non-scanning field in the range shown in Fig. 5.7. The spectrum, for say heterogeneous two-level systems coupled by F$\ddot{o}$rster energy transfer, from higher energy two-level systems to lower energy systems would show only resonances below the frequency of the non-scanning field [48]. Coherent coupling between such systems through say Coulomb exchange would show resonances above and below the non-scanning field frequency but the strength of the

response would increase as the non-scanning frequency approached a resonance. This response would be similar to that observed for an n-level system when two or more low lying levels with transitions to a common excited state (Λ-system) or two or more excited states with transitions sharing a common ground state (V-system). A many body response would also be expected to depend strongly on the pump frequency and typically show a more complex spectral structure. Hence, we conclude the physical origin of this response does not correlate with those observed in typical optical materials. We note that for very large ω_1 - ω_2 detuning, off of the scale of the spectrum shown in Fig. 5.7, where $\omega_1 < \omega_2$, the nonlinear optical response appears to be much weaker. Thus, it may be more accurate to say that the data in Fig. 5.7 shows a very weak dependence on ω_1 over the range of ω_1 values presented in Fig. 5.7 and eventually the signal level should go to zero for very low energy ω_1.

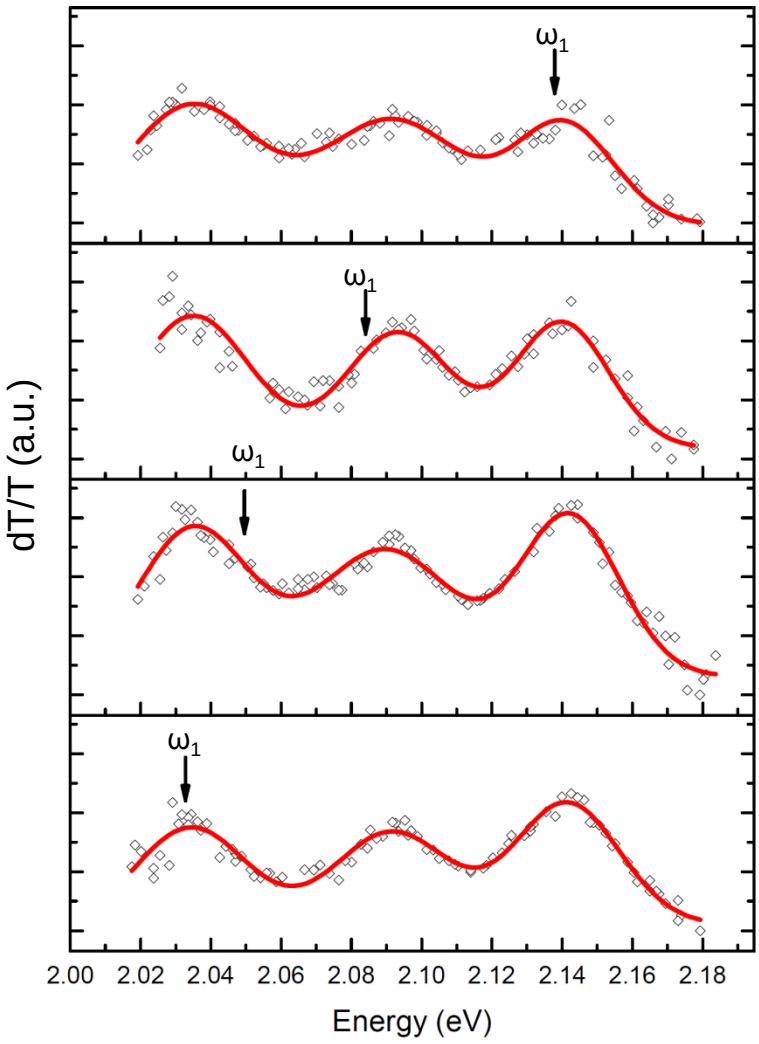

Figure 5.7: Non-degenerate differential transmission. The energy of the non-scanning laser is identified by the arrow. The results show the non-degenerate spectrum is independent of the energy of the non-scanning laser. Each scan is normalized, however the scales are the same in each scan.

In the presence of inhomogeneous broadening of resonant systems, it is known from a previous chapter that the spectral response, given by the third order nonlinear susceptibility above, exhibits spectral hole burning where the spectral hole width is the homogeneous width (T_2^{-1}) [30]. However, the data in Fig. 5.7 shows no evidence of spectral hole burning. The widths of the resonant features are comparable to those reported in quantum well structures in the time domain, corresponding to time scales of order ∼100 fs [100], a result they attribute to disorder induced dephasing [173].

However, given the evident role of screening of the internal fields (see discussion below), hole burning would not be evident in 3rd order spectroscopy since the same field screening would appear in all the structures and uniformly affect all the resonances, not just the resonance excited by the non-scanning field. A higher order technique would be required.

However, a high resolution scan does reveal an ultra-narrow resonance as seen in Fig. 5.8. This structure, obtained following the methods in Ref. [8], is observed throughout the response shown in Fig. 5.8 and at every arrow location in Fig. 5.8. To summarize from Ref. [8], ultranarrow resonances can be observed by varying the relative driving frequencies of two AOMs. The resonance arises from coherent mixing of the ω_1 and ω_2 fields leading population pulsations, however the linewidth (FWHM $\sim$110 kHz) is significantly more narrow than what we may expect from lifetimes measured in this system using time-resolved PL even in the presence of a strain field.

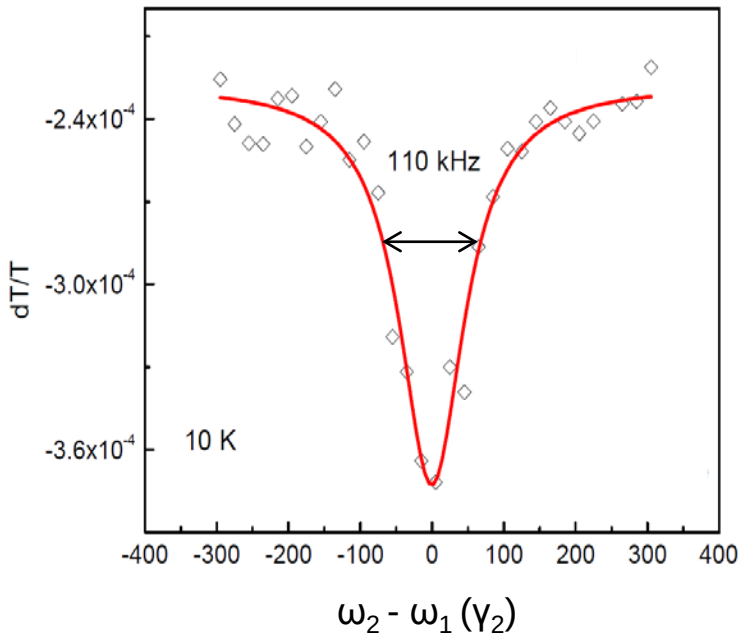

Figure 5.8: Coherent population pulsation component of nondegenerate nonlinear spectrum taken using the methods of ref. [8] with negative background included.

The presence of an ultranarrow resonance in the system implies that the decay dynamics of the nonlinear signal are determined by a metastable state in the sys-

tem, as first predicted by Lamb [156] and shown in chapter 3. The width (FWHM ∼110kHz) corresponds to the relaxation time of the state of order 2.9 μs. The narrow feature is expected from theory except the theory for a normal resonant system shows the resonance is positive, not negative. The resonance is negative here because it is dominated by the negative offset. Such a long time scale is inconsistent with excitonic lifetimes measured in this system using time-resolved PL even in the presence of a strain field [7, 12]. It is more likely due to the presence of traps, for example a trap state formed by a misorientation defect formed due to the coalescence of nanowires [164, 165].

Using phase modulation techniques, it was shown in chapter 4 how the presence of long-lived states can be detected and how to obtain a measurement of the lifetimes of the long-lived states in the system by comparing the in-phase and out-of-phase components measured in the nonlinear signal by a lock-in amplifier. The nonlinear response in this sample shows a significant out of phase component for $\sim 10kHz$ modulation frequencies of either ω_1 or ω_2. Using phase modulation techniques, we measure that decay rate of the nonlinear signal in the same sample location as the data in Fig. 5.8 is 2.56 μs, in good agreement with the value obtained from the ultranarrow resonance.

5.3.1 Arrhenius plot

In this section some of the temperature-dependent properties of the slow decay in the nonlinear signal will be examined. As stated, we attribute the slow decay to metastable trap states in the system. The occupation probability of trap or defect state is heavily influenced by temperature, since at higher temperature the thermal energy in the system can promote it into the conduction band (for donor-type defects) or the valence band (for acceptor-type defects). From Shockley-Read-Hall statistics the trap emission rate e_n for a donor-type defect is proportional to

$$e_n(E_t) \propto f(E_t) \approx e^{-\frac{E_c - E_t}{k_B T}}, \tag{5.1}$$

where $f(E)$ is the occupation probability of a state at energy E, E_c is the conduction

band energy and E_t is the trap energy [174].

Indeed, a measurement of the relaxation rate as a function of inverse temperature is linear on the standard Arrhenius plot, yielding activation energies of 5-12 meV in the samples studied, as shown in Fig. 5.9. The decay times in the Arrhenius plot in Fig. 5.9 was measured using phase modulation techniques. To perform the phase modulation measurement, a $\lambda = 405$ nm beam was used to modulate the absorption of a second beam (ω_2) at $\omega = 2.01$ eV. The activation energies were measured over several different regions of the sample, spaced by $\sim$100 μm (black, blue and red data points in Fig. 5.9). Similar to the temperature-dependent modulated absorption measurements, the limited resolution of the confocal microscope set-up implies that the exact group of excitons may not be measured at each temperature for a specific data set. Metastable traps with similar lifetimes were reported in yellow emitting InGaN quantum wells [175] and attributed to states formed at the boundaries of InGaN clusters, however we mainly attribute the traps to coalescent defects, as mentioned earlier.

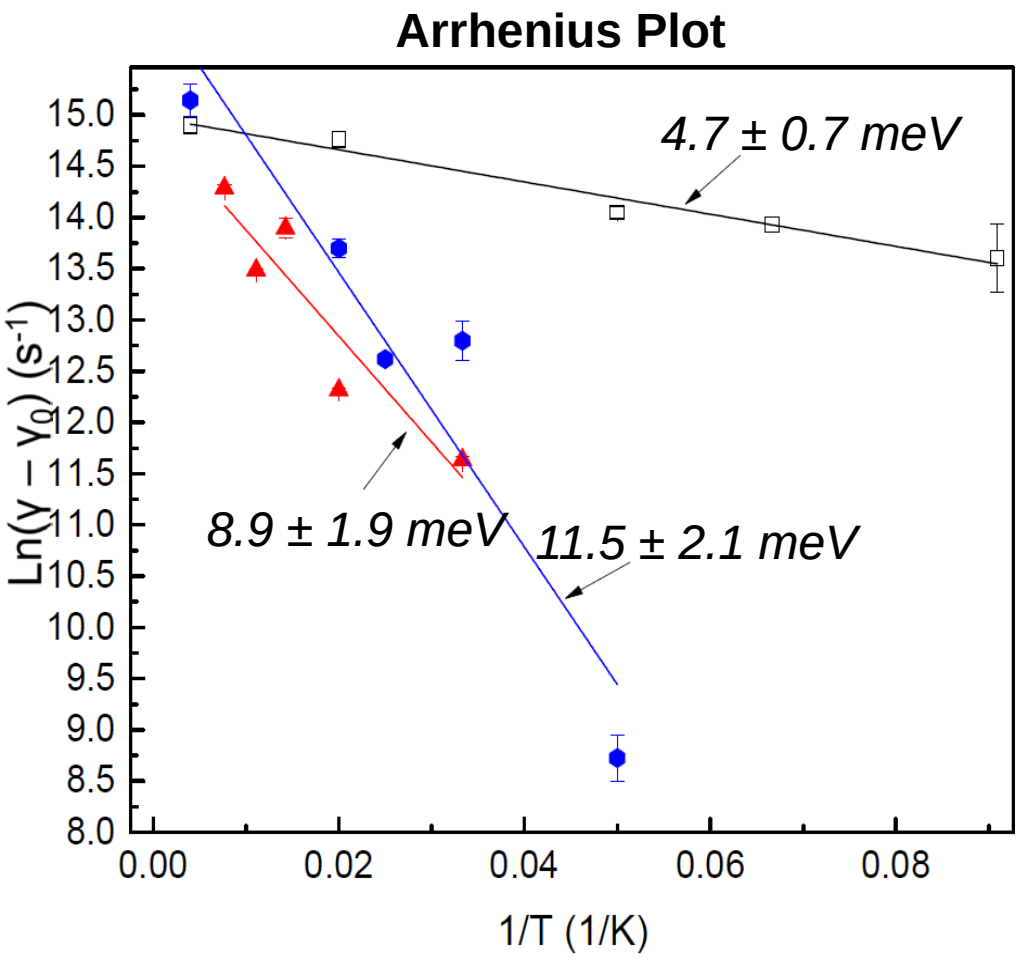

Figure 5.9: Arrhenius plots taken at different regions of the sample, represented by the different colors in the plot. Each data point was taken by averaging over several measurements from the lock-in amplifier. The error bars are from the error in the mean of the measurement.

5.4 Model and Dicussion

In order to understand the data, we consider a phenomenological model in Fig. 5.10 where non-radiative electron traps are localted in the region adjacent to the dot. The specific observations we address are: 1. the exponential dependence of the PLE signal, 2. the positive dT/T resonant structures within the modulated absorption and non degenerate dT/T and 3. the constant negative dT/T offset observed in the modulated absorption and non degenerate dT/T.

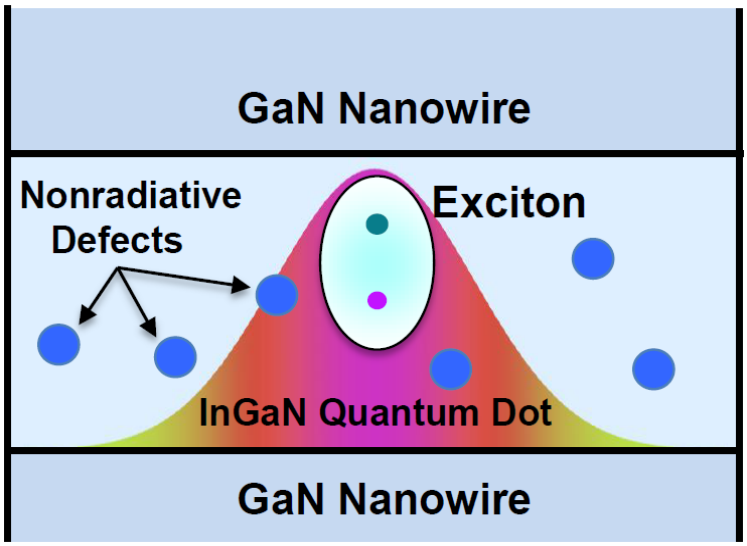

Figure 5.10: 2-D cross-section of DINW. A gradient in the InN concentration is also shown due to strain effects in the system [9] (magenta is the highest concentration, with blue/yellow the lowest).

The reduced absorption associated with the excitonic structures in more conventional III-As quantum dots is due to saturation of the absorption arising from decreasing the population in the ground state and increasing the population in the excitonic state, a simple result of the optical Bloch equations. However, this explanation would show the nondegenerate response is strongly dependent on the frequency of the nonscanning beam, contrary to the data in Fig. 5.7. Both Λ and V systems mentioned earlier would also give strong dependence of the spectra on the nonscanning beam as would simple energy transfer.

An alternate explanation for the positive dT/T resonances is again associated with disorder. The DINW structures are known to have a compact quantum dot at the center as evidenced in (PL) and transmission electron microscopy (TEM)

studies [9, 12, 123]. Isolated DINWs from similar samples show clear evidence of single photon emission [12] from second order correlation measurements, the result of Coulomb blocking of additional excitons in the dot, something that does not occur in higher dimensional systems. The disordered states in the surrounding material can be optically excited and are the origin of the exponentially increasing featureless PLE shown previously. After excitation into the disordered states, carriers can be captured by the metastable trap states (Fig. 5.11). It has been shown that charges that occupy charge trap states in close vicinity to quantum confined excitons in semiconductor nanostructures can decrease the oscillator strength of the lowest exciton transition when the exciton hole wavefunction becomes localized in the vicinity of the trap electron due to the large hole effective mass compared to the electron effective mass [176, 177]. The quantum dot exciton states may be especially susceptible to this type of interaction, as it is known from nano-cathodoluminescence measurements that the largest concentration of nonradiative localized states (e.g. traps) occurs at the bottom of the DINW in the same vicinity as the hole wave function [9].

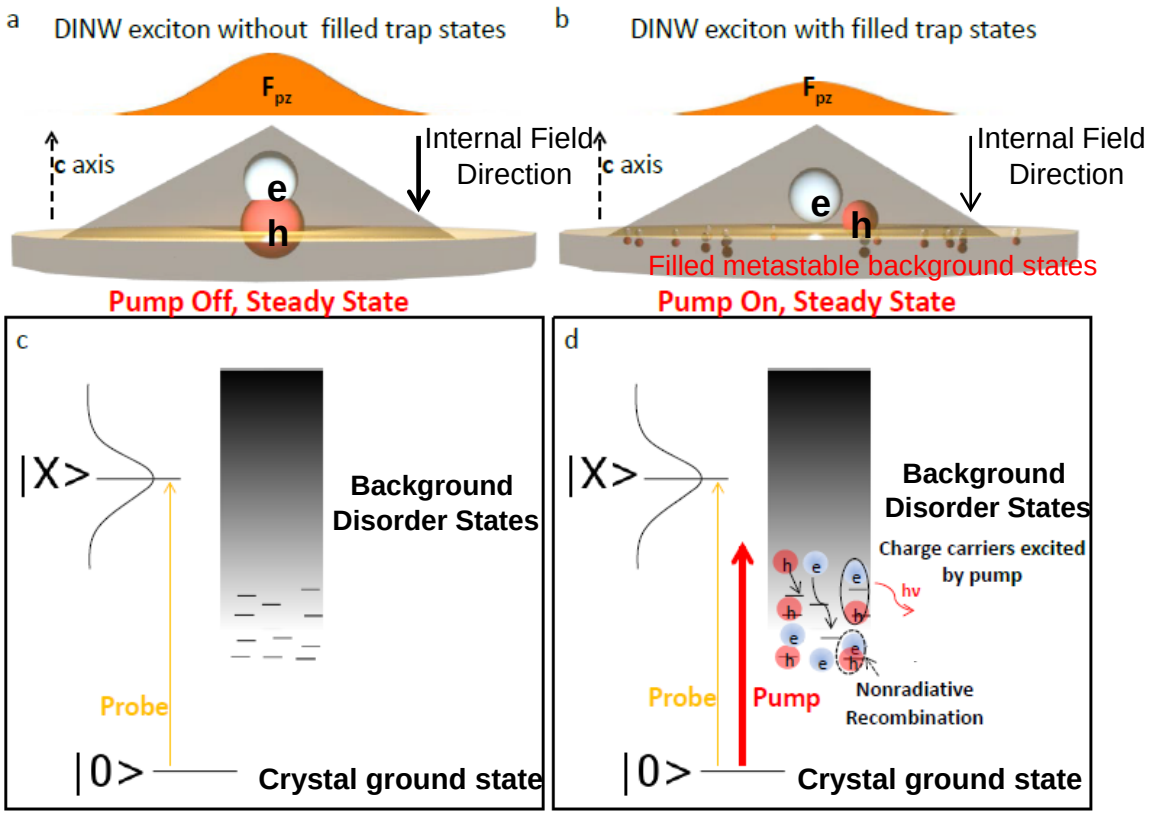

Figure 5.11: **(*a.*)** 3-D schematic of DINW with the exciton electron wavefunction (white sphere inside the DINW pyramid) and hole wavefunction (red sphere inside DINW pyramid). The pyramid represents the Volmer-Weber quantum dot that can form in the center of the DINW [10]. The strength of the piezoelectric field is shown by the orange plot and pointed in the opposite direction to the c-axis (dashed arrow) where the electron and hole are separated along this axis due to this piezoelectric field. **(*b.*)** 3-D schematic of the DINW showing the effect of the filled trap states (electron and hole represented by smaller white and red sphere, illustrating the higher degree of localization for these states). **(*c.*)** Energy level diagram of the single DINW showing the exciton state ($|X\rangle$) along with the continuum of background states formed by disorder and charge trap states. **(*d.*)** Energy level diagram including the effect of the pump beam which is tuned to lower energy than the exciton resonance.

Alternatively, excitation of the defect states could result in charge transfer from the valence band in the quantum dot state to a lower lying defect state. This would mean the quantum dot could no longer undergo a transition to the (neutral) exciton state, i.e., the absorption would be reduced.

A constant negative dT/T offset in all of the data has been subtracted to em-

phasize the excitonic response. The negative offset (optically induced increase in absorption) is comparable, though not correlated, in magnitude to the positive response (reduced absorption) of the excitons. We tentatively associate the increase in absorption to either an increase in the oscillator strength of the background disorder in these systems that gives rise to the PLE and/or to a red shift in the PLE response. The origin of either effect is likely due to screening of the internal electric field by the trapped carriers excited by the optical field (Fig. 5.11). This type of effect could lead to a negative dT/T offset, but we are currently unsure of why the offset is a constant signal. Further investigation will be needed to understand this effect.

5.5 Chapter summary

In summary, this chapter featured a study of the coherent nonlinear optical properties of an ensemble of self-assembled InGaN DINWs. This study shows that as expected there are strong excitonic resonances in InGaN DINWs arising from the strain induced dots at the center, however, these resonances are obscured in the PLE and PL by the dominant role of traps and defects, likely formed due to nanowire coalescence. The nonlinear optical behavior of the excitons shows no evidence of manybody physics typical of larger or higher dimensional systems and, hence, may be promising for future photonic applications if the contribution of the non-resonant background can be reduced.

CHAPTER 6

Luminescence and energy transfer effects in selective area disk-in-nanowire samples

The data and analysis presented in this chapter focuses on optical measurements for the characterization of selective area grown InGaN disks-in-GaN nanowires (DINWs). The aim of the chapter is to provide some preliminary data that can be used to better understand selective-area samples for coherent nonlinear optical measurements featured in the next chapter. Unlike in the self-assembled DINW sample featured in the last chapter, the selective area sample utilizes a high degree of growth control over the morphological properties of the GaN nanowires such as diameter and growth position. As a result of the increased level of growth control, the selective area sample does not exhibit effects related to nanowire coalescence such as emission quenching due to defects. The nonlinear optical spectrum of the selective area sample also does not exhibit long-lived decays due to metastable trap states that were thought to be associated with coalescence.

In this chapter we present a series of linear and nonlinear optical measurements at low temperature (10 K) on an ensemble of red-emitting, selective area InGaN DINWs. The specific linear optical measurements are sample photoluminescence and photoluminescence excitation. The nonlinear optical measurements are nondegenerate and degenerate nonlinear absorption to probe energy transfer in the system. We find that the optical dynamics are largely driven by effects related to background disorder states. Specifically, we find that energy/charge transfer processes of optically excited electron-hole pairs from higher to lower states is dominated by transfer from

higher energy background disorder states to lower energy background disorder states or quantum confined excitons. We propose that energy transfer from disorder states to excitons along with disorder state filling lead to sharp blueshifts in the intensity-dependent PL spectrum, assuming that most of the sample emission originates from the excitons. Support for this assumption will be given in a later section. It is important to reiterate that energy transfer effects observed in the nonlinear optical spectrum are not visible in the self assembled sample because the nonlinear optical response of the self-assembled sample is almost entirely due to effects from metastable trap states.

6.1 Selective-area growth of GaN nanowires with InGaN disks

Before a presentation of the data in this chapter, some of the specific growth techniques for the selective area samples featured in this chapter and the next are described. To achieve a high uniformity of nanowire morphology, the InGaN disk-in-nanowires can be grown on a pre-patterned substrate. Small nanoapertures can be patterned onto metal masks that are sputtered on top of the substrate, leaving small areas of substrate exposed. Spatially controlled growth of the nanowires can then be achieved as the mask limits the growth of the nanowires only through the nanoapertures. In the samples studied in this chapter and the next, the Ti mask is deposited on top of a layer of (0 0 0 1) GaN that is grown coherently on top of a layer of sapphire. The GaN layer is around 5 μm thick and the sapphire is about 500 μm thick. A scanning electron microscopy (SEM) image and a schematic of the selective-area grown sample featured in this work in shown in fig. 6.1. More detailed descriptions of the selective area growth process can be found in Refs. [114, 167].

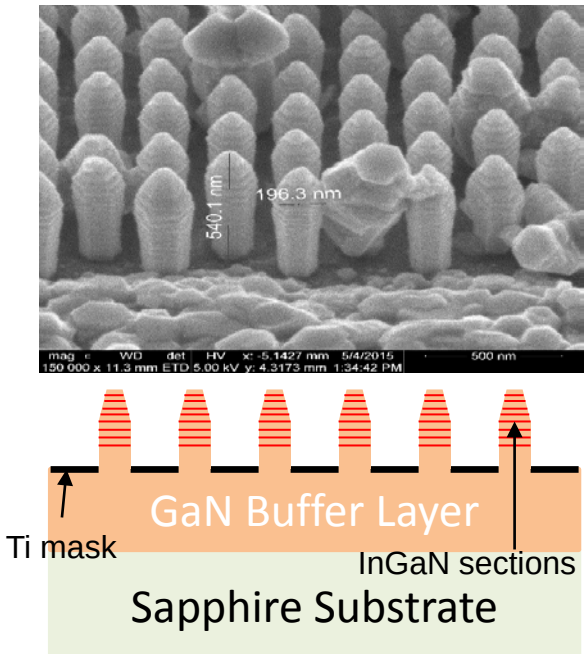

Figure 6.1: Top: SEM image of the selective area sample featured in this chapter. Bottom: cross-section of the selective area sample along the nanowire growth direction

The sample featured in this work contains an ensemble of nanowires where 8 InGaN disks are grown in each GaN nanowire. The disks are 3 nm thick and separated by 3 nm of GaN. The relative spacing of the nanowires across the sample surface is $\sim$ 200 nm. The nanowires have a tapered end structure so that several disks near the tip of the nanowire have varying diameters, where the change in diameter ΔD $\sim$10 nm between each disk along the growth direction. The tapered structure is necessary to prevent nucelation of GaN around the mask apertures leading to undesired sizes of nanowires [114].

6.2 Experimental Results

For measuring PL and photoluminescence excitation (PLE), the sample is excited in a reflection geometry by a continuous-wave $\lambda = 405$ nm diode laser for PL and a continuous-wave tunable dye laser for PLE. The excitation lasers are focused onto the sample using the NA = 0.55 microscope objective that was mentioned in chapter

4, giving a spot size $\sim$1 μm^2. Within the focal spot, $\sim$200 DINWs are probed at once. The PL and PLE spectra were collected using a nitrogen-cooled CCD camera and has been corrected for the wavelength-dependent responsivity of the silicon CCD. Each PLE data point was collected by integrating the total luminescence counts over 1 second from λ = 670-700 nm using the CCD.

The PL spectrum is shown for several different intensities in Fig. 6.2a. As a function of excitation intensity, the spectrum shows a pronounced blueshift. Furthermore, the spectra appear to be composed of multiple resonances as highlighted in the high intensity data in Fig. 6.2a. A plot of the energy corresponding to the peak PL emission as a function of excitation intensity is shown in Fig. 6.2b. We observe that the peak PL emission energy is relatively constant over some range of excitation intensity values, then sharply blueshifts, then is relatively constant again, resulting in a "stair-case" shaped plot. Intensity-dependent blueshifts in the PL spectrum are common for InGaN nanostructures and heterostructures due to internal electric field screening [84, 178] and disorder state filling [89] effects, however both of these effects do not exhibit the "stair-case behavior" observed in Fig. 6.2b. The physical origin for the "stair-case" behavior will be discussed in a later seciton. In Fig. 6.2c, we plot the maximum PL counts as a function of excitation intensity. This data shows: 1. a saturation behavior at high excitation intensity, characteristic of excitonic emission and 2. a superlinear increase in PL emission as a function of excitation intensity ($I_{PL} \sim I_{exc}^{1.25}$). The superlinear increase in PL emission is not characteristic of biexcitons, where the intensity of the PL emission scales like the square of the excitation intensity. It is possible that the superlinear increase in PL intensity is a result of multiple emitting states.

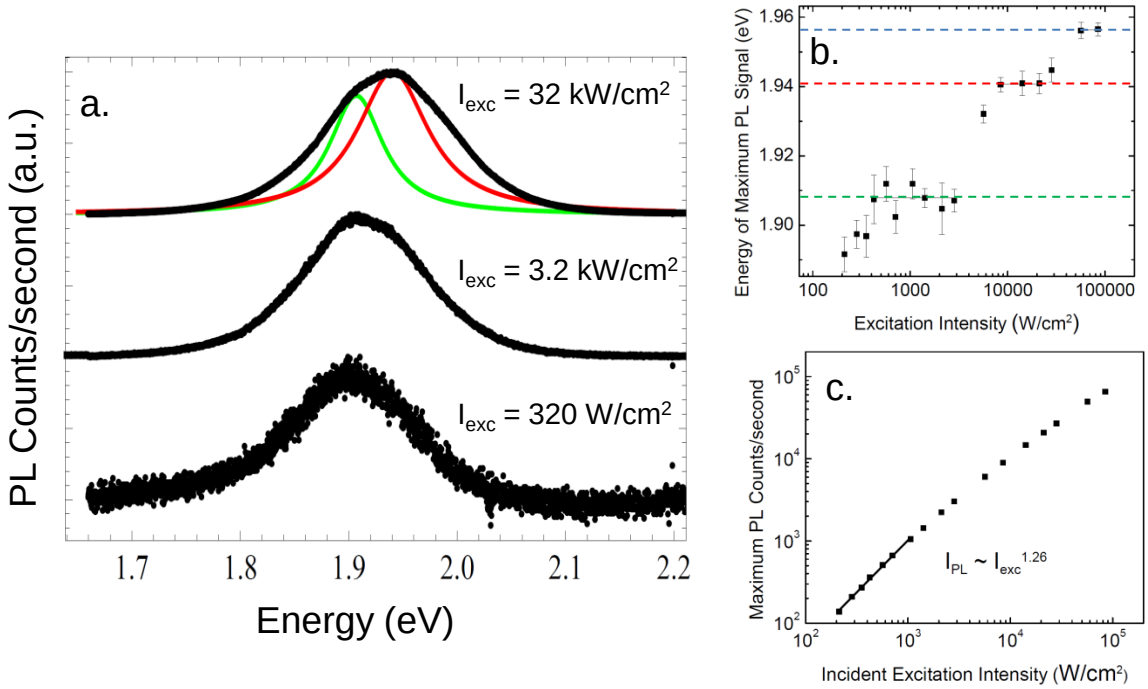

Figure 6.2: ***a.*** Photoluminescence spectrum of the sample taken at 10 K for three different orders of magnitude in excitation intensity. As a guide to the eye, the spectral location of some resonances within the spectrum is highlighted in the high intensity data. Note that the resonances are not fit to the data and only represent an estimate of resonances that compose the spectrum. ***b.*** Energy of the maximum PL emission signal vs. the PL excitation intensity. The colored flat lines show regions where the PL signal is relatively independent of excitation intensity. ***c.*** Maxmimum PL signal vs. excitation intensity.

The PLE data is shown by the green points in Fig. 6.3, where the green line provides a guide to the eye. One striking feature about the data is that the PLE shows an essentially featureless, monotonically increasing signal as a function of energy while the PL is dominated by resonant behavior, similar to what was observed in the self-assembled sample. The relatively featureless, increasing spectrum as a function of energy is a common signature of disorder in the system, similar to the Urbach

tail [98], as mentioned in an earlier chapter.

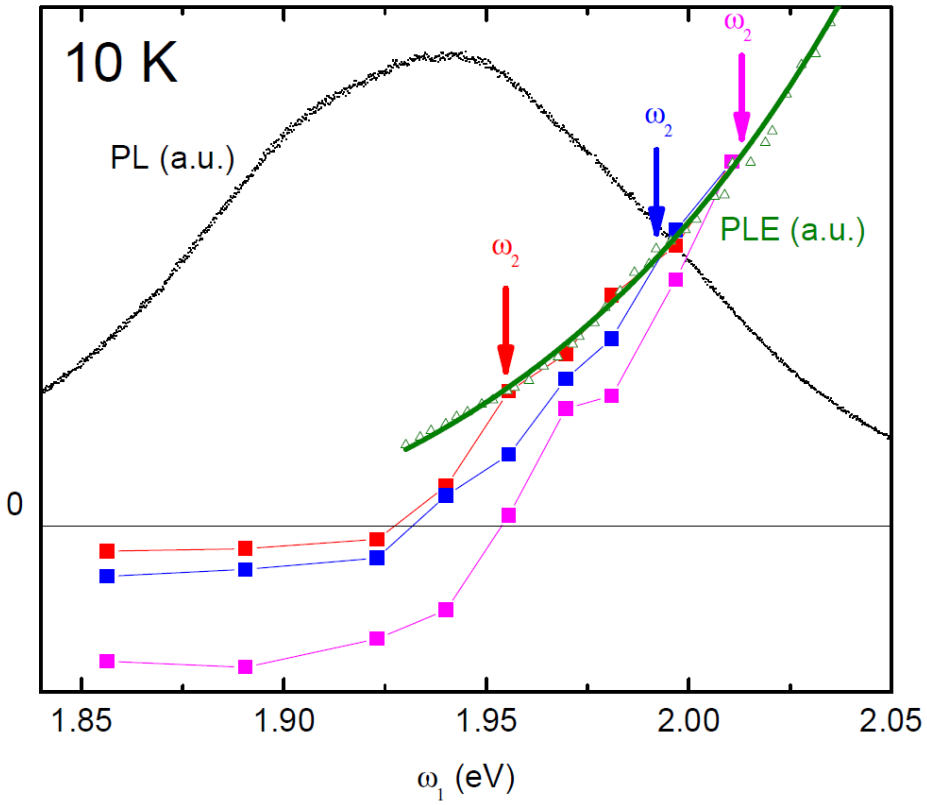

Figure 6.3: PLE (blue points and line) shown with PL (black points) and several nondegnerate nonlinear absorption spectra as a function of ω_1 for a fixed ω_2, given by the colored arrows. The color of each ω_1 scan corresponds to each colored arrow. The black horizontal line shows zero signal for all data sets.

The nondegenerate nonlinear absorption data shown in Fig. 6.3 spectrum is taken

by fixing the detected ω_2 beam near the PL resonance and scanning the ω_1 beam over the resonance. The nonlinear signal is detected along the ω_2 direction using phase-sensitive detection as described in chapter 4. This is the sort of beam configuration that is normally used for probing energy transfer, as discussed in section 3.3. We verify that the nonlinear optical signal is in the $\chi^{(3)}$ limit by observing the power dependence of the signal. As discussed in a previous chapter, the lowest order contribution to the dT/T signal is $\propto |E_1|^2|E_2|^2$, therefore for a fixed ω_2 power, the nonlinear signal should be linear in the ω_1 power. In Fig. 6.4, the nonlinear optical signal for a fixed ω_2 power is presented as a function of ω_1 power. We observe that the nonlinear signal is linear as a function of excitation power up to an ω_1 power of $\sim$ 300 μW, where the signal begins to saturate due to higher order terms in the nonlinear response. The linear region of this plot represents the excitation powers where the nonlinear signal is in the $\chi^{(3)}$ limit. To remain in the $\chi^{(3)}$ limit, the ω_1 beam power is kept at $\sim$ 200 μW and the ω_2 power is fixed at 100 μW.

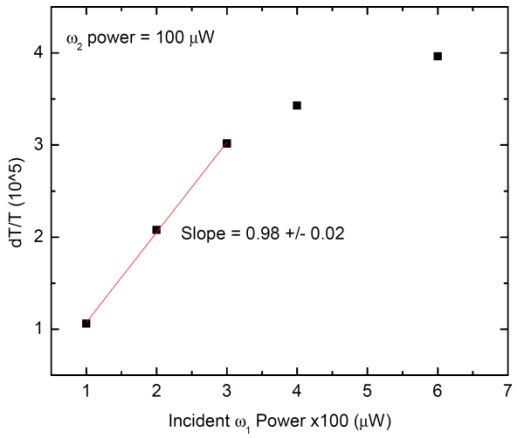

Figure 6.4: Nonlinear optical signal measured along the ω_2 direction as a function of ω_1 power.

We find that the ω_2 beam absorption saturation due to the presence of ω_1 (positive dT/T) increases as a function of energy for $\omega_1 \geq \omega_2$ and follows a qualitatively similar dependence on energy as the PLE spectrum. For $\omega_1 < \omega_2$, the NDdT signal decreases more rapidly than the PLE signal and has an additional negative dT/T offset once

the ω_1 beam is sufficiently detuned from the exciton transition. The magnitude of the negative dT/T offset increases as a function of ω_2. The physical origin of the negative dT/T offset will be discussed further in later sections. In the measurement shown in Fig. 6.3 the ω_1 - ω_2 detuning is generally not small enough to observe narrow coherent population pulsation resonances, which are expected to be $\sim$ GHz based on time-resolved PL data of similar samples [55]. The nature of coherent population pulsation resonances will be explored in the next chapter.

6.3 Discussion

Our understanding of the data and the physical models outlined in this section are centered on the coexistence of states formed by material disorder and quantum confined exciton states within the DINWs. Physically, the disorder states can be atomistic defects such as In-N-In chains as discussed in section 2.5, and the exciton is the quantum-confined single electron-hole pair state that can exist in the center of the DINW that was described in section 2.6. In principle, both the disorder states and the quantum confined excitons can contribute to the sample emission. Studies in similarly grown samples have shown evidence of single photon emission can be observed from single DINWs [12,120,168], which suggests that the excitons on average provide a larger contribution to the sample emission compared to disorder states. The degree to which the disorder states contribute to the sample emission compared to the exciton states is currently unknown in this system and should be the subject of further investigation.

The PLE spectrum of InGaN/GaN heterostructures is typically dominated by the large density of DS, therefore it is usually difficult to measure absorption features from excitons in linear absorption [100]. On the other hand, it has been found that the resonant nonlinear absorption of InGaN/GaN structures resulting in a positive dT/T signal is very sensitive to signals from excitons, with virtually no contribution from the DS [100]. We therefore tentatively attribute the positive dT/T nonlinear ($\chi^{(3)}$) absorption signal in the spectrum of Fig. **??** to saturation of the absorption of

ω_2 due to state-filling processes of excitons.

We observed that the positive dT/T signal in Fig. 6.3 qualitatively follows the energy dependence of the PLE spectrum when $\omega_2 < \omega_1$, which supports the idea that population from the DS is transferred to lower energy excitons resulting in a state filling of the exciton (saturation of exciton absorption). Energy transfer from the localized DS to the localized energy state representing the occupation of the exciton in the center of the DINW (and vice versa) can occur from several different mechanisms. Electrons and holes confined to nano-scale regions formed by disorder can emit phonons to directly hop from the localized disorder site to a different nano-scale region [108, 154]. Furthermore, dipole-dipole coupling can contribute to long-range energy transfer, with or without the emission of a phonon [154]. It is also possible that energy/charge transfer from exciton excited states to lower energy states probed by ω_2 can contribute somewhat to the state-filling signal. This idea will be explored further below. When $\omega_2 > \omega_1$ the effects of population transfer from DS to excitons diminish rapidly (compared to the energy dependence of the density of DS) at low temperature, likely because tunneling processes involving phonon absorption are negligible at low temperature. Energy transfer between localized states was also observed in GaAs heterostructures at low temperatures and showed some similar qualitative behavior in the nonlinear spectrum [48].

As noted, it is possible that energy/charge transfer from exciton excited states or from electron-hole pairs in different DINWs can give rise to the type of signal observed in Fig. 6.3. In order to characterize this type of behavior, we perform several measurements at higher energy compared to the PL resonance, where we may expect to probe exciton excited states or excitons from different DINWs that emit/absorb at higher energy. In Fig. 6.5, the degenerate third order nonlinear signal $\chi^{(3)}(\omega_2 = \omega_1)$ (DdT) is presented along with the nondegenerate nonlinear absorption for a fixed ω_2 (scanning beam is ω_1 as in Fig. 6.3) and the PLE. The DdT signal is mostly positive, again indicating a state-filling type saturation of the excitons. It is found that the DdT signal shows several resonances and begins to decrease at higher energy (around $\omega = 2.18$ eV). The individual resonances in the DdT spectrum

could be from different groups of excitons or exciton excited states. The positive dT/T nondegenerate nonlinear signal in Fig. 6.5 mainly follows the PLE spectrum, similar to the data presented in Fig. 6.3. This indicates that the background DS are primarily responsible for the exciton state filling at lower energies, and not exciton excited states or different DINWs that would be probed in the DdT spectrum.

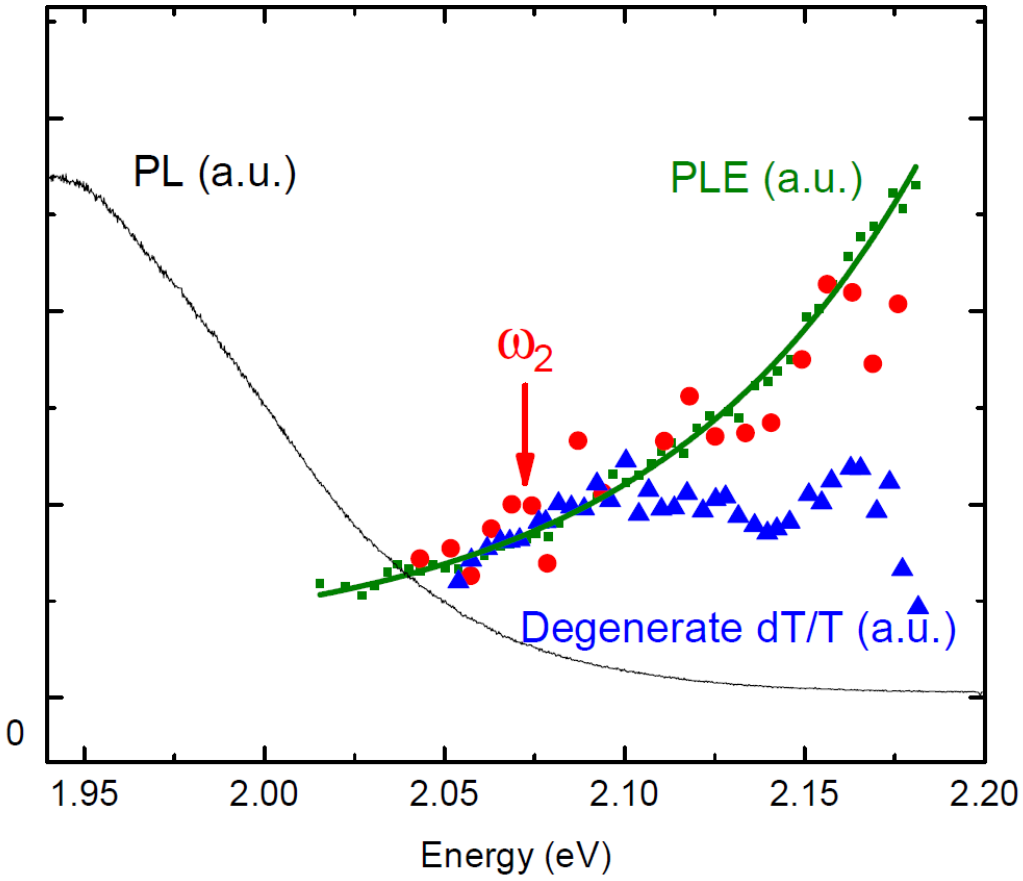

Figure 6.5: PLE (green points and line) shown with PL (black points), the degenerate nonlinear absorption (blue points) nondegnerate nonlinear absorption (red data points) as a function of ω_1 for a fixed ω_2, given by the red arrow. At higher energies, the non-degenerate dT/T spectrum follows the PLE, unlike the degenerate dT/T that begins to decrease in signal strength at higher energy.

When $\omega_2 >> \omega_1$, the dT/T signal in Fig. 6.3 shows a constant, negative offset that generally increases in magnitude as a function of ω_2. A negative dT/T offset, or an increase in ω_2 absorption due to the presence of ω_1, could be caused by an effect

related to screening of the internal piezoelectric field, perhaps by optically excited disorder states as noted in the previous chapter. A similar effect is observed in the self-assembled DINW samples featured in chapter 7 and will be discussed in more detail within that chapter.

To understand the intensity-dependent PL behavior, we consider a model in which energy transfer occurs between the DS and the excitons, as illustrated in Fig. 6.6. In our model we further assume that most of the sample emission from the DINWs comes from the excitons, although it is possible that some of the sample emission comes from the disorder states. As noted earlier, the intensity-dependent PL of disorder states generally shows a monotonic blueshift as a function of excitation intensity due to state-filling effects. On the other hand, it has been observed that the intensity-dependent PL of DINW excitons does not show a strong dependence on excitation intensity [27, 126]. Instead, the exciton emission from DINWs saturates without a significant blue shift and biexciton states begin to emerge in the spectrum, typically at higher energies [126]. Finally, our model incorporates the fact that the tapered nanowire design results in emission from groups of excitons with different diameters. The diameter of the DINW has a large influence on the emission energy of the exciton because the diameter affects the strain relaxation properties of the InGaN active region, leading to a blueshift in the emission energy for larger diameter DINWs.

To illustrate our physical model, we consider two different inhomogeneously broadened exciton states $|X1\rangle$ and $|X2\rangle$ from two different groups of DINWs, where the diameters of the DINWs in the group belonging to $|X1\rangle$ is different from the diameters of DINWs in the group belonging to $|X2\rangle$. The diameters of the DINWs within each group $|X1\rangle$ and $|X2\rangle$ are assumed to be roughly uniform. Generally we assume that the groups of DINWs represented by $|X1\rangle$ and $|X2\rangle$ are not coupled and the energy-dependent density of background DS is approximately the same in both groups. The decay rates from the DS into the excitons are given by Γ_{D1} and Γ_{D2}, respectively. Generally $\Gamma_{D2} > \Gamma_{D1}$ due to the higher density of disorder states at higher energy. The decay rates out of the excitons and into the disorder states are given by Γ_{1D} and Γ_{2D}, where $\Gamma_{1D} \approx \Gamma_{D1}$ and $\Gamma_{2D} \approx \Gamma_{D2}$. If we first consider

excitation of the sample by $\lambda_1 = 405$ nm used for PL, the disorder states in Fig. 6.6 will become filled as a function of excitation intensity up to energy levels denoted I_1 and I_2, corresponding to two different intensities I_1 and I_2 of ω_1. When the intensity of the ω_1 beam is I_1, the decay rate $\Gamma_{1D} \rightarrow 0$ due to the state filling of the DS, hence the emission of $|X1\rangle$ is enhanced compared to $|X2\rangle$ because the decay path into the DS is closed. When the intensity of the ω_1 reaches I_2, $\Gamma_{2D} \rightarrow 0$ and both of the decay channels from $|X1\rangle$ and $|X2\rangle$ into the DS are closed. The emission of $|X2\rangle$ is enhanced compared to $|X1\rangle$ because $\Gamma_{D2} > \Gamma_{D1}$ therefore more steady state population is accumulated in $|X2\rangle$. Hence, the emission enhancement of higher energy DS as a function of excitation intensity leads to a similar effect in the exciton emission energy. As noted, the excitons are not expected to show a significant energy shift as a function of excitation intensity. If we assume that most of the emission comes from the excitons, the behavior outlined above could potentially result reproduce the "stair-case" intensity-dependent PL data observed in Fig. 6.2b. The flat regions in the intensity-dependent PL data would correspond to the emission of a specific group of excitons and the sharp transitions correspond to excitation intensities in which the emission from a higher energy group becomes more dominant.

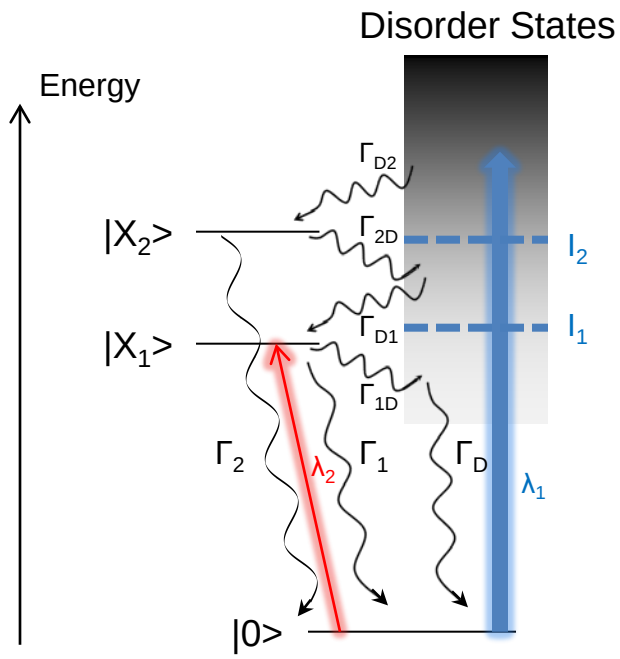

Figure 6.6: Energy level diagram of the DINW system. The states $|X1\rangle$ and $|X2\rangle$ represent two different groups of excitons from DINWs with very similar diameters, however the diameters of the two groups $|X1\rangle$ and $|X2\rangle$ are assumed to be different. Population excited into background disorder states is coupled to the excitons. The sample is excited by a λ = 405 nm beam (λ_1) and generally probed by a second beam (λ_2) for nonlinear measurements.

From the high resolution SEM image in Fig. 6.1, we estimate that the variation in diameter of successive DINWs near the tip of the nanowire is ∼10-20 nm from the tapered design of the sample. Zhang et al. performed a systematic study of the emission energy dependence of excitons in blue-emitting site-defined DINWs emitting and found that variations in the diameter of the DINWs caused a corresponding change in the emission energy of $\Delta E/\Delta D$ = -3.47 meV/nm [168]. It is likely that the magnitude of the emission energy shift as a function of diameter is even larger in red emitting samples due to the higher lattice mismatch between the InGaN and GaN layers that leads to more strain. At the same time, the shift also depends on the average diameter of the DINWs and the differential change in emission energy

is larger for smaller diameter DINWs. Assuming the model outlined above, we find that the diameter dependent emission energy in Zhang et al. is roughly consistent with the energy spacing of the emission energies observed in Fig. 6.2b (∼30-40 meV) based on the variation in the DINW diameter in the tapered design. It is possible that the resonances observed in Fig. 6.2a are from groups of excitons with different diameters, however the resonances are likely broadened by emission from other states such as background DS.

The intensity-dependent PL of self-assembled samples for two different orders of magnitude in excitation intensity is shown in Appendix B. Unlike in the selective area samples, there is no significant shifting of the PL emission. In fact, it is possible that there is a slight red shift of the higher intensity PL compared to the lower intensity PL. A physical understanding of this effect, perhaps incorporating the metastable trap states, is still being developed. It is also possible that this is related to the fact that the self-assembled DINWs have smaller diameters compared to the selective area samples, so energy transfer effects from the DS are diminished.

6.4 Summary

In summary, in this chapter we have presented a low temperature study on the linear and nonlinear optical properties of InGaN disks in nanowires, focusing particularly on the role of disorder states in the sample. Some aspects of the growth techniques of DINW samples were also mentioned. This work gives strong evidence that population in localized disorder states is transferred into lower energy quantum confined excitons. Assuming that the exciton states are responsible for most of the sample emission, this behavior along with intensity-dependent background DS filling can be used to explain the unusual "stair-case" intensity-dependent PL spectrum observed in Fig. 6.2b. It is possible that this type of relaxation can enhance the radiative efficiency of excitons in the DINWs, similar to the emission enhancement expected from population transfer between defects and quantum confined excitons [179].

CHAPTER 7

Coherent nonlinear optical spectroscopy of selective-area InGaN DINW samples

In this chapter, the coherent nonlinear optical spectrum in the selective area DINW ensemble system will be presented. In the previous chapter, the nonlinear optical spectrum was used along with the intensity-dependent PL to show energy transfer effects between background disorder states and excitons in the system. To show this effect, the nonlinear optical spectrum was measured by fixing ω_2 and scanning ω_1 while detecting the ω_2 beam. In this section, we will discuss the nonlinear optical spectrum that is obtained by fixing ω_1 and scanning/detecting ω_2, which is the more traditional experimental set up for measurements such as spectral hole burning discussed in chapter 3. In effect, this chapter is about nonlinear absorption spectrum while the previous chapter was about nonlinear excitation spectrum.

For an ensemble of isolated discrete-level quantum systems, recall that there are generally two resonances in the third order nonlinear optical response that both track with the ω_1 frequency. The first resonance, known as the hole burning resonance, has a FWHM $\sim$ the dipole dephasing rate γ. The second resonance, known as the population pulsation, is generally much more narrow than the hole burning term and has a FWHM $\sim$ the excited state decay rate γ_2. Again, the power of the nonlinear absorption measurement comes from the fact that the decay times and dephasing rates can be extracted from individual subgroups of quantum dots probed by ω_1 that compose the overall inhomogeneous distribution and may have different dynamics at different energies.

It was found in chapter 5 that the coherent nonlinear optical signal from self-assembled DINW structures grown on silicon was dominated by effects related to metastable trap states. Filled trap states were thought to simultaneously screen the internal piezoelectric field leading to a negative dT/T signal associated with background disorder states and to decrease the oscillator strength of exciton transitions in the sample giving a positive dT/T signal. There was no evidence of spectral hole burning in the sample because the effects of the filled trap states affected all excitons and disorder states within the measurement field of view simultaneously. Furthermore, the population pulsation spectra were dominated by trap-related ultranarrow resonances that occurred at all probed energies. Unlike in the self-assembled DINW sample featured in chapter 5, the selective area DINW sample featured in this chapter does not show evidence of the effects of metastable trap states in the nonlinear absorption spectrum such as a slow decay in the nonlinear signal within our measurement sensitivity. It is therefore possible to observe effects such as spectral hole burning resonances in the nonlinear absorption spectrum.

We indeed find possible evidence of spectral holes in the nonlinear optical response of the selective area sample in the data reported in this chapter, however the spectral holes appear to be very broad, likely due to a fast dephasing process in the system. Furthermore, as one might expect from the previous chapter, we find that the physical picture of selective area DINW ensembles deviates from the relatively simple inhomogeneously broadened discrete-level system response expected in an ensemble of non-interacting quantum dots such as in III-As systems largely due to the background disorder states present in the DINW. We believe that the presence of the disorder states leads to behavior such as negative dT/T signals for large ω_1 - ω_2 detuning that was also observed in chapter 6. In addition to the possibly broad hole burning resonances, we observe narrow ($\sim \mu$eV) population pulsation resonances on top of the spectral hole burning response. The population pulsation resonances demonstrate decoherence-induced extra resonances, a phenomenon discussed in section 3.2.2.1, due to the large dephasing rates in the system. Generally, the width of the population pulsation resonance does not change significantly at room tempera-

ture compared to cryogenic temperatures. Exact comparison is difficult because the sample moves as a function of temperature and we do see variations (less than a factor of 2) as a function of position. This shows that both the dephasing mechanisms and the exciton lifetime do not seem to have a significant dependence on temperature, an exciting result for room temperature quantum photonics applications.

7.1 Preliminary data: Modulated Absorption

In order to gain an initial understanding of the system, we perform an optical modulation spectroscopy measurement. In this case, the ω_1 beam is replaced by a $\lambda = 405$ nm beam, while ω_2 is scanned over any resonances in the system, identical to the set up in chapter 5. Modulation of the 405 nm beam is used to detect the modulation in the transmitted probe beam using phase sensitive detection and a lock-in amplifier, as described in chapter 4 and 5. In a modulated absorption measurement of quantum dot systems, the higher energy ω_1 beam excites a population of electron-hole pairs in the continuum energy levels that rapidly decay to the lowest energy states [180]. In the absence of effects such as inter-dot frequency shifts, the ω_2 dT/T signal will be dominated by absorption saturation of the lowest energy exciton states (i.e. the lowest energy states that are populated by optically excited electron hole pairs) [180]. For an inhomogeneously broadened system, this is typically a positive dT/T Gaussian resonance (reflecting a pump-induced saturation/reduction in absorption), where the width gives the inhomogeneous bandwidth.

The modulated absorption of the selective area sample is shown at room temperature (top panel) and 10 K (bottom panel) in Fig. 7.1 along with PL data from the previous chapter. The modulated absorption at 10 K and room temperature as well as the two PL spectra were all taken at different sample regions, therefore it is important to note that the spectra may shift because of heterogeneity across the sample surface. As a rough approximation, the modulated absorption spectra in Fig. 7.1 is fit to a Gaussian distribution. Clearly, using a smooth Gaussian distribution to describe the spectrum is only an approximation since there are resonant struc-

ture within the Gaussian. It is possible that the resonant structures are from groups of excitons within disks of very similar geometries and InN concentrations and the spacing of the resonances is caused by the variation in diameters of the DINWs due to the tapered design of the sample. On the other hand, because of the 5 μm GaN layer in the sample, Fabry-Perot resonances could be a concern, assuming the index of refraction of GaN = 2.32 at 10 K [170]. The modulated absorption dT/T signal is positive throughout the spectrum, which indicates that the origin of the optical nonlinearity is state filling of excitons due to the presence of ω_1 that saturates the ω_2 beam. Furthermore, the phase-sensitive nonlinear signal shows no evidence of an out-of-phase component that was observed in chapter 5 and indicates a slow decay of the nonlinear signal. Many-body effects such as excitation-induced dephasing [129] do not appear to be significant. Finally, we note that the peak of the modulated absorption distribution is blue shifted compared to the peak of the PL resonance. The origin for this effect is still being investigated.

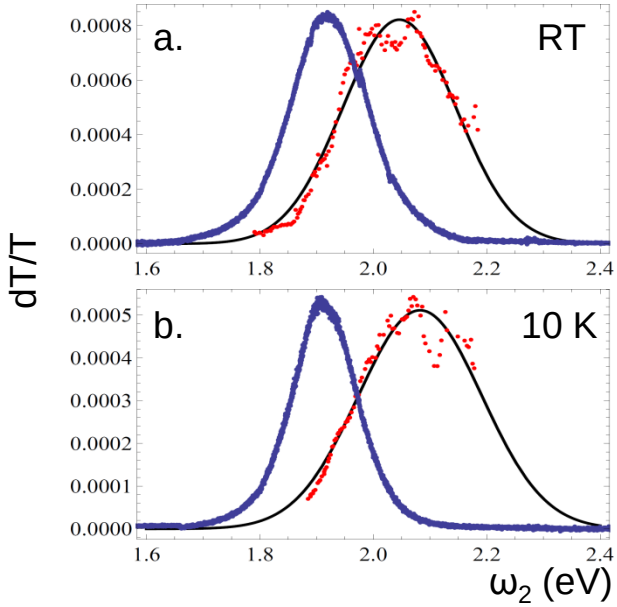

Figure 7.1: Modulated absorption and photoluminescence at 10 K (top panel) and room temperature (bottom panel) The PL excitation power was 100 μW in each spectrum. In each modulated absorption measurement the $\lambda = 405$ nm beam was fixed at 100 μW, while the resonant ω_2 beam was maintained at 100 μW. The modulated absorption data is fit to a Gaussian distribution (black line).

It is interesting to note that the modulated absorption signal level is generally much higher in the self-assembled samples featured in chapter 5. The filled metastable trap states appear to be much more effective at inducing optical absorption nonlinearities compared to the state filling nonlinearity described above.

7.2 Coherent nonlinear optical spectrum: hole burning reponse data

The analysis of the third order coherent nonlinear absorption spectrum is divided into two sections: one section that addresses the possible hole burning response and one section that covers the population pulsation response. The reason for this division is because the energy scales involved in both measurements are so different and the

physics giving rise to the resonances is quite different. As stated, measuring the hole burning resonances involves ω_1 - ω_2 detuning of 10s of meV while the population pulsation resonances are $\sim \mu$eV. The population pulsation resonances are therefore too narrow to resolve on the same scale as the hole burning features. Similarly, during the discussion of the population pulsation resonances, the contribution from the hole burning terms is usually treated as a constant offset. This section presents the hole burning data at both room temperature and low temperature. A discussion and comparison of the data at the two temperatures is presented in the next section. As in the previous chapter, it is verified that the coherent nonlinear optical signal is in the $\chi^{(3)}$ limit by carefully checking that the signal is linear in the ω_1 and ω_2 intensities.

The room temperature hole burning data is presented in Fig. 7.2 for several different ω_1 values shown by the colored arrows. Each data set has been smoothed using an 8 point moving window average. The spectra were taken at a slightly different sample locations compared to the modulated absorption spectrum shown in Fig. 7.1, therefore the hole burning response may show some differences compared to what may be expected from the modulated absorption spectrum. Generally, the hole burning spectrum shown in Fig. 7.2 is dominated by a single peak near 2.02 eV, however there are some smaller peaks in the spectrum in addition to the main peak. The overall magnitude of the nonlinear signal increases as a function of ω_1 energy and most of the qualitative features of the nonlinear spectrum, in particular the main peak near 2.02 eV, do not change significantly. This behavior is attributed to the energy transfer effect between DS and excitons that was explored in the last chapter that produces a larger overall signal as the ω_1 energy is increased. Close inspection of the data shows that there is some evidence that the nonlinear response tracks with the ω_1 energy. In particular, we observe that the peak near 2.02 eV seems to shift to the low energy side for the red and blue colored spectra in Fig. 7.2. A negative dT/T signal is also observed for lower energy ω_1 tuning. The physical origin of this effect will be discussed further shortly.

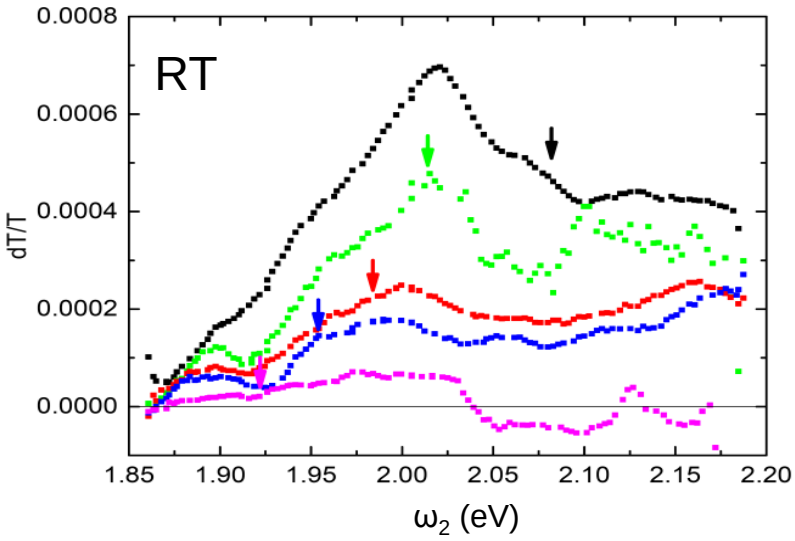

Figure 7.2: Nondegenerate nonlinear absorption spectrum at room temperature showing the spectral hole burning repsonse. The arrows represent the fixed energy of ω_1.

Nonlinear optical data at low temperature (10 K) is presented in Fig. 7.3. The scans in Fig. 7.2 have also been smoothed using an 8 point moving window average. The fact that the ω_2 scan at 10 K has a smaller range of energy values compared to room temperature has to do with the laser gain medium used in the measurement. In the room temperature measurement, the laser gain medium was changed from Rhodamine 6G laser dye (565 nm - 615 nm) to DCM laser dye (615 nm - 665 nm) in the middle of the measurement to obtain the full spectrum. The data shown in Fig. 7.3 was obtained using one dye laser operating with Kiton Red laser dye (600 - 645 nm) for ω_2 and a second dye laser operating with DCM for ω_1. Generally it is more difficult to accomplish a dye change in the middle of a measurement at low temperature while maintaining the sample in a fixed position since the overall data taking procedure (finding a strong signal, averaging) can exceed 12-15 hours and usually the vacuum degrades over this time. The sample chamber then needs to be re-evacuated that moves the sample slightly. We were therefore only able to take a 10 K data set over a relatively small wavelength range. Generally, the nonlinear signal strength does not

significantly change between low temperature and room temperature and variations in the nonlinear signal strength depend more heavily on the area of the sample that is probed. The data presented in Fig. 7.3 was taken at a different sample location compared to the data in Fig. 7.2, however the nonlinear signal strength is comparable to the room temperature data. In some cases, the overall nonlinear signal at room temperature is higher than low temperature at different sample positions.

A comparison of the nonlinear absorption spectra for different ω_1 values at 10 K shows some evidence of a positive dT/T response that tracks with ω_1, similar to the room temperature data. As in the room temperature data, the overall signal level increases as a function of ω_2 energy and there is a negative dT/T offset for large ω_1 - ω_2 detuning. As in the room temperature data, there also appears to be a series of resonances within the low temperature nonlinear optical response that could be from groups of excitons. There is also a large negative dT/T signal observed at higher energies for lower energy ω_1.

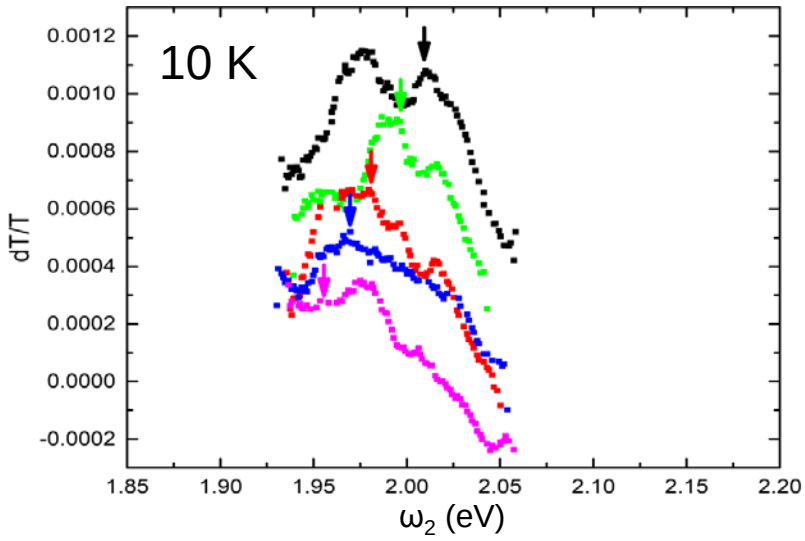

Figure 7.3: Nondegenerate nonlinear absorption spectrum at 10 K showing the spectral hole burning repsonse. The arrows represent the fixed energy of ω_1. The overall nonlinear signal level increases as a function of excitation energy and is not due to an arbitrary offset inserted into the plot.

7.2.1 Discussion on large scale resonance data

Normally we expect that the spectral hole burning response in an ensemble of two-level systems would show a relatively narrow (compared to the inhomogeneous bandwidth) resonance centered at zero ω_1 - ω_2 detuning ($\omega_1 = \omega_2$) that tracks with the ω_1 energy. Although there is some evidence of ω_1 tracking in the data in Figs. 7.2 and 7.3, the overall shape of the spectrum appears to be relatively unchanged as a function of ω_1. To evaluate the data, we consider a simpler system such as an ensemble of non-interacting two-level systems where the dipole dephasing rate of each of the two-level systems is comparable to the inhomogeneous bandwidth. Both the dephasing rate and inhomogeneous bandwidth are assumed large compared to the population decay rate γ_2. The theoretical hole burning response for an ensemble of two level systems (where the transition frequencies are assumed to be inhomogeneously broadened as described by a Gaussian distribution) with population decay rate γ_2, pure dephasing rate $\Gamma = 100\gamma_2$ and inhomogeneous bandwidth $\sigma_\omega = 200\gamma_2$ is presented in Fig. 7.4 following equation 3.39. Population pulsations are left out of the plot in Fig. 7.4 because they are generally too narrow to resolve in the hole burning measurements in this section. It is observed in the theory that there is some tracking of the signal with ω_1, exemplified by the shifting of the peak of the nonlinear signal, however the overall shape of the nonlinear spectrum remains unchanged. This behavior appears to be similar to some of the behavior in the nonlinear absorption data in Figs. 7.2 and 7.3.

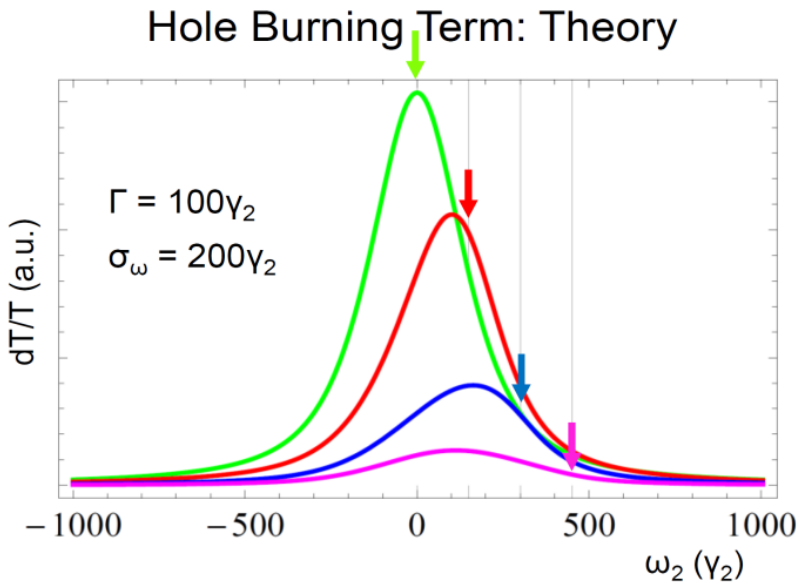

Figure 7.4: Theoretical nonlinear optical response from equation 3.39 as a function of γ_2 with $\Gamma = 100\gamma_2$ and $\sigma_\omega = 200\gamma_2$ for an ensemble of homogeneously broadened, closed two level systems.

Although the theoretical response can reproduce some of the basic features of the data, we also note that there are significant deviations from the two-level system ensemble theory in the data. First, there is some evidence of an enhanced dT/T signal at higher energy (around 2.18 nm) for some ω_1 values (1.92-1.97 eV). It is possible that this effect comes from absorption saturation of ω_2 due to exciton excited states in the system. In general, it is difficult to accurately calculate the energy separation of exciton excited states in the system because the exact quantum confinement potential is unknown, however the TiberCAD simulation of a single DINW shown

in Fig. 2.6 gives an energy separation between the lowest energy exciton state and the first excited state of $\Delta E = 0.264$ eV, roughly consistent with what is observed in Fig 7.2. Note again that the TiberCAD simulation is an approximation and a more accurate estimate will require an exact knowledge of the quantum confinement potential, nevertheless it is conceivable that the positive dT/T feature is associated with excited states in the system. Similar effects have been observed due to from exciton excited states in III-As interface fluctuation dots [155]. Next, as noted previously the spectrum shows a series of resonances instead of a smooth curve as shown in the theory. It is possible that these peaks are from different groups of DINW excitons or possibly exciton excited states. Finally, a negative dT/T signal is present for large ω_1-ω_2 detuning with $\omega_2 < \omega_1$. It is possible that the negative dT/T signal is related to internal electric field screening as described in chapter 5, where the increase in the exciton dipole moment as a result of the screening results in a higher population decay rate of the background disorder states [11, 181]. A more complete physical model of the system will require further investigation.

As a whole, the hole burning data presented in this section indicates that excitons in InGaN DINWs have extremely large homogeneous linewidths, even at low temperature, compared to excitons in quantum dot structures made from other materials such as GaAs. Based on the linewidth of the inhomogeneously broadened nonlinear spectrum shown in the modulated absorption data ($\sim$ 100 meV) and the theoretical analysis presented previously, we estimate that the homogeneous linewidth is $\sim$ 50 meV at both room temperature and low temperature. A source of very fast dipole dephasing that is not related to phonon induced processes is needed to explain this feature. We suggest that one possible origin for this effect in the DINW sample is Coulomb interactions between rapidly relaxing background disorder states and excitons. It is possible that electron-hole pairs excited into excitons or DS can rapidly transfer into lower energy states that results in a fast spectral diffusion and therefore a fast dipole dephasing rate.

7.3 Coherent nonlinear optical spectrum: population pulsation resonances

In this section, the population pulsation resonances are presented. Generally, measuring the population pulsation component of the nonlinear response in addition to the hole burning response is done because the population pulsations can be used to easily extract the population decay times (T_1) of the states probed in the hole burning measurement. Time-resolved PL data of similar DINW structures can be used to estimate the population decay rate of the exciton and the corresponding line width that we would expect in for the population pulsation resonance in the nonlinear optical response. Typically data for red emitting DINWs shows exciton decay times $\sim$500 ps-1 ns [55]. This value largely depends on the strength of the internal electric field due to the quantum confined Stark effect. In this section narrow resonances in the coherent nonlinear optical spectrum are reported that are attributed to population pulsations. We find that the linewidth of the resonance is slightly narrower than what we would expect from previous studies [55] by a factor of 3-5, however it is quite possibly due to variations in the growth properties of the sample featured here compared to in other studies. As expected, the population pulsation resonances are on top of a nearly flat background dT/T signal that is from the broad hole burning response that was discussed in the previous section.

The population pulsation data is taken by fixing ω_1, provided by a frequency stabilized dye laser and scanning ω_2, provided by another frequency stabilized dye laser, over the resonances probed by ω_1. The bandwidth of each laser is $\sim$ 1 MHz. In Fig. 7.5, narrow population pulsation resonances are shown in each panel for a ω_1 energy shown by the arrow in the inset of each panel. The insets show the spectral position of ω_1 with respect to the distribution probed in modulated absorption, where the modulated absorption data is given by the red data points. Note that in this case the modulated absorption and population pulsation spectra are probed at the same sample region. Here we observe that the population pulsation resonances can be fit by a single Lorentzian curve when ω_1 is tuned near the center of the modulated absorption distribution, however there is an interference-type component in the population

pulsation resonance that becomes more pronounced as a function of detuning from the center of the modulated absorption distribution. The interference resonance also changes orientation (sign depending on whether ω_1 is tuned to the high or low energy side of the modulated absorption distribution.

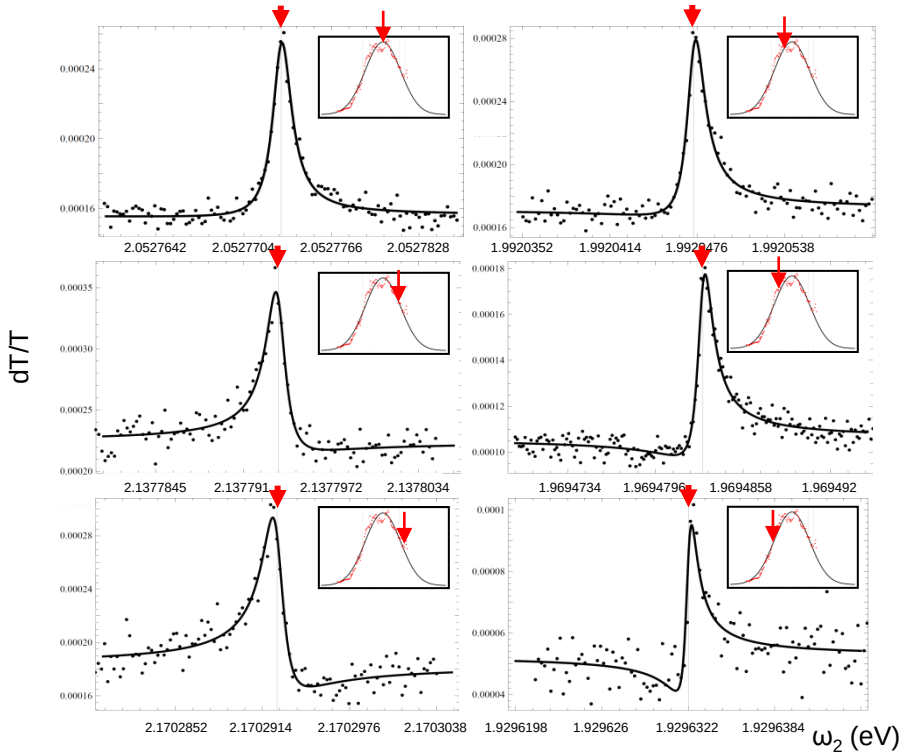

Figure 7.5: Population pulsation resonances shown for different ω_1 energies at room temperature, given by the red arrows. The energy of ω_1 is shown with repsect to the modulated absorption distribution in the inset of each plot. The black line is a least-squares fit to the data using equation 7.1.

The power dependence of the linewidth of population pulsations when ω_1 is tuned near the center of the modulated absorption distribution was measured and shown in Appendix C. In this case, the population pulsation resonance can be approximately fit to a Lorentzian, as shown in Fig. 7.5. It is found that the linewidth of the population pulsation resonance increases monotonically as a function of ω_1 power, even when

the signal is verified to be in the $\chi^{(3)}$ limit by verifying that the nonlinear signal doubles when either the ω_1 or ω_2 intensity doubles. From the analysis in chapter 3, this behavior is not expected in an isolated two-level system. Further investigation is needed to understand this effect.

The population pulsation terms show a strong sensitivity to the polarization of the excitation beams. For a fixed ω_1, the population pulsation spectrum is shown as a function of ω_1-ω_2 detuning for co-polarized beams (top panel) and cross-polarized beams (bottom panel) in Fig. 7.6. As discussed in chapter 2, an uneven biaxial strain can lead to orthogonal linearly polarized selection rules for the A and B valence bands and significant band splitting. As a result, the coupling to an exciton transition within a DINW depends heavily on the degree (and direction) of linear polarization of the excitation lasers. When ω_1 and ω_2 are co-polarized, population pulsations result due to interference effects between the two beams. When the beams are cross-polarized, the beams are not coupled efficiently to the same transition, therefore the interference effects should disappear. We find instead that the cross-polarized population pulsation resonance does not disappear, but rather shows a weak resonance that has twice the width of the co-polarized response. This effect could be a result of new physics in the system, but the analysis is still in the preliminary stages.

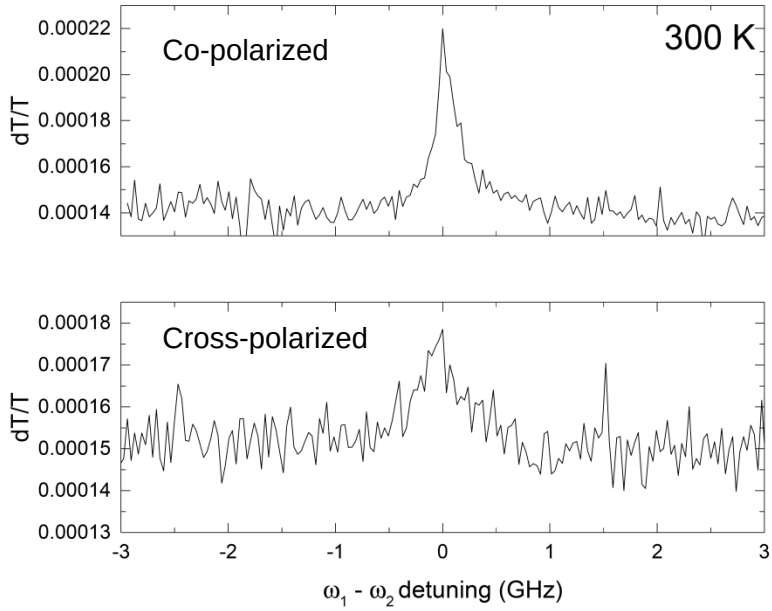

Figure 7.6: Room temperature population pulsation resonance for co-polarized ω_1 and ω_2 (top panel) and cross-polarized ω_1 and ω_2 (bottom panel). The signal is taken near the peak of the modulated absorption distribution.

We observe that on average the linewidth of the population pulsation is essentially the same at room temperature and low temperature within a factor of $\sim$1.5. Note that this behavior is very different from the self-assembled sample featured in chapter 5. The self-assembled sample showed an ultranarrow population pulsation resonance that had a width determined by the metastable decay rate. As a function of temperature, the width of the ultranarrow resonance increased exponentially due to the temperature dependence of the metastable state population. In this case, the temperature-dependent dynamics of the population pulsation is not as well understood, but is robust at room temperature. In Fig. 7.7 the coherent population pulsation response is presented for two different ω_1 values, where the energy of ω_1 within the modulated absorption spectrum is shown in the insets. Note that in this data the modulated absorption and nonlinear absorption are not taken in the same sample region. The line width of the population pulsations observed in Fig. 7.7 is

essentially the same as the line width of the room temperature resonances observed in Fig. 7.5. It is also interesting that the extra resonances associated with decoherence are observed in both the room temperature and 10 K data.

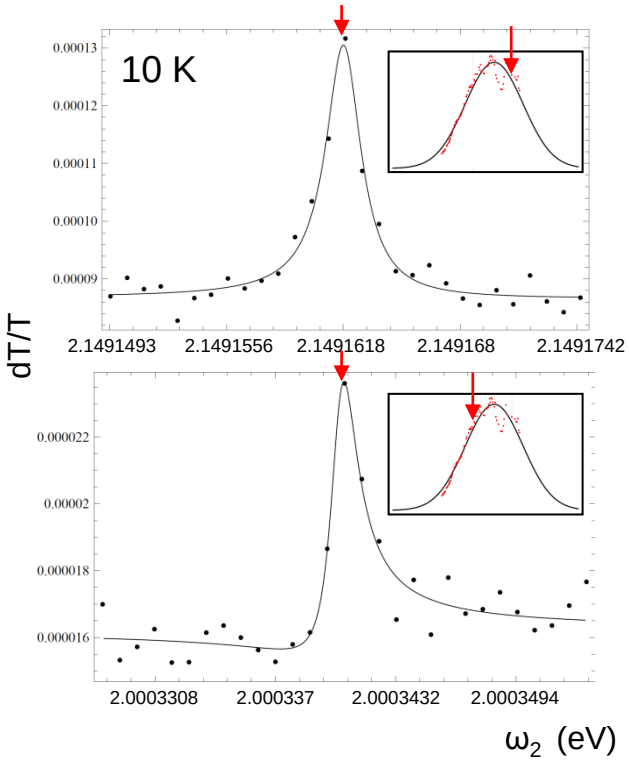

Figure 7.7: Population pulsation resonances shown for different ω_1 energies at 10 K, given by the red arrows. The energy of ω_1 is shown with repsect to the modulated absorption distribution in the inset of each plot. The black line is a least-squares fit to the data using equation 7.1.

7.3.1 Discussion

7.3.1.1 Decoherence-induced extra resonances

One of the most interesting features of the population pulsation data is the fact that the population pulsation resonances show an interference-type effect that is more pronounced as a function of ω_1 detuning from the modulated absorption line center. The focus of this discussion will be on how the interference-type resonances can be described as decoherence-induced extra resonances. The data presented in this

chapter is the first evidence of decoherence-induced extra resonances in a solid state system.

As a starting point to the discussion, a phenomenological model of the DINW ensemble is discussed. Based on previous work, it might be assumed that a single InGaN DINW has a somewhat similar optical behavior to a single quantum dot based on the fact that single photon emission has been observed from single DINWs, however our recent data now indicates that this description of the DINW system is complicated by the presence of background disorder states that lead to effects such as charge/energy transfer and negative dT/T signals. We instead consider a phenomenological model in which a two-level system is used to describe the nonlinear absorption of the DINW with the understanding that the excited state represents the creation of an electron-hole pair with a large rate of spectral diffusion. Physically, the excited state can represent the creation of an exciton within a DINW that can transfer into background DS and recombine radiatively, for example. Obviously, reliable coherent control in this type of system would be extremely difficult except on very short time scales. A similar type of quasi-2 level system approach was used to describe population pulsation dynamics in a 2-D $MoSe_2$ system [160]. It is assumed that the rate of spectral diffusion is fast compared to the population decay rate in the two-level system. Based on the spectral hole burning data presented in the previous section that showed very large homogeneous broadening, this assumption seems to be plausible. Assuming the rate of spectral diffusion is very fast compared to the population decay rate, each DINW behaves like a homogeneously broadened two-level system where the dipole decay rate $\gamma = \gamma_2/2 + \Gamma_{SD}$, where Γ_{SD} is the pure dephasing rate due to the fast exciton spectral diffusion. Note that this model does not properly describe the dynamics for slow spectral diffusion and is therefore approximate.

Under the assumption that each DINW is modeled as a quasi-two-level system, an understanding of the nonlinear optical response will require an averaging over the nonlinear signal from the distribution of DINWs within the field of view of the measurement. As an approximation, we consider that the inhomogeneously broadened nonlinear signal distribution is given by the Gaussian fit to the modulated absorption

data. The coherent nonlinear optical response of our sample can then be theoretically described using the nonlinear optical response of an ensemble of two-level systems in section 3.2.3. From the hole burning data, we expect that the homogeneous linewidth of the individual DINWs is similar to the inhomogeneous bandwidth.

In Fig. 7.8, the theoretical population pulsation resonances are presented for an inhomogeneously broadened distribution of two-level systems as a function of ω_1 - ω_2 detuning. The inhomogeneous distribution that is averaged over to obtain the nonlinear signal is shown in the top panel of Fig. 7.8, assumed to be a Gaussian (width = $10000\gamma_2$) for simplicity. In the bottom two panels, the nonlinear reponse that is centered at zero ω_1 - ω_2 detuning is presented. In the bottom left panel, the population pulsation resonances are shown for no pure dephasing and in the bottom right panel a pure dephasing rate $\Gamma = 8000\gamma_2$ is assumed. Each color represents a different fixed value of ω_1 that are given by the arrows on the top panel with the corresponding color. In the absence of pure dephasing, the spectral hole shows a single Lorentzian resonance at zero ω_1 - ω_2 detuning for any value of ω_1 within the inhomogeneous distribution. When the pure dephasing rate $\Gamma >> \gamma_2$, the resonances show significant interference-type effects that become more pronounced as a function of ω_1 detuning from the line center of the inhomogeneous distribution. Furthermore, the interference line shapes change orientation depending on whether ω_1 is tuned to the low energy or higher energy side of the inhomogeneous distribution. The population pulsation resonances are on top of a constant offset signal in the bottom right panel of Fig. 7.8 due to the broad spectral hole burning response. It is important to note that the interference-type resonances are only easily visible when the pure dephasing rate is much larger than γ_2. The interference resonances are a type of decoherence-induced extra resonance that was described in section 3.2.2.1. From the theory presented in Fig. 7.8, the interference effects observed in the population pulsation resonances observed in 7.5 are attributed to similar decoherence induced extra resonances, where the inhomogeneous distribution is given by the modulated absorption data.

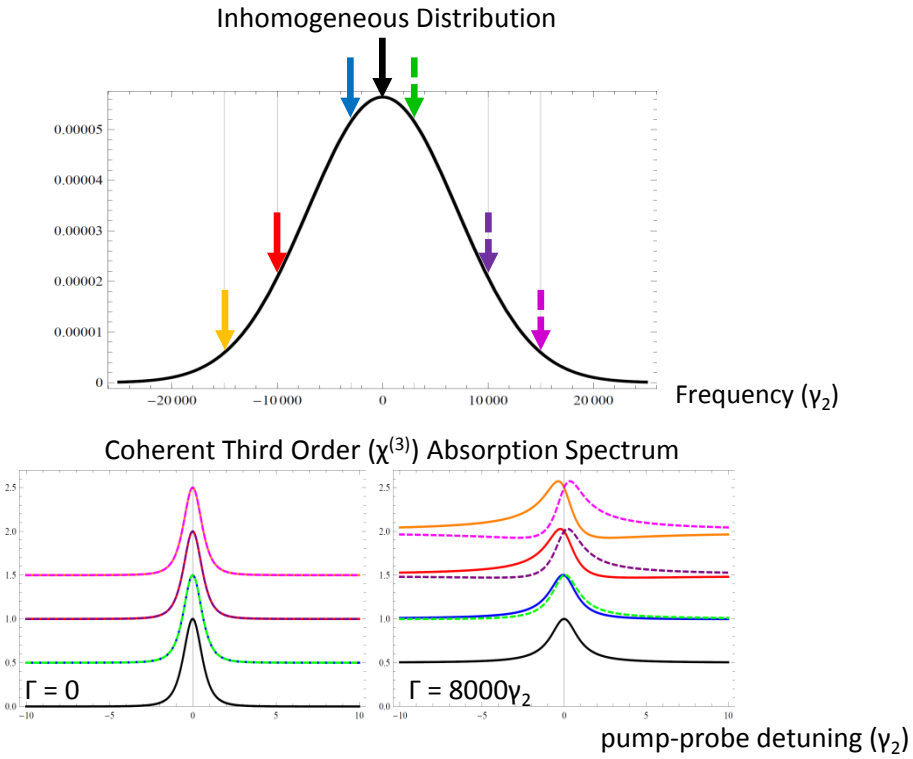

Figure 7.8: The top panel shows an inhomogeneous distribution with a width given by $10000\gamma_2$ as a function of γ_2. The nonlinear signal is averaged over the inhomogeneous distribution. The bottom two panels show the population pulsation response for different values of pure dephasing, where the pure dephasing rate $\Gamma = \Gamma_{SD}$, plotted as a function of ω_1 - ω_2 detuning. The colored arrows give the frequency of ω_1.

It is useful to fit the data using 2-level system theory to obtain estimates of fundamental parameters. To fit the data in Fig. 7.5, the third order nonlinear optical response describing the population pulsation resonances in an inhomogeneously broadened system will be used. We note again that the linewidth of the nonlinear response from the hole burning term is very broad due to the fast spectral diffusion that it effectively only adds a constant offset to the nonlinear spectrum in Figs.7.5 and 7.7. Therefore, for the purposes of modeling the data, the hole burning response will be treated as a constant offset. The population pulsation component of the nonlinear signal from the inhomogeneously broadened ensemble of DINWs is proportional to the third order off-diagonal density matrix element from chapter 3:

$$\rho_{21}^{I(3)}(\boldsymbol{R},t) = -2i\chi_2|\chi_1|^2 e^{i(\boldsymbol{k_2}\cdot\boldsymbol{R}+\delta_2 t)}\frac{\sqrt{\pi}}{\sigma_\omega}([(1+\frac{2\Gamma_{SD}(\omega_1)}{\gamma_2(\omega_1)}) \times\frac{1}{\omega_2-\omega_1+2i\gamma(\omega_1)}(\frac{1}{\omega_2-\omega_1}(w(z(\omega_1-\bar{\omega_0}))-w(z(\omega_2-\bar{\omega_0}))+ \frac{1}{2i\gamma(\omega_1)}(w(z(\omega_1-\bar{\omega_0}))+w(z_1(\omega_1-\bar{\omega_0})))], \tag{7.1}$$

where

$$z(\omega) = \frac{\omega + i\gamma(\omega_1)}{\sigma_\omega} \tag{7.2}$$

and

$$z_1(\omega) = \frac{-\omega + i\gamma(\omega_1)}{\sigma_\omega}, \tag{7.3}$$

and where the fact that the spectral diffusion and population decay rates depend on the subgroup of DINWs that is probed at the fixed ω_1 frequency has been explicitly included. The parameter $\bar{\omega_0}$ is the center of the inhomogeneous distribution that is written explicitly in this case (see Appendix A for the usual convention). Note that the assumption that the decay rates in the system are function of energy does not affect the integrals in the calculation of the third order off-diagonal density matrix element in Appendix A.

We fit each resonance in Fig. 7.5 using equation 7.1 with the addition of a constant offset for the hole burning resonance. The fits are given by the black lines in the main panels of Fig. 7.5 using a least-squares method, with σ_ω, $\bar{\omega}_0$, γ_2, Γ_{SD}, and ω_1 as fitting parameters. The red arrows in Fig. 7.5 give the locations of ω_1 based on the fits. A Gaussian inhomogeneous distribution is assumed for the fit based on the modulated absorption data, however more accurate modeling will have to take into account the resonant behavior in the nonlinear signal within the Gaussian distribution. Even with the simplifying assumption of a Gaussian inhomogeneous distribution, the fits seem to show good agreement with the data. We note that the average value of $\bar{\omega}_0$ obtained from the fits was found to be 2.047 eV, in agreement with the center of the modulated absorption spectrum that was found to be 2.041 eV. Unfortunately, the fit seems to underestimate the width of the Gaussian distribution shown in the modulated absorption data by a factor of $\sim$2, which could be an error associated with the fact that the real inhomogeneous distribution is not a smooth Gaussian. It is found that the average value of the spectral diffusion rate (expressed in energy

units) is 33.1 meV, a value that agrees reasonably well with our estimate from the spectral hole burning data. One of the most interesting effects from the population pulsation fits is found in the extracted values of the population decay rates. The population decay rate γ_2 was found to range between shows a strong dependence on ω_1. In Fig. 7.9, the decay rates γ_2 are plotted as a function of ω_1, along with the modulated absorption plotted as a function of ω_2. We find that the decay rates decrease rapidly on the low energy side of the modulated absorption data and seem to flatten out on the higher energy side. This effect could be related to lower energy transfer rates of the background disorder states at lower energies. It is possible that this data can also help to explain the blue shift of the modulated absorption data from the PL. This result is still being studied.

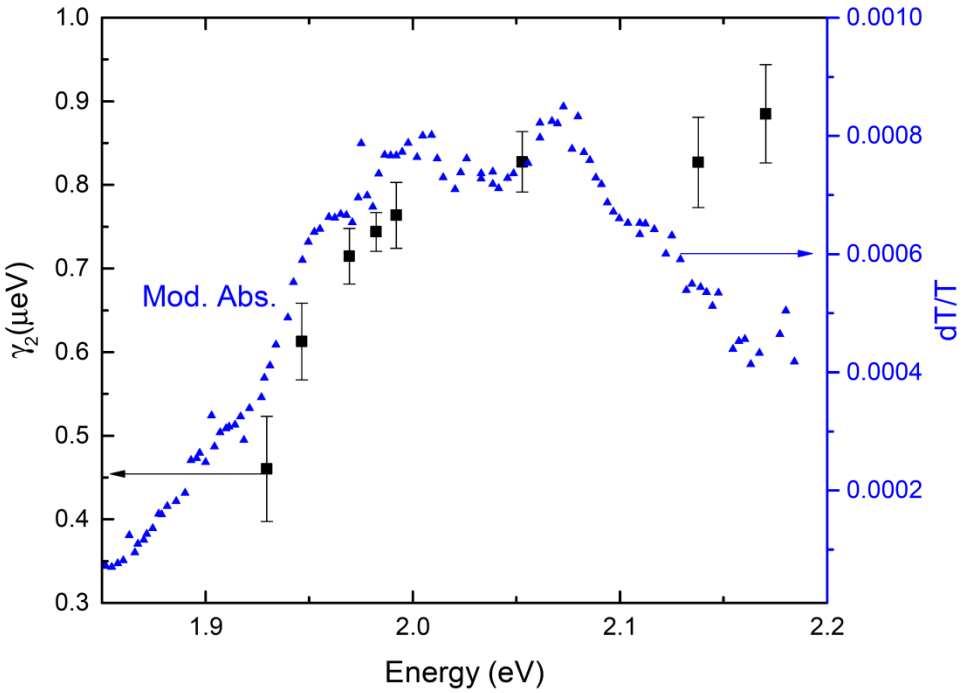

Figure 7.9: Modulated absorption data (blue points) plotted as a function of ω_2 (also shown in Fig. 7.1 at room temperature. The population decay rates γ_2 are also shown as a function of ω_1. The error bars are from the error to the fit, where the data and fit are shown in Fig. 7.5.

A fit to the low temperature population pulsation data in Fig. 7.7 using equation 7.1 is shown by the black lines in each panel of Fig. 7.7. From the fit, it is found that the values of the population decay rate γ_2 (~ 0.8 μeV) and the inverse decoherence

rate ($\Gamma_{SD} \sim 30$ meV) is similar to what is found in the room temperature data. It should be noted again that the low temperature and room temperature data were taken at slightly different regions of the sample. The fact that the decoherence rate is similar in the room temperature and low temperature data is consistent with what is observed in the hole burning data.

7.4 Summary

In this chapter, the third order coherent nonlinear optical spectrum was presented for an ensemble of selective area red-emitting InGaN DINWs. It was found that the nonlinear absorption spectrum showed evidence of excitonic absorption, where the dephasing rate of the excitons is $\sim$ 20-40 meV, even at low temperature. The large dephasing rate in the system results in decoherence-induced extra resonances in the population pulsation terms of the coherent nonlinear spectrum, an effect that has never been observed in a solid-state system. Fast dipole dephasing caused by spectral diffusion in the system does not bode well for the use of red emitting InGaN quantum dots in quantum information processing applications and further materials engineering will be required in order to implement advanced coherent control applications. This will require further study in order to understand the exact origins of the decoherence that is virtually independent of temperature. At the same time, it is truly remarkable that the population lifetimes of DINW excitons are virtually unchanged at room temperature and low temperature in this system.

CHAPTER 8

Summary and Future Directions

The work in this thesis has been centered on coherent nonlinear optical spectroscopy measurements of ensembles of InGaN disks in GaN nanowires to evaluate the material for potential use in future applications such as quantum information processing. The results of this work show that the realization of coherent control for quantum information processing in this system is limited by dephasing processes due to the presence of material disorder or metastable trap states formed by nanowire coalescence. At the same time, this work showed that the lifetime of excited electron-hole pairs in the system appears to be virtually unaffected by interactions from phonons at room temperature compared to cryogenic temperatures, which could give motivation for materials scientists to improve growth techniques and correct the effects of disorder in the system. This chapter will summarize the results of the work in this thesis and mention the ways in which future optical experiments can extend this work to better understand the optical physics of this system. This chapter will also discuss future prospects for the InGaN system in coherent optical control applications such quantum information processing that was the overarching theme of this work.

8.1 Results Summary

The first part of the data presented in the thesis involved self-assembled DINW samples. The nonlinear absorption spectrum in self-assembled ensembles of InGaN DINWs grown on Si substrates was essentially dominated by effects related to long-lived charge trap states. The presence of long-lived trap states was verified from the

observation of ultranarrow population pulsation resonances that were supplemented with a phase modulation measurement. The charge traps were found to have several effects on the nonlinear optical spectrum: first, a negative dT/T offset was signal produced that was associated with screening effects and second, resonances that were assigned to exciton resonances produced a positive dT/T signal. The signal strength of the negative dT/T offset and the positive dT/T signal were not correlated and varied over the sample surface. Nanowire coalescence in the self-assembled sample occured due to roughness in substrate that lead to the formation of charge traps at the coalescent boundaries. We attribute the behavior of the nonlinear signal to interactions between metastable trap states formed due to coalescence and excitons.

The second part of the data sections in the thesis dealt with selective area DINW samples that showed interesting optical physics related to background disorder. Because of the nanowire uniformity in the selective area growth technique, coalescence of nanowires in this sample was negligible. Hence, we did not observe significant effects from metastable trap states. It was proposed that electron-hole pairs can be excited into background disorder states and subsequently decay into lower energy exciton states before radiatively recombining. This behavior was thought to be responsible for a stair-case shaped intensity-dependent PL spectrum in which discrete blueshifts occur due to state filling of the background disorder states and subsequent tunneling into lower energy DINW exciton states that provided most of the emission in the sample. The presence of background disorder states in the system was confirmed using a PLE measurement that showed an exponential dependence on excitation energy, a well-known signature of disorder in the system. The physical interpretation of the intensity-dependent PL was supported by nonlinear absorption data that showed evidence of energy transfer between between background disorder states (that follow an exponential density of states based on the PLE spectrum) and lower energy excitons.

The coherent nonlinear absorption spectrum of the selective area sample showed evidence of extremely fast (rate $\sim$30-40 meV) exciton dipole decoherence based on a spectral hole burning measurement at both room temperature and low temperature. As a result of the fast decoherence, population pulsation resonances in the sample

showed decoherence-induced extra resonances (DIER) that were measured for the first time in a solid-state system. This type of effect is closely related to pressure-induced extra resonances (PIER) [30,143] that were predicted [145,146] and observed [147,148] in four-wave mixing studies. A more extensive discussion of the physics associated with DIER is found in chapter 3. Individual DINWs were modeled using a quasi-two-level system in which the excited state represented the excitation of an electron-hole pair (assumed to have a large degree of spectral diffusion) and the ground state of the two-level system is the crystal ground state.

8.2 Future work in the current system

As noted in chapters 5-7, there are some open questions related to the analysis of the coherent nonlinear optical spectrum and the linear optical spectra. First, although it is possible that some of the sample emission in both the self-assembled and selective area samples comes from the background disorder states, it is unclear what are the relative radiative efficiencies of the background disorder states and the excitons. This question will become important to address in future applications that utilize the fact that some DINW structures seem to support engineered single photon emission. Further, in self-assembled samples, a consistent theory is required to properly describe coexistence of a negative dT/T offset (induced absorption) and a positive dT/T signals that are related to metastable trap states while incorporating the background disorder states that were observed in the PLE spectrum and excitons. Negative dT/T signals were also observed in selective area samples for large detunings of the scanning and non-scanning beams. The selective area sample also showed some unusual behavior in the the linewidth of the population pulsation terms depended on the power of the excitation beams, even when the signal was verified to be in the $\chi^{(3)}$ limit, as shown in Appendix B. A theoretical interpretation of the wavelength dependence of the population pulsation decay rates shown in Fig. 7.9 is also needed. If a Hamiltonian is to be formulated for the system, it is likely that it will need to incorporate the effects of exciting of multiple electron-hole pairs. Immediate future

work should be based on developing a unified theoretical picture of the system.

It is possible that a great deal of new optical physics in the samples featured in this work could be obtained by probing the spatiotemporal dynamics of excited electron-hole pairs in the system. In chapter 7, we assumed that the system could be modeled as a two-level system that represented the creation of an electron-hole pair with a large amount of spectral diffusion. As part of the spectral diffusion process, the electron could hop from one localized state in the material to another, for example from a localized disorder state to the exciton. One interesting future experiment could involve measuring the population pulsation terms featured in chapter 7 as a function of angle between the ω_1 and ω_2 beams. Similar types of measurements have shown that the spatial diffusion length of excitons can be measured using the angular dependence of the four-wave-mixing signal [182]. It is possible that this measurement is easier to interpret in the time domain, where fast initial decays can be more easily distinguished. Along the same vein, it may be useful to simply perform a pump-probe measurement in the time-domain to observe the femtosecond dynamics of charge carriers in the system [183]. Fast ($\sim$ femtosecond) decays from background disorder states that interact with excitons could be useful in explaining the fast decoherence rate in the system. For larger diameter DINWs, near-field microscopy techniques [184, 185] could be useful in distinguishing the positions of disorder states from excitons, for example. Near field techniques can also be used to comment on the sources of photoluminescence in the system (i.e. how much of the luminescence comes from disorder states and how much from excitons). Future experimental work in the DINW ensemble samples should be geared toward understanding the solid state environment within each DINW if possible.

8.2.1 Nonlinear spectroscopy in single DINW samples

The analysis in this work was also complicated by the fact that the nonlinear signal originated from ensembles of InGaN DINWs therefore averaging over the ensemble was required to understand the nonlinear spectrum. The averaging can result

in complicated expressions for the nonlinear optical response and the inhomogeneous broadening can obscure important optical physics that are required to better understand the system. A natural extension to this work is to perform nonlinear optical measurements on single DINWs. Depending on the exact band structure (strain properties), it may be possible to resolve exciton fine structure in a single DINW despite the very broad line widths in the system [186] in nonlinear absorption. Isolation of a single quantum dot will also allow for more accurate temperature-dependent studies. Finally, the linewidth of the single DINW will be typically be smaller than the ensemble linewidths featured in this study, therefore it will likely be easier to observe a more complete nonlinear absorption spectrum when either of the beams is tuned off resonance.

There have been attempts by our group to observe third order nonlinear signals from samples that contain a low density $\sim 1 \mu m^{-2}$ of DINWs with a single disk grown inside the nanowire in both self-assembled and selective area samples. Thus far, within our experimental sensitivity ($\sim 10^{-6}$) we have not been able to reliably measure a third order nonlinear optical signal from a single DINW. We have observed modulated absorption signals for very high intensity ω_1 fields, however this measurement was taken well beyond the $\chi^{(3)}$ limit and is therefore not very useful. It is likely that the large dephasing rates in the single DINWs limit the magnitude of the third order nonlinear signal. It is possible that other techniques such as resonance flourescence can be used for exploring the optical physics of individual DINWs at very high sensitivity ($s \sim 10^{-7}$) [187]. This technique has been used for measuring the excited state dynamics and nonlinear optical physics of individual InAs quantum dots [127, 188]. Future work could be aimed at measuring and characterizing resonance fluorescence from individual DINWs, however measuring a resonance fluorescence signal will require significant engineering based of the current optical set-up.

8.3 Future work towards quantum information processing using InGaN quantum dot structures

If III-nitride materials are going to have similar success in quantum optical demonstrations towards quantum information processing, clearly the optical linewidth of the system needs to be reduced, even to the lifetime limited value. Although the work in this thesis and other work in III-nitrides [189] points to fast or slow spectral diffusion processes as one source of line broadening, the exact source of the spectral diffusion and how to eliminate this effect during growth is not presently known. At the same time, there have been several engineering techniques that have been effective in reducing the optical linewidth somewhat. For example, is it known that the presence of an internal electric field along the growth direction can exacerbate the Coulomb shifts caused by interactions between excitons and nearby charges [149, 190, 191], so it is possible that reducing or eliminating the internal electric field can be effective in lowering the optical linewidth [192]. One way to accomplish this is to grow zinc-blende III-nitride quantum dots rather than wurtzite, a crystal configuration that eliminates the internal electric fields [193, 194]. It is also possible to grow III-nitrides along a non-polar direction that gives similar results [195]. It may also be possible that a reduction in the volume of the quantum dot active area can reduce the effect of background states and decrease the optical linewidth of the dot emission. Reducing the size of the dot is also advantageous for optical applications because of the increase in quantum confinement [196]. Recently it has been shown using photochemical techniques that it is possible to control the size of quantum dot structures and acheive a corresponding reduction in linewidth for InGaN samples [197]. Finally, there is a trade-off between the degree of quantum confinement and the degree of disorder specifically for varying the InN concentration in InGaN samples. A balance should be found between the degree of quantum confinement and the degree of disorder that is tolerable in the experiment.

Some quantum information processing applications do not utilize coherent optical control of quantum dots, but rather use the polarization state of the emitted single photons and optical elements such as waveplates to perform quantum computations [43,198]. In this type of quantum information processing scheme, the optical linewidth of the dot is less important. However, it should be noted that unwanted emission from

disorder may affect the reliability of the single photon emission if InGaN quantum dots are used in this way. Material engineering should still be aimed at controlling the degree of disorder before considering red emitting InGaN for this type of application.

8.4 Conclusion

In this work third order coherent nonlinear optical spectroscopy was performed on two different ensembles of InGaN disks in GaN nanowires. The nonlinear optical spectra were used to characterize quantum confined excitons in the material and to further our understanding of the optical physics associated with disorder and metastable trap states in the system. It was found that although quantum confined excitons in the system can survive without dissociation up to room temperature, decoherence processes in the sample at cryogenic temperatures and room temperature prohibit the use of individual DINWs in coherent control applications such as quantum computation without further material improvements.

APPENDICES

APPENDIX A

Calculation of third order off-diagonal density matrix elements for an inhomogeneously broadened two-level system

Some of the details related to the calculation of the theoretical third order ($\chi^{(3)}$) coherent nonlinear optical signal for an inhomogeneously broadened ensemble of two level systems will be outlined in this Appendix. The purpose here is to provide a reference to show the algebra involved in the calculation with the correct signs.

It is assumed that the system of interest is an ensemble of closed, homogeneously broadened two-level systems where the transition frequencies of the individual two-level systems is inhomogeneously broadened around an average transition frequency $\bar{\omega}_0$ and are distributed according to a Gaussian distribution:

$$W_f(\Delta) = \frac{1}{\sqrt{\pi}\sigma_\omega} e^{-(\Delta/\sigma_\omega)^2} \tag{A.1}$$

where $\Delta = \omega_0$ - $\bar{\omega}_0$.

In a field interaction representation, the third order off-diagonal density matrix element is given by

$$\begin{aligned} &\rho_{21}^{I(3)}(\boldsymbol{R}, \Delta, t) = 2i \sum_{\mu,\nu,\sigma=1,2} \chi_\mu \chi_\nu^* \chi_\sigma e^{i(\boldsymbol{k_s}\cdot\boldsymbol{R} + \delta_s t} \\ &\times \frac{1}{(\gamma + i\delta_s(\Delta))(\gamma + i\delta_\mu(\Delta))(\gamma - i\delta_\nu(\Delta))} [1 + \frac{2\Gamma}{\gamma_2 - i(\omega_\nu - \omega_\mu)}], \end{aligned} \tag{A.2}$$

where $\delta_\mu(\Delta) = \bar{\omega}_0 - \omega_\mu + \Delta$. For simplicity, we redefine ω_{mu} so that $\omega_\mu \rightarrow \omega_\mu$ - $\bar{\omega}_0$.

To calculate the terms of interest, the "pump-probe" geometry is assumed in which the ω_2 and ω_1 beams are crossed at the sample and the ω_2 beam is detected as described in chapters 3 and 4. We first consider the saturation component of the

nonlinear optical response that is found by setting $\mu = \nu = 1$ and $\sigma = 2$. The resulting nonlinear term is given by

$$\begin{aligned}\rho_{21}^{I(3)}(\boldsymbol{R}, \Delta, t) &= |\chi_1|^2 \chi_2 e^{i(\boldsymbol{k_2}\cdot\boldsymbol{R}+\delta_2 t} \\ &\times \tfrac{2}{(-i\gamma-\delta_2(\Delta))(-i\gamma-\delta_1(\Delta))(-i\gamma+\delta_1(\Delta))}[1+\tfrac{2\Gamma}{\gamma_2}].\end{aligned} \tag{A.3}$$

The focus will now be on the resonant denominator in equation A.2:

$$\frac{1}{(-i\gamma+\Delta-\omega_1)(-i\gamma+\omega_2-\Delta)(-i\gamma+\Delta-\omega_2)}. \tag{A.4}$$

To calculate the nonlinear optical signal, this equation must be averaged over the inhomogeneous distribution in A.1. Before this averaging takes place, A.4 can be rewritten using partial fractions as:

$$\begin{aligned}&\tfrac{1}{-i\gamma+\Delta-\omega_2}[\tfrac{1}{-i\gamma+\Delta-\omega_1}+\tfrac{1}{-i\gamma-\Delta+\omega_2}]\tfrac{1}{(\omega_2-\omega_1-2i\gamma)} = \\ &\tfrac{i}{-i\gamma+\Delta-\omega_2}[(\tfrac{1}{-i\gamma+\Delta-\omega_2}-\tfrac{1}{-i\gamma+\Delta-\omega_1})\tfrac{1}{(\omega_2-\omega_1)}+(\tfrac{1}{-i\gamma+\Delta-\omega_2}+\tfrac{1}{-i\gamma-\Delta+\omega_2})\tfrac{1}{-2i\gamma}].\end{aligned} \tag{A.5}$$

The expression on the right hand side of A.5 contains 4 resonances that contain the detuning parameter Δ. Each of these expressions can be integrated over the inhomogeneous distribution in equation A.1, giving integrals such as

$$\frac{1}{\sqrt{\pi}\sigma_\omega}\int_\infty^\infty d\Delta e^{-(\Delta/\sigma_\omega)^2}\frac{1}{-i\gamma+\Delta-\omega_2}. \tag{A.6}$$

As noted in chapter 2, this term can be written in terms of the plasma dispersion function [199], given by

$$w(z) = \frac{i}{\pi}\int_\infty^\infty dx e^{-x^2}\frac{1}{z\pm x}, \tag{A.7}$$

where $Im(z) > 0$. This condition requires that the last resonant denominator on the right hand side of equation A.5 be multiplied by a factor of -1. For the population pulsation nonlinear term when $\mu = 2$, $\nu = 1$ and $\sigma = 1$, the third-order off diagonal density matrix element can be written as

$$\begin{aligned}\rho_{21}^{I(3)}(\boldsymbol{R}, \Delta, t) &= |\chi_1|^2 \chi_2 e^{i(\boldsymbol{k_2}\cdot\boldsymbol{R}+\delta_2 t} \\ &\times \tfrac{2}{(-i\gamma-\delta_2(\Delta))(-i\gamma+\delta_1(\Delta))^2}[1+\tfrac{2\Gamma}{\gamma_2+i(\omega_2-\omega_1)}].\end{aligned} \tag{A.8}$$

Again, we focus on the resonant denominator given by

$$\frac{1}{(-i\gamma-\delta_2(\Delta))(-i\gamma+\delta_1(\Delta))^2}, \tag{A.9}$$

which can be written in terms of partial fractions as

$$\frac{1}{(-i\gamma+\Delta-\omega_1)^2}\frac{1}{-2i\gamma+\omega_2-\omega_1}+\frac{1}{-i\gamma+\Delta-\omega_1}\left(\frac{1}{-2i\gamma+\omega_2-\omega_1}\right)^2+ \\ \frac{1}{-i\gamma-\Delta+\omega_2}\left(\frac{1}{-2i\gamma+\omega_2-\omega_1}\right)^2. \tag{A.10}$$

To solve the first term in equation A.10, we note that the derivative of the plasma dispersion function is given by

$$\frac{dw(z)}{dz}=\frac{-i}{\pi}\int_{\infty}^{\infty}dxe^{-x^2}\frac{1}{(z\pm x)^2}. \tag{A.11}$$

The first term in equation A.10 can therefore be expressed as

$$-\frac{\sqrt{\pi}}{\sigma_\omega^2}\left(\frac{1}{\omega_2-\omega_1-2i\gamma}\right)\frac{dw(z)}{dz}. \tag{A.12}$$

By rewriting the terms in equations A.5 and A.10 in terms of the plasma dispersion function and derivatives of the plasma dispersion function, the total third order nonlinear optical response can be written as equation 3.39.

APPENDIX B

Intensity-dependent PL in the self-assembled samples

The excitation intensity PL spectrum of the self assembled sample is shown in Fig. B.1. Unlike in the selective area sample, the PL does not show a significant energy shift as a function of excitation intensity. It should be noted that the density of background disorder states in the self-assembled samples is lower than the selective area samples due to the smaller DINW diameter.

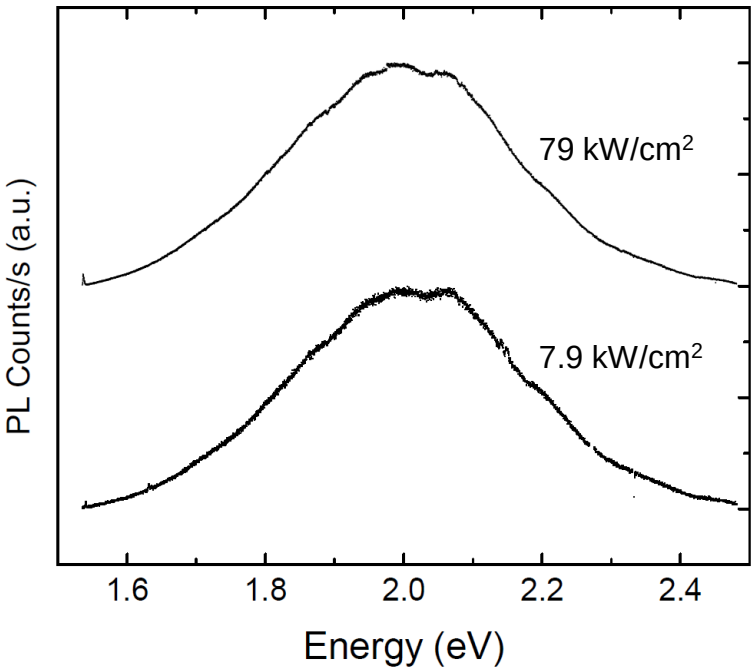

Figure B.1: Photoluminescence of self assembled sample at two different intensities

APPENDIX C

Linewidth of population pulsation as a function of excitation intensity

It was mentioned in chapter 7 that the linewidth of the population pulsation resonances increased as a function of ω_1 intensity as shown in Fig. C.1, even when the signal is verified to be in the $\chi^{(3)}$ limit. The linewidths shown in Fig. C.1 were found by fitting the population pulsations to a single Lorentzian for ω_1 values very close to the center of the modulated absorption spectrum. The physical origin for this effect is still under investigation.

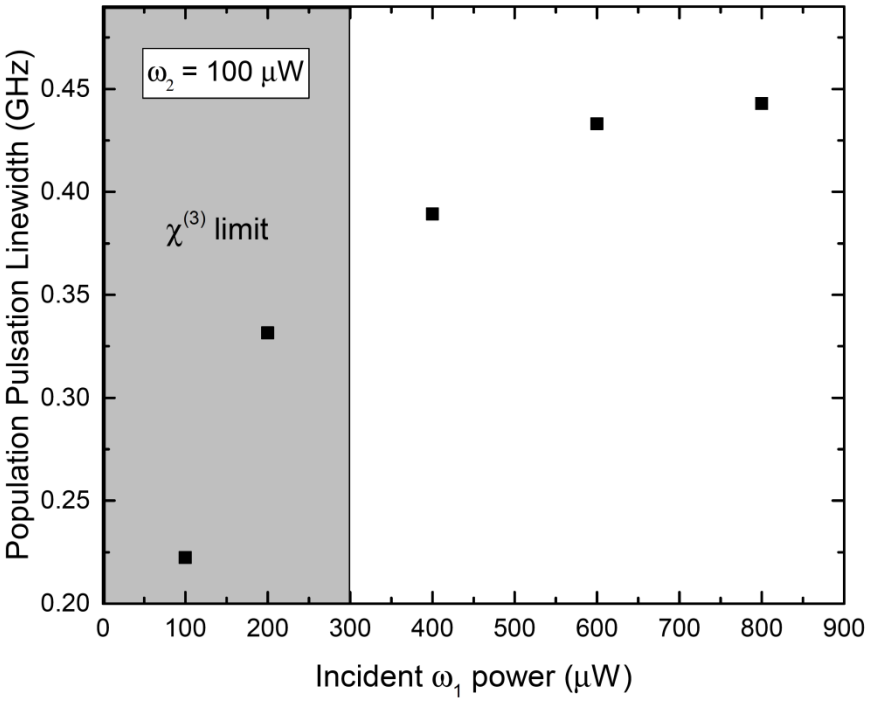

Figure C.1: Linewidth of population pulsation resonances measured near the peak of the modulated absorption distribution versus the incident ω_1 power. The shaded region shows the ω_1 intensities for which the signal is in the $\chi^{(3)}$ limit..

BIBLIOGRAPHY

BIBLIOGRAPHY

[1] S. Nakamura, "Nobel Lecture: Background Story of the Invention of Efficient Blue InGaN Light Emitting Diodes", Nobelprize.org (2014).

[2] V. Zwiller, T. Aichele, O. Benson, "Quantum optics with single quantum dot devices", *New Journal of Physics* **6**, 96 (2004).

[3] M. Suzuki, T. Uenoyama, A. Yanase, "First-principles calculations of effective-mass parameters of AlN and GaN", *Phys. Rev. B* **52**, 8132 (1995).

[4] S. L. Chuang, C. S. Chang, "k·p method for strained wurtzite semiconductors", *Phys. Rev. B* **54**, 2491 (1996).

[5] M. Winkelnkemper, *Electronic Structure of Nitride-based Quantum Dots*, Ph.D. thesis, Technischen Universitt Berlin (2008).

[6] S. Fernndez-Garrido, J. Grandal, E. Calleja, M. A. Snchez-Garca, D. Lpez-Romero, "A growth diagram for plasma-assisted molecular beam epitaxy of GaN nanocolumns on Si(111)", *Journal of Applied Physics* **106**, 126102 (2009).

[7] S. Jahangir, M. Mandl, M. Strassburg, P. Bhattacharya, "Molecular beam epitaxial growth and optical properties of red-emitting (=650nm) InGaN/GaN disks-in-nanowires on silicon", *Appl. Phys. Lett.* **102**, 071101 (2013).

[8] D. G. Steel, S. C. Rand, "Ultranarrow Nonlinear Optical Resonances in Solids", *Phys. Rev. Lett.* **55**, 2285 (1985).

[9] G. Tourbot, C. Bougerol, F. Glas, L. F. Zagonel, Z. Mahfoud, S. Meuret, P. Gilet, M. Kociak, B. Gayral, B. Daudin, "Growth mechanism and properties of InGaN insertions in GaN nanowires", *Nanotech.* **23**, 135703 (2012).

[10] S. Deshpande, T. Frost, A. Hazari, P. Bhattacharya, "Electrically pumped single-photon emission at room temperature from a single InGaN/GaN quantum dot", *Appl. Phys. Lett.* **105**, 141109 (2014).

[11] J. Singh, *Electronic and Optoelectronic Properties of Semiconductor Structures*, Camrbidge University Press (2003).

[12] S. Deshpande, T. Frost, L. Yan, S. Jahangir, A. Hazari, X. Liu, J. Mirecki-Millunchick, Z. Mi, P. Bhattacharya, "Formation and Nature of InGaN Quantum Dots in GaN Nanowires", *Nano Lett.* **15**, 1647 (2015).

[13] D. of Energy, "Energy Savings Forecast of Solid-State Lighting in General Illumination Applications", Technical report, Department of Energy (2014).

[14] S. Nakamura, T. Mukai, M. Senoh, "Candelaclass highbrightness InGaN/AlGaN doubleheterostructure bluelightemitting diodes", *Applied Physics Letters* **64**, 1687 (1994).

[15] M. Krames, O. Shchekin, R. Mueller-Mach, G. Mueller, L. Zhou, G. Harbers, M. Craford, "Status and Future of High-Power Light-Emitting Diodes for Solid-State Lighting", *Journal of Display Technology* **3**, 160 (2007).

[16] K. A. Bulashevich, A. V. Kulik, S. Y. Karpov, "Optimal ways of colour mixing for high-quality white-light LED sources", *physica status solidi (a)* **212**, 914 (2015).

[17] Y.-R. Wu, Y.-Y. Lin, H.-H. Huang, J. Singh, "Electronic and optical properties of InGaN quantum dot based light emitters for solid state lighting", *J. Appl. Phys.* **105**, 013117 (2009).

[18] W. Guo, A. Banerjee, P. Bhattacharya, B. S. Ooi, "InGaN/GaN disk-in-nanowire white light emitting diodes on (001) silicon", *Applied Physics Letters* **98**, 193102 (2011).

[19] M. G. Kibria, H. P. T. Nguyen, K. Cui, S. Zhao, D. Liu, H. Guo, M. L. Trudeau, S. Paradis, A.-R. Hakima, Z. Mi, "One-Step Overall Water Splitting under Visible Light Using Multiband InGaN/GaN Nanowire Heterostructures", *ACS Nano* **7**, 7886 (2013).

[20] N. G. Yeh, C.-H. Wu, T. C. Cheng, "Light-emitting diodesTheir potential in biomedical applications", *Renewable and Sustainable Energy Reviews* **14**, 2161 (2010).

[21] Y. Narukawa, Y. Kawakami, M. Funato, S. Fujita, S. Fujita, S. Nakamura, "Role of self-formed InGaN quantum dots for exciton localization in the purple laser diode emitting at 420 nm", *Applied Physics Letters* **70**, 981 (1997).

[22] M. Dutta, M. A. Stroscio, *Advances in Semiconductor Lasers and Applications to Optoelectronics*, World Scientific Publishing (2000).

[23] K. Okamoto, J. Kashiwagi, T. Tanaka, M. Kubota, "Nonpolar m-plane InGaN multiple quantum well laser diodes with a lasing wavelength of 499.8 nm", *Applied Physics Letters* **94**, 071105 (2009).

[24] Y. Yoshizumi, M. Adachi, Y. Enya, T. Kyono, S. Tokuyama, T. Sumitomo, K. Akita, T. Ikegami, M. Ueno, K. Katayama, T. Nakamura, "Continuous-Wave Operation of 520 nm Green InGaN-Based Laser Diodes on Semi-Polar 2021 GaN Substrates", *Applied Physics Express* **2**, 092101 (2009).

[25] A. Woolf, T. Puchtler, I. Aharonovich, T. Zhu, N. Niu, D. Wang, R. Oliver, E. L. Hu, "Distinctive signature of indium gallium nitride quantum dot lasing in microdisk cavities", *Proceedings of the National Academy of Sciences of the United States of America* **111**, 14042 (2014).

[26] A. Banerjee, T. Frost, S. Jahangir, E. Stark, P. Bhattacharya, "InGaN/GaN self-organized quantum dot lasers grown by molecular beam epitaxy", *Journal of Crystal Growth* **378**, 566 , the 17th International Conference on Molecular Beam Epitaxy (2013).

[27] T. Frost, S. Jahangir, E. Stark, S. Deshpande, A. Hazari, C. Zhao, B. S. Ooi, P. Bhattacharya, "Monolithic Electrically Injected Nanowire Array Edge-Emitting Laser on (001) Silicon", *Nano Lett.* **14**, 4535 (2014).

[28] H. Haug, S. W. Koch, *Quantum Theory of the Optical and Electronic Properties of Semiconductors*, World Scientific Publishing, 3 edition (1990).

[29] R. Hanbury-Brown, R. Q. Twiss, "Correlation between Photons in two Coherent Beams of Light", *Nature* **177**, 27 (1956).

[30] P. R. Berman, V. S. Malinovsky, *Principles of Laser Spectroscopy and Quantum Optics*, Princeton Univ. Press, Princeton, NJ, USA (2011).

[31] P. Michler, A. Kiraz, C. Becher, W. V. Schoenfeld, P. M. Petroff, L. Zhang, E. Hu, A. Imamoglu, "A Quantum Dot Single-Photon Turnstile Device", *Science* **290**, 2282 (2000).

[32] W. Shan, B. D. Little, A. J. Fischer, J. J. Song, B. Goldenberg, W. G. Perry, M. D. Bremser, R. F. Davis, "Binding energy for the intrinsic excitons in wurtzite GaN", *Phys. Rev. B* **54**, 16369 (1996).

[33] M. J. Holmes, K. Choi, S. Kako, M. Arita, Y. Arakawa, "Room-Temperature Triggered Single Photon Emission from a III-Nitride Site-Controlled Nanowire Quantum Dot", *Nano Lett.* **14**, 982 (2014).

[34] W. H. Knox, R. L. Fork, M. C. Downer, D. A. B. Miller, D. S. Chemla, C. V. Shank, A. C. Gossard, W. Wiegmann, "Femtosecond Dynamics of Resonantly Excited Excitons in Room-Temperature GaAs Quantum Wells", *Phys. Rev. Lett.* **54**, 1306 (1985).

[35] D. I. Lubyshev, P. P. GonzlezBorrero, E. Marega, E. Petitprez, N. La Scala, P. Basmaji, "Exciton localization and temperature stability in selforganized InAs quantum dots", *Applied Physics Letters* **68**, 205 (1996).

[36] C. H. Bennett, G. Brassard, "Quantum cryptography: Public key distribution and coin tossing", *Theoretical Computer Science* **560, Part 1**, 7 , theoretical Aspects of Quantum Cryptography celebrating 30 years of {BB84} (2014).

[37] T. Jennewein, C. Simon, G. Weihs, H. Weinfurter, A. Zeilinger, "Quantum Cryptography with Entangled Photons", *Phys. Rev. Lett.* **84**, 4729 (2000).

[38] C.-H. Teng, L. Zhang, T. A. Hill, B. Demory, H. Deng, P.-C. Ku, "Elliptical quantum dots as on-demand single photons sources with deterministic polarization states", *Applied Physics Letters* **107**, 191105 (2015).

[39] A. Lundskog, C.-W. Hsu, K. Fredrik Karlsson, S. Amloy, D. Nilsson, U. Forsberg, P. Olof Holtz, E. Janzen, "Direct generation of linearly polarized photon emission with designated orientations from site-controlled InGaN quantum dots", *Light Sci Appl* **3**, e139 (2014).

[40] C. Schneider, A. Huggenberger, T. Snner, T. Heindel, M. Strau, S. Gpfert, P. Weinmann, S. Reitzenstein, L. Worschech, M. Kamp, S. Hfling, A. Forchel, "Single site-controlled In(Ga)As/GaAs quantum dots: growth, properties and device integration", *Nanotechnology* **20**, 434012 (2009).

[41] T. Takagahara, "Enhanced excitonic optical nonlinearity and exciton dynamics in semiconductor microstructures", *Surface Science* **196**, 590 (1988).

[42] D. P. DiVincenzo, "Quantum Computation", *Science* **270**, 255 (1995).

[43] T. D. Ladd, F. Jelezko, R. Laflamme, Y. Nakamura, C. Monroe, J. L. O/'Brien, "Quantum computers", *Nature* **464**, 45 (2010).

[44] P. W. Shor, "Polynomial-Time Algorithms for Prime Factorization and Discrete Logarithms on a Quantum Computer", *SIAM Review* **41**, 303 (1999).

[45] R. L. Rivest, A. Shamir, L. Adleman, "A Method for Obtaining Digital Signatures and Public-key Cryptosystems", *Commun. ACM* **21**, 120 (1978).

[46] R. P. Feynman, "Simulating physics with computers", *International Journal of Theoretical Physics* **21**, 467 (1982).

[47] A. J. Ramsay, "A review of the coherent optical control of the exciton and spin states of semiconductor quantum dots", *Semiconductor Science and Technology* **25**, 103001 (2010).

[48] N. H. Bonadeo, J. Erland, D. Gammon, D. Park, D. S. Katzer, D. G. Steel, "Coherent Optical Control of the Quantum State of a Single Quantum Dot", *Science* **282**, 1473 (1998).

[49] G. Chen, N. H. Bonadeo, D. G. Steel, †. D. Gammon, D. S. Katzer, D. Park, L. J. Sham, "Optically Induced Entanglement of Excitons in a Single Quantum Dot", *Science* **289**, 1906 (2000).

[50] X. Xu, B. Sun, P. R. Berman, D. G. Steel, A. S. Bracker, D. Gammon, L. J. Sham, "Coherent population trapping of an electron spin in a single negatively charged quantum dot", *Nat Phys* **4**, 692 (2008).

[51] E. D. Kim, K. Truex, X. Xu, B. Sun, D. G. Steel, A. S. Bracker, D. Gammon, L. J. Sham, "Fast Spin Rotations by Optically Controlled Geometric Phases in a Charge-Tunable InAs Quantum Dot", *Phys. Rev. Lett.* **104**, 167401 (2010).

[52] J. R. Schaibley, A. P. Burgers, G. A. McCracken, L.-M. Duan, P. R. Berman, D. G. Steel, A. S. Bracker, D. Gammon, L. J. Sham, "Demonstration of Quantum Entanglement between a Single Electron Spin Confined to an InAs Quantum Dot and a Photon", *Phys. Rev. Lett.* **110**, 167401 (2013).

[53] M. Holmes, S. Kako, K. Choi, P. Podemski, M. Arita, Y. Arakawa, "Measurement of an Exciton Rabi Rotation in a Single GaN/Al_xGa_{1-x}N Nanowire-Quantum Dot Using Photoluminescence Spectroscopy: Evidence for Coherent Control", *Phys. Rev. Lett.* **111**, 057401 (2013).

[54] B. P. L. Reid, C. Kocher, T. Zhu, F. Oehler, R. Emery, C. C. S. Chan, R. A. Oliver, R. A. Taylor, "Observations of Rabi oscillations in a non-polar InGaN quantum dot", *Appl. Phys. Lett.* **104**, 263108 (2014).

[55] S. V. Deshpande, *III-Nitride Based Visible Single-Photon Sources*, Ph.D. thesis, The University of Michigan (2015).

[56] Y. Wu, *Coherent Ultrafast Optical Manipulations of Semiconductor Quantum Dots for Quantum Computation*, Ph.D. thesis, The University of Michigan (2008).

[57] N. Bonadeo, *Nano-Optics: Coherent Optical Spectroscopy of Single Semiconductor Quantum Dots*, Ph.D. thesis, The University of Michigan (1999).

[58] F. Bloch, "Über die Quantenmechanik der Elektronen in Kristallgittern", *Zeitschrift für Physik* **52**, 555 (1929).

[59] N. W. Ashcroft, N. D. Mermin, *Solid State Physics*, Holt, Rinehart and Winston, 33 edition (1976).

[60] J. C. Slater, G. F. Koster, "Simplified LCAO Method for the Periodic Potential Problem", *Phys. Rev.* **94**, 1498 (1954).

[61] J. C. Slater, "An Augmented Plane Wave Method for the Periodic Potential Problem", *Phys. Rev.* **92**, 603 (1953).

[62] W. E. Rudge, "Self-Consistent Augmented-Plane-Wave Method", *Phys. Rev.* **181**, 1024 (1969).

[63] J. M. Luttinger, W. Kohn, "Motion of Electrons and Holes in Perturbed Periodic Fields", *Phys. Rev.* **97**, 869 (1955).

[64] E. O. Kane, "Band structure of indium antimonide", *Journal of Physics and Chemistry of Solids* **1**, 249 (1957).

[65] J. Ziman, *Principles of the Theory of Solids*, Cambridge University Press, 2 edition (1972).

[66] R. J. Elliott, "Theory of the Effect of Spin-Orbit Coupling on Magnetic Resonance in Some Semiconductors", *Phys. Rev.* **96**, 266 (1954).

[67] M. Winkelnkemper, R. Seguin, S. Rodt, A. Schliwa, L. Reimann, A. Strittmatter, A. Hoffmann, D. Bimberg, "Polarized emission lines from A- and B-type excitonic complexes in single InGaN/GaN quantum dots", *Journal of Applied Physics* **101**, 113708 (2007).

[68] G. Dresselhaus, "Effective mass approximation for excitons", *Journal of Physics and Chemistry of Solids* **1**, 14 (1956).

[69] M. D. Sturge, "Optical Absorption of Gallium Arsenide between 0.6 and 2.75 eV", *Phys. Rev.* **127**, 768 (1962).

[70] G. E. Pikus, G. L. Bir, "Exchange Interaction in Bound Excitons in Semiconductors", *Soviet Physics JETP* **62**, 324 (1972).

[71] P. S. A. G. W. W. D. Chemla, D. Miller, "Room temperature excitonic nonlinear absorption and refraction in GaAs/AlGaAs multiple quantum well structures", *IEEE Journal of Quantum Electronics* **20**, 265 (1984).

[72] K. Torii, T. Deguchi, T. Sota, K. Suzuki, S. Chichibu, S. Nakamura, "Reflectance and emission spectra of excitonic polaritons in GaN", *Phys. Rev. B* **60**, 4723 (1999).

[73] T. Hanada, *Basic Properties of ZnO, GaN, and Related Materials*, 1–19, Springer Berlin Heidelberg, Berlin, Heidelberg, ISBN 978-3-540-88847-5 (2009).

[74] S. Schmitt-Rink, D. A. B. Miller, D. S. Chemla, "Theory of the linear and nonlinear optical properties of semiconductor microcrystallites", *Phys. Rev. B* **35**, 8113 (1987).

[75] V. Bougrov, M. Levinshtein, S. L. Rumyantsev, A. Zubrilov, *Properties of Advanced Semiconductor Materials GaN, AlN, InN, BN, SiC, SiGe*, John Wiley and Sons (2001).

[76] T. Matsuoka, H. Okamoto, M. Nakao, H. Harima, E. Kurimoto, "Optical bandgap energy of wurtzite InN", *Applied Physics Letters* **81**, 1246 (2002).

[77] H. P. Maruska, J. J. Tietjen, "THE PREPARATION AND PROPERTIES OF VAPORDEPOSITED SINGLECRYSTALLINE GaN", *Applied Physics Letters* **15**, 327 (1969).

[78] I. Puchugin, M. Tiachala, *Ivz. Akad. Nauk. SSSR, Neorg. Mater.* **14**, 175 (1978).

[79] F. Bernardini, V. Fiorentini, D. Vanderbilt, "Spontaneous polarization and piezoelectric constants of III-V nitrides", *Phys. Rev. B* **56**, R10024 (1997).

[80] R. B. Schwarz, K. Khachaturyan, E. R. Weber, "Elastic moduli of gallium nitride", *Applied Physics Letters* **70**, 1122 (1997).

[81] K. Kim, W. R. L. Lambrecht, B. Segall, "Elastic constants and related properties of tetrahedrally bonded BN, AlN, GaN, and InN", *Phys. Rev. B* **53**, 16310 (1996).

[82] D. A. B. Miller, D. S. Chemla, T. C. Damen, A. C. Gossard, W. Wiegmann, T. H. Wood, C. A. Burrus, "Band-Edge Electroabsorption in Quantum Well Structures: The Quantum-Confined Stark Effect", *Phys. Rev. Lett.* **53**, 2173 (1984).

[83] T. Takeuchi, S. Sota, M. Katsuragawa, M. Komori, H. Takeuchi, H. Amano, I. Akasaki, "Quantum-Confined Stark Effect due to Piezoelectric Fields in GaInN Strained Quantum Wells", *Japanese Journal of Applied Physics* **36**, L382 (1997).

[84] T. Kuroda, A. Tackeuchi, "Influence of free carrier screening on the luminescence energy shift and carrier lifetime of InGaN quantum wells", *Journal of Applied Physics* **92**, 3071 (2002).

[85] C.-K. Kao, A. Bhattacharyya, C. Thomidis, R. Paiella, T. D. Moustakas, "Electroabsorption modulators based on bulk GaN films and GaN/AlGaN multiple quantum wells", *Journal of Applied Physics* **109**, 083102 (2011).

[86] F. Rana, "Lecture Notes from: Semiconductor Optics at Cornell Univerisity", Online (2016).

[87] C. J. Humphreys, "Does In form In-rich clusters in InGaN quantum wells?", *Philosophical Magazine* **87**, 1971 (2007).

[88] S. Chichibu, K. Wada, S. Nakamura, "Spatially resolved cathodoluminescence spectra of InGaN quantum wells", *Applied Physics Letters* **71**, 2346 (1997).

[89] H. Schömig, S. Halm, A. Forchel, G. Bacher, J. Off, F. Scholz, "Probing Individual Localization Centers in an InGaN/GaN Quantum Well", *Phys. Rev. Lett.* **92**, 106802 (2004).

[90] D. M. Graham, A. Soltani-Vala, P. Dawson, M. J. Godfrey, T. M. Smeeton, J. S. Barnard, M. J. Kappers, C. J. Humphreys, E. J. Thrush, "Optical and microstructural studies of InGaNGaN single-quantum-well structures", *Journal of Applied Physics* **97**, 103508 (2005).

[91] I. Ho, G. B. Stringfellow, "Solid phase immiscibility in GaInN", *Applied Physics Letters* **69**, 2701 (1996).

[92] H. K. Cho, J. Y. Lee, N. Sharma, C. J. Humphreys, G. M. Yang, C. S. Kim, J. H. Song, P. W. Yu, "Effect of growth interruptions on the light emission and indium clustering of InGaN/GaN multiple quantum wells", *Applied Physics Letters* **79**, 2594 (2001).

[93] L. Bellaiche, T. Mattila, L.-W. Wang, S.-H. Wei, A. Zunger, "Resonant hole localization and anomalous optical bowing in InGaN alloys", *Applied Physics Letters* **74**, 1842 (1999).

[94] P. R. C. Kent, A. Zunger, "Carrier localization and the origin of luminescence in cubic InGaN alloys", *Applied Physics Letters* **79**, 1977 (2001).

[95] L.-W. Wang, "Calculations of carrier localization in $In_xGa_{1-x}N$", *Phys. Rev. B* **63**, 245107 (2001).

[96] S. F. Chichibu, A. Uedono, T. Onuma, B. A. Haskell, A. Chakraborty, T. Koyama, P. T. Fini, S. Keller, S. P. DenBaars, J. S. Speck, U. K. Mishra, S. Nakamura, S. Yamaguchi, S. Kamiyama, H. Amano, I. Akasaki, J. Han, T. Sota, "Origin of defect-insensitive emission probability in In-containing (Al,In,Ga)N alloy semiconductors", *Nat Mater* **5**, 810 (2006).

[97] F. Urbach, "The Long-Wavelength Edge of Photographic Sensitivity and of the Electronic Absorption of Solids", *Phys. Rev.* **92**, 1324 (1953).

[98] R. W. Martin, P. G. Middleton, K. P. ODonnell, W. Van der Stricht, "Exciton localization and the Stokes shift in InGaN epilayers", *Appl. Phys. Lett.* **74**, 263 (1999).

[99] K. P. O'Donnell, R. W. Martin, P. G. Middleton, "Origin of Luminescence from InGaN Diodes", *Phys. Rev. Lett.* **82**, 237 (1999).

[100] D. O. Kundys, J.-P. R. Wells, A. D. Andreev, S. A. Hashemizadeh, T. Wang, P. J. Parbrook, A. M. Fox, D. J. Mowbray, M. S. Skolnick, "Resolution of discrete excited states in $In_xGa_{1-x}N$ multiple quantum wells using degenerate four-wave mixing", *Phys. Rev. B* **73**, 165309 (2006).

[101] K. O. Y. N. T. M. Yoichi Kawakami, Akio Kaneta, *Handbook of Nano-Optics and Nano-Photonics*, chapter 12, 483–525, Springer Berlin Heidelberg (2013).

[102] Y.-H. Cho, T. J. Schmidt, S. Bidnyk, G. H. Gainer, J. J. Song, S. Keller, U. K. Mishra, S. P. DenBaars, "Linear and nonlinear optical properties of $In_xGa_{1-x}N$/GaN heterostructures", *Phys. Rev. B* **61**, 7571 (2000).

[103] T. Wang, D. Nakagawa, M. Lachab, T. Sugahara, S. Sakai, "Optical investigation of InGaN/GaN multiple quantum wells", *Applied Physics Letters* **74**, 3128 (1999).

[104] Y.-H. Cho, G. H. Gainer, A. J. Fischer, J. J. Song, S. Keller, U. K. Mishra, S. P. DenBaars, "S-shaped temperature-dependent emission shift and carrier dynamics in InGaN/GaN multiple quantum wells", *Applied Physics Letters* **73**, 1370 (1998).

[105] Q. Li, S. J. Xu, W. C. Cheng, M. H. Xie, S. Y. Tong, C. M. Che, H. Yang, "Thermal redistribution of localized excitons and its effect on the luminescence band in InGaN ternary alloys", *Applied Physics Letters* **79**, 1810 (2001).

[106] S.-W. Feng, Y.-C. Cheng, Y.-Y. Chung, C. C. Yang, Y.-S. Lin, C. Hsu, K.-J. Ma, J.-I. Chyi, "Impact of localized states on the recombination dynamics in InGaN/GaN quantum well structures", *Journal of Applied Physics* **92**, 4441 (2002).

[107] E. Cohen, M. D. Sturge, "Fluorescence line narrowing, localized exciton states, and spectral diffusion in the mixed semiconductor CdS_xSe_{1-x}", *Phys. Rev. B* **25**, 3828 (1982).

[108] C. Gourdon, P. Lavallard, "Exciton Transfer between Localized States in CdS1xSex Alloys", *physica status solidi (b)* **153**, 641 (1989).

[109] M. F. S. H. Scher, J. T. Bendler, "Time-Scale Invariance in Transport and Relaxation", *Phys Today* **44**, 26 (1991).

[110] X. Chen, B. Henderson, K. P. ODonnell, "Luminescence decay in disordered lowdimensional semiconductors", *Applied Physics Letters* **60**, 2672 (1992).

[111] L. Cerutti, J. Risti, S. Fernndez-Garrido, E. Calleja, A. Trampert, K. H. Ploog, S. Lazic, J. M. Calleja, "Wurtzite GaN nanocolumns grown on Si(001) by molecular beam epitaxy", *Applied Physics Letters* **88**, 213114 (2006).

[112] H. P. T. Nguyen, S. Zhang, K. Cui, X. Han, S. Fathololoumi, M. Couillard, G. A. Botton, Z. Mi, "p-Type Modulation Doped InGaN/GaN Dot-in-a-Wire White-Light-Emitting Diodes Monolithically Grown on Si(111)", *Nano Letters* **11**, 1919, pMID: 21517080 (2011).

[113] W. Guo, M. Zhang, A. Banerjee, P. Bhattacharya, "Catalyst-Free InGaN/GaN Nanowire Light Emitting Diodes Grown on (001) Silicon by Molecular Beam Epitaxy", *Nano Lett.* **10**, 3355 (2010).

[114] S. Albert, A. Bengoechea-Encabo, M. A. Sanchez-Garcia, E. Calleja, U. Jahn, "Selective area growth and characterization of InGaN nanocolumns for phosphor-free white light emission", *Journal of Applied Physics* **113**, 114306 (2013).

[115] V. Consonni, "Self-induced growth of GaN nanowires by molecular beam epitaxy: A critical review of the formation mechanisms", *physica status solidi (RRL) Rapid Research Letters* **7**, 699 (2013).

[116] H. P. T. Nguyen, K. Cui, S. Zhang, S. Fathololoumi, Z. Mi, "Full-color InGaN/GaN dot-in-a-wire light emitting diodes on silicon", *Nanotechnology* **22**, 445202 (2011).

[117] F. Sacconi, M. Auf der Maur, A. Di Carlo, "Optoelectronic Properties of Nanocolumn InGaN/GaN LEDs", *IEEE Trans. Elect. Dev.* **59**, 2979 (2012).

[118] L. Zhang, T. A. Hill, C.-H. Teng, B. Demory, P.-C. Ku, H. Deng, "Carrier dynamics in site- and structure-controlled InGaN/GaN quantum dots", *Phys. Rev. B* **90**, 245311 (2014).

[119] S. D. Hersee, A. K. Rishinaramangalam, M. N. Fairchild, L. Zhang, P. Varangis, "Threading defect elimination in GaN nanowires", *Journal of Materials Research* **26**, 2293 (2011).

[120] S. Deshpande, J. Heo, A. Das, P. Bhattacharya, "Electrically driven polarized single-photon emission from an InGaN quantum dot in a GaN nanowire", *Nat. Commun.* **4**, 1675 (2013).

[121] S. Pereira, M. R. Correia, E. Pereira, K. P. O'Donnell, C. Trager-Cowan, F. Sweeney, E. Alves, "Compositional pulling effects in $In_xGa_{1-x}N$/GaN layers: A combined depth-resolved cathodoluminescence and Rutherford backscattering/channeling study", *Phys. Rev. B* **64**, 205311 (2001).

[122] W.-C. Tsai, C.-H. Hsu, S.-F. Fu, F.-W. Lee, C.-Y. Chen, W.-C. Chou, W.-K. Chen, W.-H. Chang, "Optical properties associated with strain relaxations in thick InGaN epitaxial films", *Opt. Express* **22**, A416 (2014).

[123] G. Tourbot, C. Bougerol, A. Grenier, M. D. Hertog, D. Sam-Giao, D. Cooper, P. Gilet, B. Gayral, B. Daudin, "Structural and optical properties of InGaN/GaN nanowire heterostructures grown by PA-MBE", *Nanotech.* **22**, 075601 (2011).

[124] M. Povolotskyi, A. Di Carlo, "Elasticity theory of pseudomorphic heterostructures grown on substrates of arbitrary thickness", *Journal of Applied Physics* **100**, 063514 (2006).

[125] M. Auf der Maur, M. Povolotskyi, F. Sacconi, A. Di Carlo, "Simulation of piezoresistivity effect in FETs", *Journal of Computational Electronics* **5**, 323 (2006).

[126] L. Zhang, L.-K. Lee, C.-H. Teng, T. A. Hill, P.-C. Ku, H. Deng, "How much better are InGaN/GaN nanodisks than quantum wellsOscillator strength enhancement and changes in optical properties", *Applied Physics Letters* **104**, 051116 (2014).

[127] J. R. Schaibley, A. P. Burgers, G. A. McCracken, D. G. Steel, A. S. Bracker, D. Gammon, L. J. Sham, "Direct detection of time-resolved Rabi oscillations in a single quantum dot via resonance fluorescence", *Phys. Rev. B* **87**, 115311 (2013).

[128] N. H. Bonadeo, G. Chen, D. Gammon, D. S. Katzer, D. Park, D. G. Steel, "Nonlinear Nano-Optics: Probing One Exciton at a Time", *Phys. Rev. Lett.* **81**, 2759 (1998).

[129] H. Wang, K. Ferrio, D. G. Steel, Y. Z. Hu, R. Binder, S. W. Koch, "Transient nonlinear optical response from excitation induced dephasing in GaAs", *Phys. Rev. Lett.* **71**, 1261 (1993).

[130] H. Wang, D. G. Steel, "Effects of spectral diffusion on frequency-domain four-wave-mixing spectroscopy", *Phys. Rev. A* **43**, 3823 (1991).

[131] H. Haug, S. Schmitt-Rink, "Electron theory of the optical properties of laser-excited semiconductors", *Progress in Quantum Electronics* **9**, 3 (1984).

[132] N. Bloembergen, Y. R. Shen, "Quantum-Theoretical Comparison of Nonlinear Susceptibilities in Parametric Media, Lasers, and Raman Lasers", *Phys. Rev.* **133**, A37 (1964).

[133] R. Boyd, *Nonlinear Optics*, Academic Press, San Diego, CA, USA (2003).

[134] Y. Shen, *Principles of non-linear optics*, Wiley-Interscience, New York, NY, USA (1984).

[135] B. Saleh, M. Teich, *Fundamentals of Photonics*, Wiley Interscience (1991).

[136] J. A. Armstrong, N. Bloembergen, J. Ducuing, P. S. Pershan, "Interactions between Light Waves in a Nonlinear Dielectric", *Phys. Rev.* **127**, 1918 (1962).

[137] R. W. Boyd, S. Mukamel, "Origin of spectral holes in pump-probe studies of homogeneously broadened lines", *Phys. Rev. A* **29**, 1973 (1984).

[138] G. Khitrova, P. R. Berman, M. Sargent, "Theory of pump–probe spectroscopy", *J. Opt. Soc. Am. B* **5**, 160 (1988).

[139] S. Haroche, F. Hartmann, "Theory of Saturated-Absorption Line Shapes", *Phys. Rev. A* **6**, 1280 (1972).

[140] B. R. Mollow, "Stimulated Emission and Absorption near Resonance for Driven Systems", *Phys. Rev. A* **5**, 2217 (1972).

[141] D. G. Steel, J. T. Remillard, "Resonant nearly degenerate backward four-wave mixing in open and closed systems", *Phys. Rev. A* **36**, 4330 (1987).

[142] S. C. Rand, *Lectures on Light: Nonlinear and Quantum Optics using the Density Matrix*, Oxford University Press (2010).

[143] L. Rothberg, "{II} Dephasing-Induced Coherent Phenomena", volume 24 of *Progress in Optics*, 39 – 101, Elsevier (1987).

[144] P. Berman, G. Khitrova, "Theory of pump-probe spectroscopy using an amplitude approach1", *Optics Communications* **179**, 19 (2000).

[145] N. Bloembergen, H. Loten, R. Lynch, "Lineshapes in coherent resonant Raman scattering", *Indian J. Pure Appl. Phys.* **16**, 151 (1978).

[146] B. Dubetsky, P. R. Berman, "Theory of four-wave mixing using an amplitude approach", *Phys. Rev. A* **47**, 1294 (1993).

[147] Y. Prior, A. R. Bogdan, M. Dagenais, N. Bloembergen, "Pressure-Induced Extra Resonances in Four-Wave Mixing", *Phys. Rev. Lett.* **46**, 111 (1981).

[148] J. Liu, D. G. Steel, "High-resolution four-wave-mixing spectroscopy of collision-induced narrow resonances in Doppler-broadened systems", *Phys. Rev. A* **38**, 4639 (1988).

[149] I. A. Ostapenko, G. Hnig, C. Kindel, S. Rodt, A. Strittmatter, A. Hoffmann, D. Bimberg, "Large internal dipole moment in InGaN/GaN quantum dots", *Applied Physics Letters* **97**, 063103 (2010).

[150] P. R. Berman, R. G. Brewer, "Modified optical Bloch equations for solids", *Phys. Rev. A* **32**, 2784 (1985).

[151] C. R. Kagan, C. B. Murray, M. Nirmal, M. G. Bawendi, "Electronic Energy Transfer in CdSe Quantum Dot Solids", *Phys. Rev. Lett.* **76**, 1517 (1996).

[152] A. D. Greentree, J. H. Cole, A. R. Hamilton, L. C. L. Hollenberg, "Coherent electronic transfer in quantum dot systems using adiabatic passage", *Phys. Rev. B* **70**, 235317 (2004).

[153] M. Ouyang, D. D. Awschalom, "Coherent Spin Transfer Between Molecularly Bridged Quantum Dots", *Science* **301**, 1074 (2003).

[154] T. Takagahara, "Theory of exciton dephasing in semiconductor quantum dots", *Phys. Rev. B* **60**, 2638 (1999).

[155] E. T. Batteh, J. Cheng, G. Chen, D. G. Steel, D. Gammon, D. S. Katzer, D. Park, "Coherent nonlinear optical spectroscopy of single quantum dot excited states", *Applied Physics Letters* **84**, 1928 (2004).

[156] W. E. Lamb, "Theory of an Optical Maser", *Phys. Rev.* **134**, A1429 (1964).

[157] A. Yariv, P. Yeh, *Optical waves in crystals*, Wiley New York (1984).

[158] E. A. Donley, T. P. Heavner, F. Levi, M. O. Tataw, S. R. Jefferts, "Double-pass acousto-optic modulator system", *Review of Scientific Instruments* **76**, 063112 (2005).

[159] E. D. Kim, A. Majumdar, H. Kim, P. Petroff, J. Vukovi, "Differential reflection spectroscopy of a single quantum dot strongly coupled to a photonic crystal cavity", *Applied Physics Letters* **97**, 053111 (2010).

[160] J. R. Schaibley, T. Karin, H. Yu, J. S. Ross, P. Rivera, A. M. Jones, M. E. Scott, J. Yan, D. G. Mandrus, W. Yao, K.-M. Fu, X. Xu, "Population Pulsation Resonances of Excitons in Monolayer $MoSe_2$ with Sub-1 μeV Linewidths", *Phys. Rev. Lett.* **114**, 137402 (2015).

[161] Z. Zhou, B. Yin, J. Michel, "On-chip light sources for silicon photonics", *Light Sci Appl* **4**, e358 (2015).

[162] Y.-L. Chang, J. L. Wang, F. Li, Z. Mi, "High efficiency green, yellow, and amber emission from InGaN/GaN dot-in-a-wire heterostructures on Si(111)", *Appl. Phys. Lett.* **96**, 013106 (2010).

[163] L. Lymperakis, J. Neugebauer, "Large anisotropic adatom kinetics on nonpolar GaN surfaces: Consequences for surface morphologies and nanowire growth", *Phys. Rev. B* **79**, 241308 (2009).

[164] K. Grossklaus, A. Banerjee, S. Jahangir, P. Bhattacharya, J. Millunchick, "Misorientation defects in coalesced self-catalyzed GaN nanowires", *Journal of Crystal Growth* **371**, 142 (2013).

[165] S. Jahangir, T. Schimpke, M. Strassburg, K. A. Grossklaus, J. M. Millunchick, P. Bhattacharya, "Red-Emitting (= 610 nm) In0.51Ga0.49N/GaN Disk-in-Nanowire Light Emitting Diodes on Silicon", *IEEE Journal of Quantum Electronics* **50**, 530 (2014).

[166] L. Yan, S. Jahangir, S. A. Wight, B. Nikoobakht, P. Bhattacharya, J. M. Millunchick, "Structural and Optical Properties of Disc-in-Wire InGaN/GaN LEDs", *Nano Lett.* **15**, 1535 (2015).

[167] H. Sekiguchi, K. Kishino, A. Kikuchi, "Emission color control from blue to red with nanocolumn diameter of InGaN/GaN nanocolumn arrays grown on same substrate", *Appl. Phys. Lett.* **96**, 231104 (2010).

[168] L. Zhang, C.-H. Teng, T. A. Hill, L.-K. Lee, P.-C. Ku, H. Deng, "Single photon emission from site-controlled InGaN/GaN quantum dots", *Appl. Phys. Lett.* **103**, 192114 (2013).

[169] M. Cardona, *Solid State Physics Vol. 11: Modulation Spectroscopy*, The University of California, Academic Press (1969).

[170] E. Ejder, "Refractive index of GaN", *physica status solidi (a)* **6**, 445 (1971).

[171] Y. Varshni, "Temperature dependence of the energy gap in semiconductors", *Physica* **34**, 149 (1967).

[172] I. Vurgaftman, J. R. Meyer, L. R. Ram-Mohan, "Band parameters for IIIV compound semiconductors and their alloys", *J. Appl. Phys.* **89**, 5815 (2001).

[173] C. Lonsky, P. Thomas, A. Weller, "Optical dephasing in disordered semiconductors", *Phys. Rev. Lett.* **63**, 652 (1989).

[174] U. Mishra, J. Singh, *Semiconductor Device Physics and Design*, Springer (2008).

[175] T. Li, A. M. Fischer, Q. Y. Wei, F. A. Ponce, T. Detchprohm, C. Wetzel, "Carrier localization and nonradiative recombination in yellow emitting InGaN quantum wells", *Appl. Phys. Lett.* **96**, 031906 (2010).

[176] E. F. Hilinski, P. A. Lucas, Y. Wang, "A picosecond bleaching study of quantumconfined cadmium sulfide microcrystallites in a polymer film", *J. Chem. Phys.* **89**, 3435 (1988).

[177] Y. Wang, A. Suna, J. McHugh, E. F. Hilinski, P. A. Lucas, R. D. Johnson, "Optical transient bleaching of quantumconfined CdS clusters: The effects of surfacetrapped electronhole pairs", *J. Chem. Phys.* **92**, 6927 (1990).

[178] E. Kuokstis, J. W. Yang, G. Simin, M. A. Khan, R. Gaska, M. S. Shur, "Two mechanisms of blueshift of edge emission in InGaN-based epilayers and multiple quantum wells", *Applied Physics Letters* **80**, 977 (2002).

[179] D. F. Schroeter, D. J. Griffiths, P. C. Sercel, "Defect-assisted relaxation in quantum dots at low temperature", *Phys. Rev. B* **54**, 1486 (1996).

[180] N. H. Bonadeo, A. S. Lenihan, G. Chen, J. R. Guest, D. G. Steel, D. Gammon, D. S. Katzer, D. Park, "Single quantum dot states measured by optical modulation spectroscopy", *Applied Physics Letters* **75**, 2933 (1999).

[181] K. Omae, Y. Kawakami, S. Fujita, Y. Narukawa, T. Mukai, "Effects of internal electrical field on transient absorption in $In_xGa_{1-x}N$ thin layers and quantum wells with different thickness by pump and probe spectroscopy", *Phys. Rev. B* **68**, 085303 (2003).

[182] C. M. Lawson, R. C. Powell, W. K. Zwicker, "Measurement of Exciton Diffusion Lengths in $Nd_xLa_{1-x}P_5O_{14}$ by Four-Wave Mixing Techniques", *Phys. Rev. Lett.* **46**, 1020 (1981).

[183] F. Chen, A. N. Cartwright, "Femtosecond pump and probe spectroscopy of optical nonlinearities in an InGaN/GaN heterostructure", *MRS Proceedings* **743** (2002).

[184] J. R. Guest, T. H. Stievater, G. Chen, E. A. Tabak, B. G. Orr, D. G. Steel, D. Gammon, D. S. Katzer, "Near-Field Coherent Spectroscopy and Microscopy of a Quantum Dot System", *Science* **293**, 2224 (2001).

[185] Y. Oshikane, T. Kataoka, M. Okuda, S. Hara, H. Inoue, M. Nakano, "Observation of nanostructure by scanning near-field optical microscope with small sphere probe", *Science and Technology of Advanced Materials* **8**, 181 (2007).

[186] L. Zhang, C.-H. Teng, P.-C. Ku, H. Deng, "Charge-tunable indium gallium nitride quantum dots", *Phys. Rev. B* **93**, 085301 (2016).

[187] A. P. Burgers, *Towards Quantum Teleportation from a Spontaneous Parametric Down-Conversion Source to a Quantum Dot Spin by Hong-Ou-Mandel Interferece*, Ph.D. thesis, The University of Michigan (2015).

[188] A. Moelbjerg, P. Kaer, M. Lorke, J. Mørk, "Resonance Fluorescence from Semiconductor Quantum Dots: Beyond the Mollow Triplet", *Phys. Rev. Lett.* **108**, 017401 (2012).

[189] M. Holmes, S. Kako, K. Choi, M. Arita, Y. Arakawa, "Spectral diffusion and its influence on the emission linewidths of site-controlled GaN nanowire quantum dots", *Phys. Rev. B* **92**, 115447 (2015).

[190] B. P. Reid, T. Zhu, T. J. Puchtler, L. J. Fletcher, C. C. Chan, R. A. Oliver, R. A. Taylor, "Origins of Spectral Diffusion in the Micro-Photoluminescence of Single InGaN Quantum Dots", *Japanese Journal of Applied Physics* **52**, 08JE01 (2013).

[191] R. Bardoux, T. Guillet, P. Lefebvre, T. Taliercio, T. Bretagnon, S. Rousset, B. Gil, F. Semond, "Photoluminescence of single GaNAlN hexagonal quantum dots on Si(111): Spectral diffusion effects", *Phys. Rev. B* **74**, 195319 (2006).

[192] C. Kindel, G. Callsen, S. Kako, T. Kawano, H. Oishi, G. Hnig, A. Schliwa, A. Hoffmann, Y. Arakawa, "Spectral diffusion in nitride quantum dots: Emission energy dependent linewidths broadening via giant built-in dipole moments", *physica status solidi (RRL) Rapid Research Letters* **8**, 408 (2014).

[193] E. Martinez-Guerrero, C. Adelmann, F. Chabuel, J. Simon, N. T. Pelekanos, G. Mula, B. Daudin, G. Feuillet, H. Mariette, "Self-assembled zinc blende GaN quantum dots grown by molecular-beam epitaxy", *Applied Physics Letters* **77**, 809 (2000).

[194] S. Sergent, S. Kako, M. Brger, D. J. As, Y. Arakawa, "Narrow spectral linewidth of single zinc-blende GaN/AlN self-assembled quantum dots", *Applied Physics Letters* **103**, 151109 (2013).

[195] T. Zhu, F. Oehler, B. P. L. Reid, R. M. Emery, R. A. Taylor, M. J. Kappers, R. A. Oliver, "Non-polar (11-20) InGaN quantum dots with short exciton lifetimes grown by metal-organic vapor phase epitaxy", *Applied Physics Letters* **102**, 251905 (2013).

[196] K. Choi, S. Kako, M. J. Holmes, M. Arita, Y. Arakawa, "Strong exciton confinement in site-controlled GaN quantum dots embedded in nanowires", *Applied Physics Letters* **103**, 171907 (2013).

[197] X. Xiao, A. J. Fischer, G. T. Wang, P. Lu, D. D. Koleske, M. E. Coltrin, J. B. Wright, S. Liu, I. Brener, G. S. Subramania, J. Y. Tsao, "Quantum-Size-Controlled Photochemical Fabrication of Epitaxial InGaN Quantum Dots", *Nano Lett.* **14**, 5616 (2014).

[198] E. Knill, R. Laflamme, G. J. Milburn, "A scheme for efficient quantum computation with linear optics", *Nature* **409**, 46 (2001).

[199] M. Abramowitz, I. Stegun, *Handbook of Mathematical Functions*, Dover Publications Inc (1972).